Bearingless AC Homopolar Machine Design and Control for Distributed Flywheel Energy Storage

A DISSERTATION
SUBMITTED TO THE FACULTY OF THE GRADUATE SCHOOL
OF THE UNIVERSITY OF MINNESOTA
BY

Eric Loren Severson

IN PARTIAL FULFILLMENT OF THE REQUIREMENTS
FOR THE DEGREE OF
DOCTOR OF PHILOSOPHY

Advisor: Ned Mohan,
Co-advisor: Robert Nilssen

June, 2015

Acknowledgements

This dissertation has spanned nearly six years, the same number research trips to NTNU in Trondheim, Norway totaling nearly one year, and countless individuals who have gone out of their way to support me. I have been fortunate to be part of a large and active research group at the University of Minnesota and to have been embraced by an even larger research department at NTNU.

I am especially thankful to my advisor, Ned Mohan, who has taught me that the most important thing a person can do is to show respect for others. Professor Mohan's rare combination of mischief, humility, passion for mentoring students, and laissez-faire attitude has molded me as a researcher and encouraged this project to grow wildly beyond my initial goals. I have received an incredible amount of support from my co-advisor, Robert Nilssen, in the form of creative ideas and directions for the project, lessons on winding design, and creating a welcoming research environment at NTNU. I would also like to acknowledge the support of the graduate students and staff with whom I have had the pleasure of working with at both the University of Minnesota and NTNU–especially Tore Undeland, for his help initiating my collaboration with NTNU and serving as my host advisor on the first research trip; Dominik Häger, for all of his effort, time, and creativity in constructing the protoype machines; NTNU's Service Lab for their logistical and technical support of my experimental setups; Saurabh Tewari, for the many hours he has spent reading my paper drafts, providing technical guidance, and sharing an occasional beer; Kristin Bjerke, for her enthusiastic support of my work and providing my wife and me with an adoptive Norwegian family; Apurva, Ashish, Astrid, Fritz, Gysler, Kartik, Kaushik, Maggi, Nathalie, Nathan, Rohit, Ruben, Santhosh, Santiago, Shanker, Srikant, Sverre, Vince, Visweshwar, Zhang, and the numerous other friends I have made along the way who have made this all worthwhile.

I would like to acknowledge Karsten Moholt AS, and especially Linn Moholt, for installing windings on the prototype machines; Infolytica Corp and Chad Ghalamzan for providing me with finite element analysis tools and support; my father, Verne Severson, and John Hardy Jr. from Forward Pay Systems, Inc. for assistance with the power electronic drive fabrication; the Norwegian Centre for International Cooperation in Education (SIU) for providing funding to start my collaboration with NTNU; the Office of Naval Research (ONR) for providing financial support; and the National Science Foundation, the Department of Defense, and the University of Minnesota for providing me with six years of fellowship funding in the form of the GRFP, NDSEG Fellowship, and the Doctoral Dissertation Fellowship. I would also like to thank my dissertation committee for their careful review of my work.

Finally, I would like to thank Marie Vera for adding urgency to complete my PhD.

Dedication

To Ann Marie Severson

Abstract

The increasing ownership of electric vehicles, in-home solar and wind generation, and wider penetration of renewable energies onto the power grid has created a need for grid-based energy storage to provide energy-neutral services. These services include frequency regulation, which requires short response-times, high power ramping capabilities, and several charge cycles over the course of one day; and diurnal load-/generation-following services to offset the inherent mismatch between renewable generation and the power grid's load profile, which requires low self-discharge so that a reasonable efficiency is obtained over a 24 hour storage interval. To realize the maximum benefits of energy storage, the technology should be modular and have minimum geographic constraints, so that it is easily scalable according to local demands. Furthermore, the technology must be economically viable to participate in the energy markets.

There is currently no storage technology that is able to simultaneously meet all of these needs. This dissertation focuses on developing a new energy storage device based on flywheel technology to meet these needs. It is shown that the bearingless ac homopolar machine can be used to overcome key obstacles in flywheel technology, namely: unacceptable self-discharge and overall system cost and complexity.

Bearingless machines combine the functionality of a magnetic bearing and a motor/generator into a single electromechanical device. Design of these machines is particularly challenging due to cross-coupling effects and trade-offs between motor and magnetic bearing capabilities. The bearingless ac homopolar machine adds to these design challenges due to its 3D flux paths requiring computationally expensive 3D finite element analysis. At the time this dissertation was started, bearingless ac homopolar machines were a highly immature technology. This dissertation advances the state-of-the-art of these machines through research contributions in the areas of magnetic modeling, winding design, control, and power-electronic drive implementation. While these contributions are oriented towards facilitating more optimal flywheel designs, they will also be useful in applying the bearingless ac homopolar machine in other applications. Example designs are considered through finite element analysis and experimental validation is provided from a proof-of-concept prototype that has been designed and constructed as a part of this dissertation.

Contents

List of Tables

List of Figures

Chapter 1

Introduction

1.1 Distribution grid-based energy storage

1.1.1 Motivation

Recently, the electric power grid has seen an increase in wind and solar generation as well as increasingly volatile loads from electric vehicles (EVs). The integration of available renewable generation is mandatory and has the effect of displacing a market's highest cost generators. These generators often have the fastest response time and the highest ramp rates and are therefore typically those best-suited for providing frequency regulation and load following services to the power grid [1]. Renewable generation is typically unable to provide regulation and its variability can actually increase the need for regulation. This means that one result of adding renewable generation to a market is a reduction in the market's regulation capacity which, combined with sudden changes in distribution grid load due to EV charging, decreases the reliability of the power grid. Additionally, there is a diurnal generation cycle present in the renewable technology that does not match the power grid's diurnal load cycle, causing more volatile energy prices. At current levels of renewable generation, the threats posed by these problems have been shown to be manageable. However, with initiatives to significantly increase renewable penetration, such as the Department of Energy's "20% wind by 2030," and the continued integration of renewable vehicles, these issues will need to be addressed. Both frequency regulation and diurnal load following services are energy neutral and, because generators must deliver a net positive amount of energy to the grid, it is suggested in [1–7] that energy storage devices be used to provide these services.

To maximize the benefits of energy storage, this dissertation proposes locating storage modules on the distribution grid, near points of congestion. This would allow the grid operator to direct bulk energy to points of anticipated load when it is most optimal to do so, i.e. so as to increase transmission efficiency or avoid curtailing renewable generation when load is lacking (diurnal load following). These devices could simultaneously provide frequency regulation services in response to local grid conditions to increase the grid stability. Moreover, locating energy storage near points of load would enable the grid infrastructure (transformers and transmission lines) to operate closer to the average load, enabling utilities to avoid costly upgrades due to large peak loads, such as those associated with electric vehicles. A similar use-case was considered in [7], for flywheel systems providing load-following and smoothing services at various locations on the distribution grid.

1.1.2 Requirements of an energy storage device

The requirements of implementing distribution-grid energy storage that is able to simultaneously provide frequency regulation and diurnal load-following services are numerous and diverse. Frequency regulation has energy transfer time requirements on the order of seconds to several minutes and is typically energy neutral on a time scale of a half-hour [2,3]. Energy storage devices that provide frequency regulation must have a long cycle-lifetime, high power ratings, short response times, and fast ramp rates. To understand how extreme the cycle-lifetime requirements are, consider data published by Beacon Power which indicates that their frequency regulation facility in New York experiences 2500 - 5000 charge cycles per year [8]. Finally, because frequency regulation is power-intensive, the energy storage device must have a reasonable cost per installed kW.

Diurnal load following services have energy transfer times on the order of several hours and are energy neutral over a period of 24 hours [7]. This means that energy storage devices must have a low self-discharge rate so that a meaningful amount of energy can be stored for a 24 hour period. Furthermore, load-following services are energy-intensive, which requires storage devices to have both a reasonable energy density and cost per kWh stored.

Suitable distribution-grid energy storage must have a modular form factor so that it is easily installed regardless of geographic location or population density and easily scalable based on the local grid requirements. Since it will be installed in small quantities that are staggered throughout the grid, it must be low maintenance.

In summary, the key requirements of an energy storage device for this application are: long cycle-lifetime, low self-discharge rate, modular form factor, and reasonable cost and size per kW as well as per kWh.

1.1.3 Overview of energy storage technologies

Storage technologies that are typically considered for grid applications include pumped hydro, compressed air, thermal, ultracapacitors, chemical batteries, and flywheel technology. Many published studies have evaluated these different storage technologies for use on grid. For example, [2–6, 9, 10] which suggest that conventional storage technology is inadequate to meet the needs summarized in Section 1.1.2:

- Pumped hydro and compressed air: these technologies have been economically developed in large, centralized installations where they achieve round-trip efficiencies on the order of 60-80%, but are limited by geographic restrictions and environmental concerns.

- Small scale compressed air and thermal: these technologies suffer from low round-trip efficiencies.

- Ultracapacitors: this technology is regarded as having a cost per kWh that is too high and an energy density that is too low for the bulk storage required for diurnal load following.

- Various types of chemical batteries: these technologies are generally regarded favorably for diurnal storage applications, but contain hazardous chemicals and suffer from low cycle-lifetimes which limit their use for frequency regulation. Table 1.1 shows a comparison of several different chemical batteries. Alternative technologies, such as sodium-sulfur and flow batteries, have much longer cycle-lifetimes, but require large installations, making them non-modular and therefore

Table 1.1: Typical chemical battery properties [10]

	Lead-acid	**Li-Ion**	**NiMH**
Capital cost / kWh	\$35 - \$350	\$215 - \$1070	\$285 - \$1425
Round-trip efficiency[a]	56.5 - 76.5%	76.5 - 81%	58.5 - 67.5%
Lifetime cycles	200 - 1500	~3000	1500 - 2000
Energy density (kWh/m^3)	60 - 130	150 - 400	80 - 300
Specific energy (Wh/kg)	25 - 35	60 - 180	50 - 100

---

[a] Assumes a power-electronic interface efficiency of 95% and does not take into account loss of efficiency due to climate control.

not well-suited for distribution grid applications.

- Flywheels: this technology has been commercialized for providing frequency regulation due to its long cycle-lifetime, modularity, high power density, and lack of environmentally hazardous chemicals. A 2004 study concluded that flywheels are the most economical form of energy storage for storage-intervals under 10 minutes [2]. However, this technology suffers from high self-discharge losses, resulting in low round-trip efficiencies for the longer storage intervals required by diurnal load following; this technology is further described in Section 1.2.

1.2 Flywheel systems

1.2.1 Overview of conventional flywheel systems

Flywheel systems store mechanical energy in a rotating flywheel. An example of a conventional flywheel energy storage module is shown in Fig. 1.1. The flywheel is connected to a motor/generator which "charges," or converts electrical energy into mechanical energy, by increasing the flywheel's rotational speed; and "discharges," or converts mechanical energy into electrical energy, by slowing the flywheel down, similar to regenerative braking in an electric vehicle. The motor is usually permanent magnet, but sometimes synchronous reluctance, switched reluctance, or induction motors are used. Depending on the design, these modules may use a cylindrical steel, fiber glass, or carbon composite flywheel. The flywheel is typically located in a vacuum chamber to lower

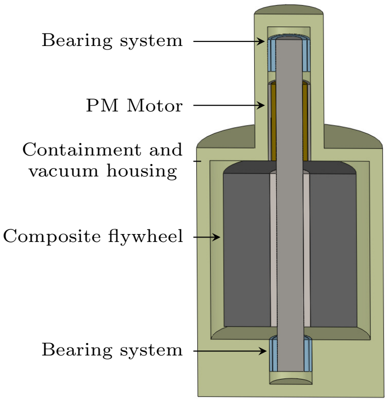

Figure 1.1: Typical flywheel system design

wind-resistance losses and suspended via active magnetic bearings to reduce drag and reliability concerns. To achieve optimal energy density and form factor, high rotational speeds are typically required (10 kRPM – 100 kRPM). For high-speed units, a containment structure is required to prevent flywheel shards from escaping the module and causing damage or harm in the event of a flywheel failure.

1.2.2 Flywheel materials

Most flywheels can be approximated as a hollow cylinder, as drawn in Fig. 1.2. The amount of stored kinetic energy of a rotating flywheel is calculated by:

$$\begin{aligned} E &= \frac{1}{2} I \omega^2 \\ &= \frac{1}{4} m v_{\text{tip}}^2 \left(1 + \frac{r_{\text{in}}^2}{r_{\text{out}}^2}\right) \\ &= \frac{\pi}{4} L \rho v_{\text{tip}}^2 \left(r_{\text{out}}^2 - \frac{r_{\text{in}}^4}{r_{\text{out}}^2}\right) \end{aligned} \tag{1.1}$$

where I is the flywheel's moment of inertia, ω is the angular rotational speed, m is the flywheel mass, ρ is the flywheel material mass density, and $v_{\text{tip}} = \omega r_{\text{out}}$ is the linear surface speed of the material at the flywheel's outer-radius. Flywheel materials can be viewed as having a maximum surface speed, beyond which the material will breakdown. This maximum surface speed is a function of the material's tensile strength and mass density. There is a trade-off in material selection between the mass density

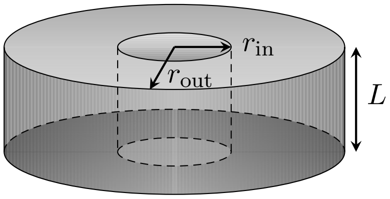

Figure 1.2: Example flywheel

Table 1.2: Comparison of flywheel materials

	ρ(kg/m^3)	v_{tip}(m/s)	kWh/m^3	Wh/kg
Carbon Fiber	1600	700 - 940	54 - 98	34 - 61
Fiber Glass	1600	500 - 600	28 - 40	17 - 25
Steel	7800	200 - 300	22 - 49	3 - 6

and maximum surface speed, where materials with larger v_{tip} typically have smaller values for ρ. Since (1.1) shows that the amount of energy stored increases quadratically with maximum surface speed and only linearly with mass, lighter and stronger flywheel materials lead to more energy-dense designs.

Equation (1.1) can be re-written to approximate the theoretical maximum specific energy and energy density for a given material:

$$\frac{E}{m} \approx \frac{v_{\text{tip}}^2}{4}, \qquad \text{when } r_{\text{in}}^2 << r_{\text{out}}^2 \tag{1.2}$$

$$\frac{E}{V} \approx \frac{\rho v_{\text{tip}}^2}{4}, \qquad \text{when } r_{\text{in}}^4 << r_{\text{out}}^4. \tag{1.3}$$

These values are calculated in Table 1.2 for typical flywheel materials, where v_{tip} represents the maximum surface speed that can be safely used. Carbon fiber leads to the most energy dense designs with steel and fiber glass overlapping as a distant second. In terms of specific energy (energy per unit mass), which has important implications for the axial bearing design, carbon fiber is also clearly at a significant advantage. In comparing Table 1.1 and Table 1.2, it is seen that carbon fiber flywheel designs have lower energy density than battery designs but outperform lead acid batteries in specific energy.

To appreciate the impact of ρ, v_{tip}, and rotational speed on the flywheel's form factor, example flywheel dimensions are calculated in Table 1.3 for maximum rotational

Table 1.3: Example flywheel dimensions

			6 kRPM[a]		36 kRPM	
	Mass	Volume	L	r_{out}	L	r_{out}
Carbon Fiber	163kg	0.10 m^3	0.01m	1.5m	0.52m	0.25m
Fiber Glass	400kg	0.25 m^3	0.09m	1.0m	3.1m	0.16m
Steel	1600kg	0.21 m^3	0.29m	0.5m	10.3m	0.08m

---

[a] Dimensions required to store 10 kWh of energy with $r_{\text{in}} = 0$. All calculations are made using the largest tip speed in the range provided in Table 1.2. To obtain the maximum energy density, the outer radius of the flywheel is fixed at the maximum allowable value using $r_{\text{out}} = v_{\text{tip}}/\omega$.

speeds of 6 kRPM and 36 kRPM. From this table it is evident that higher speeds result in reasonable form factors for carbon fiber flywheels, while lower speed designs are more reasonable for steel flywheels.

Finally, it should be noted that typical designs only operate over half of their speed range and are therefore only able to extract 75% of the energy stored. This is done to ease requirements on the motor design. It is typically desired for the flywheel module to maintain a constant power over its entire speed range and the output power of the motor is given by

$$P = \omega\tau \tag{1.4}$$

where τ is motor's output torque. To maintain a constant power, torque must vary inversely to ω, which requires unrealistic values as the rotational speed approaches zero.

1.2.3 Commercial products

Flywheel energy storage is a mature technology for applications which require short storage intervals, long cycle-life, fast response times, high power, and low energy stored. Examples include providing regulation on the power grid; providing/absorbing peak power needed for acceleration in more-electric vehicles, such as trains and sea-port gantry cranes; providing ride-through power in uninterruptible power supplies (UPS) between the occurrence of a disruption on the AC mains and when a backup generator powers up [5, 8, 9, 11–15]. Several companies which either have commercialized or are in the process of commercializing products based on flywheels are listed below.

- Beacon Power LLC has constructed two flywheel facilities to provide large-scale frequency regulation services on the order of 20 MW through flywheel modules connected in an array [12]. The modules use a carbon-fiber flywheel operating at up to 16,000 RPM, weigh 1130 kg, utilize a 100 kW permanent magnet motor, store 25 kWh, and have a typical round-trip efficiency of 84% for the short storage intervals required by frequency regulation.

- PowerThru (formerly Pentadyne Power Corporation) and Active Power, Inc. have developed UPS systems that utilize flywheel energy storage. PowerThru's design utilizes a 190 kW, 4-pole synchronous reluctance motor/generator operating at 52,000 RPM and a carbon composite flywheel that stores approximately 750 Wh. Each unit weighs approximately 590 kg and has a volume of 960 liters. The self-discharge losses are 250 W, which means that a unit will dissipate its stored energy after idling for only a few hours [13].

- VYCON, Inc. has commercialized flywheel energy storage units for use in sea port cranes. Their modules operate inside a vacuum chamber and utilize a 150 kW permanent magnet motor with a maximum speed of 36,000 RPM, a steel flywheel that stores 1.27 kWh, active magnetic bearings, and weigh 320 kg [14]. The required energy storage time is on the order of minutes.

- Rotonix USA, Inc. has commercialized flywheel devices for several different applications. Their modules have a 1.1MW power rating, use a carbon compoite flywheel that stores 12 kWh, have self-discharge losses of 500 W, weigh 2700 kg, and use magnetic bearings [16]. Unlike other companies, this flywheel system uses an outer-rotor motor design to increase the energy density, but no information is available on the type of motor used. At this self-discharge rate, the flywheel will dissipate its stored energy over the course of one day.

- Amber Kinetics, Inc. focuses on low-cost flywheel products for custom applications, which have included power smoothing and uninterruptible power supplies. They have ongoing projects with the Blue Planet Research in Hawaii and San Diego Gas and Electric in California. Their systems use steel flywheels but no other design information is available [17].

1.2.4 Problems with current technology

Flywheel technology has already been shown to be feasible for providing frequency regulation, but is currently not usable for providing diurnal load following services due to its high self-discharge rate while idling, with the best flywheel designs completely self-discharging over a period of one day. Secondary concerns with flywheel modules are the overall cost and manufacturing complexity.

The sources of self-discharge losses include bearing loss, frictional windage loss due to the high rotational speed, and magnetic losses associated with the motor and, in some designs, magnetic bearings. Bearing losses can be minimized through use of magnetic bearings with optimized magnetic circuit design to minimize flux variability [18] or by implementing high-temperature superconducting bearings [19] at the expense of cost and complexity. For most designs, frictional windage losses can be reduced to nearly negligible levels by using a vacuum of less than 1 mTorr [20]. Magnetic losses associated with the motor remain a key concern and are one of the primary areas the proposed use of the ac homopolar motor addresses. Motors that use permanent magnets will inherently have losses while they are freewheeling due to hysteresis and induced eddy currents from the rotating magnetic fields. Traditional machines without permanent magnets have other complications:

- Induction and switched reluctance motors have increased rotor heating which limits the energy transfer time of the flywheel module before the motor/generator must idle to prevent overheating, a consequence of the rotor being levitated on magnetic bearings and operating in a vacuum where the only mechanism for heat exchange is radiation.

- Wound-rotor and doubly-fed motors require brushes that are not usable for high-speed operation.

- Synchronous reluctance motors require a high L_d/L_q ratio which leads to a rotor structure that is not mechanically robust for high-speed operation.

1.2.5 Relevant flywheel research projects

There are many recent and ongoing research projects in flywheel technology, for example: [19–45]. To increase the energy density, integrating the flywheel into the motor has been proposed to various extents [22, 24, 25]. The traditional topology, depicted in Fig. 1.1, is at one extreme of this spectrum, where the flywheel is mounted on a shaft at a separate axial location from the motor. At the other extreme, designs where the motor's rotor is the flywheel have been considered [27] as well as designs where an outer-rotor motor is used and the flywheel is mounted directly on the motor's rotor, as described later in Fig. 1.3a.

Efforts to reduce self-discharge losses have taken several different approaches. Projects focused on improving permanent magnet motors have included investigations into Halbach configurations and core-less stators [35, 37], which resulted in reduced power and energy density, as well as an investigation into a design with a removable stator that was retracted from the rotor during idling times [42], which has the negative consequences of reducing the system's energy density, increasing the response time, and increasing the overall system cost and complexity. Other efforts have focused on magnetic bearing losses and have looked at optimizing active and hybrid magnetic bearings [38, 39] as well as using superconducting bearings [19, 21, 25].

There are numerous examples of recent investigations into the use of bearingless motors for flywheel energy storage, including [30, 43–45]. Bearingless designs combine the functionality of magnetic bearing and a motor into a single device and as such are theoretically able to reduce the overall flywheel system size, amount of raw materials needed, and the manufacturing complexity. All types of traditional motors can be redesigned as bearingless motors with varying consequences to the overall machine performance. One significant drawback of conventional bearingless motors is that they utilize a separate set of windings to produce magnetic bearing forces which must share the same slot space as the torque windings. This creates a trade-off between the magnetic bearing and motor capabilities and is an issue that is explored in this dissertation.

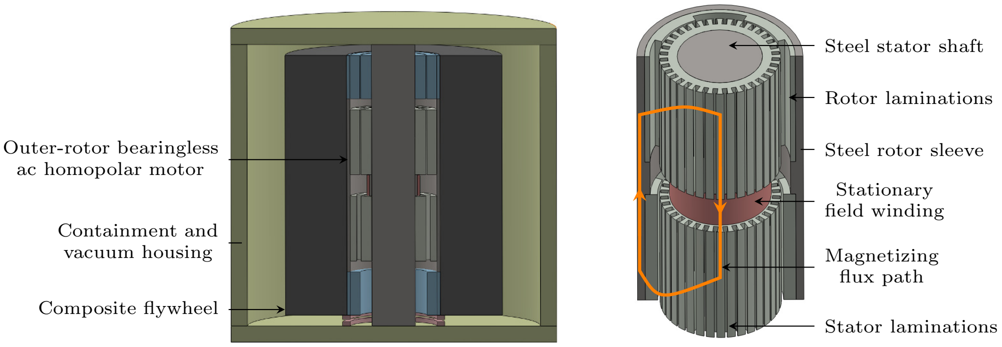

(a) Proposed flywheel system design (b) Bearingless ac homopolar motor

Figure 1.3: Proposed flywheel system design

1.3 Proposed flywheel system

This dissertation proposes the flywheel module topology depicted in Fig. 1.3. The proposed design has the following key features:

- AC homopolar motor to eliminate motor losses while idling. The ac homopolar motor is completely stator-side current excited. This means that during times of idling, the magnetization can be removed by turning all current off, and therefore self-discharge losses from the motor can be eliminated. The ac homopolar motor avoids the previously mentioned pitfalls of traditional motors which either suffer from rotor loss, the required use of brushes, or non-robust rotor structure. Furthermore, because the machine uses current excitation, the excitation level can be varied based on the flywheel system's current rotational speed to reduce losses in the power electronic motor drive during times of energy transfer.

- Integrated design topology to increase the energy and power density of the flywheel system. The motor is implemented in an outer-rotor fashion where the rotor forms the inner backing for a carbon composite flywheel. Since, as is shown by (1.1), most of the flywheel's energy is stored near the flywheel's outer-radius, hollowing the flywheel out does not result in a sizable reduction in the amount of energy stored; instead, this dramatically increases the flywheel system's overall energy density as the flywheel and the motor are now able to occupy the same volume.

- Bearingless motor to reduce the system size, cost, and manufacturing complexity. By using a bearingless version of the ac homopolar motor, the need for separate radial magnetic bearings is eliminated. This reduces the amount of raw materials required and, because active magnetic bearings are complex electromechanical devices with their own stator windings, reduces the required manufacturing effort. Note that an axial thrust bearing is still required to support the flywheel's weight. However, this can be implemented with a very simple permanent magnet passive bearing design.

1.4 Research contributions

The results of this project have resulted in the following papers either published or submitted for publication: [46–55]. The individual contributions can be summarized as:

- exploring the application of bearingless ac homopolar machines to flywheel energy storage;
- developing magnetic eqivalent circuit (MEC) models of the ac homopolar machine that are suitable for use in the design process; these models can be solved in a fraction of a second as opposed to transient 3D finite element models which have a solve time on the order of days;
- developing a design procedure and constraints for dual purpose no voltage (DPNV) windings; these windings allows the same stator coils to be used for both radial force and torque production and thereby increase the machine's torque density; the results of this contribution as well as the next item apply generally to all types of radial flux bearingless machines;
- proposing and evaluating different power-electronic drive implementations for DPNV windings;
- designing a prototype bearingless ac homopolar motor and presenting experimental validation of the above contributions; because relatively little literature exists on the bearingless ac homopolar machine, the publication of experimental data is particularly valuable to the bearingless machines community.

1.5 Dissertation outline

- Chapter 2 introduces the bearingless ac homopolar machine and derives its operating principles from a drives perspective.
- Chapter 3 explores the application of the ac homopolar machine for flywheel energy storage. A macroscopic design sizing approach is investigated and compared against results from 3D FEA.
- Chapter 4 develops and validates a MEC of the ac homopolar machine that is suitable for design optimization.
- Chapter 5 presents the rigid body rotor model for the suspension of the bearingless ac homopolar machine and investigates the impact of variable excitation on the model.
- Chapter 6 derives the necessary conditions to realize DPNV windings, proposes a design procedure, and explores several example bearingless motor designs using DPNV windings.
- Chapter 7 proposes and evaluates implementations of power-electronic drives for DPNV-wound motors.
- Chapter 8 describes the prototype design of the bearingless ac homopolar machine, including the power electronic drive and controllers, and presents experimental results.
- Chapter 9 presents the dissertation conclusions and proposes future work.

Chapter 2

Model of the Bearingless AC Homopolar Motor

This chapter investigates the bearingless ac homopolar motor from a drives perspective. Idealized machine quantities are assumed, such as sinusoidally distributed windings and infinite iron permeability. The point of the chapter is to describe how the motor and magnetic bearing functionality work and derive simple inductances matrices as well as torque and force expressions that will be used later when developing a drive for the machine. Note that while the overall goal of the dissertation is to develop an outer-rotor bearingless motor for flywheel energy storage, in this chapter (as well as in several other chapters) an inner-rotor motor is considered. Since the same results and theory apply to both the inner- and outer-rotor variants, this is done to be consistent with the hardware prototype that was developed (described in Chapter 8).[1]

2.1 Introduction

Classical bearingless motors require that a suspension winding produce a revolving $p\pm2$-pole flux density to disrupt the otherwise symmetric, revolving p-pole magnetic field in the motor's airgap [56, 57]. This requires high-bandwidth angular-position sensors and an *ac suspension current* to produce a constant force. Alternatively, the bearingless

---

[1] Portions of the material in this chapter have also been published in [52] and submitted for publication in [48].

consequent-pole motor has been developed which utilizes a 2-pole suspension winding with a *dc current* to produce a constant radial force for a $p \geq 8$-pole motor [56, 58]. However, this motor has permanent magnets on its rotor, making it not applicable to superconducting applications; less desirable for variable-speed applications, such as flywheel energy storage, where a controllable excitation is desired; and difficult to implement in high-speed applications where securing the magnets to the rotor becomes a challenge. For such applications, the bearingless ac homopolar motor is best suited.

Like the bearingless consequent-pole motor, a $p \geq 8$-pole bearingless ac homopolar motor is able to produce a constant radial suspension force with a dc current. Unlike the consequent-pole motor, the homopolar motor is magnetized through a dc field winding secured to the stator, allowing for variable excitation. Since the field winding is stationary, no brushes are required and, in the case of a superconducting coil, coolant does not need to be pumped into the rotor. The rotor's structure is therefore very simple and conducive to high-speed operation. One important drawback of the ac homopolar motor is that its theoretical torque density is roughly one-half that of a classical synchronous motor. The motor's torque density can be somewhat improved in the case of a superconducting machine where the field winding is able to provide a very large excitation [59]. It is shown in Chapter 3 that when losses are normalized when comparing this machine to other synchronous machines, the discrepancy in torque density disappears.

There have been several papers considering the ac homopolar motor, but little literature on the *bearingless* ac homopolar motor [56, 60–62]. The ac homopolar motor has attracted recent attention as a high speed machine, a superconducting machine, an alternator operated with a rectifier for capacitor charge power supplies, and in the dissertation's application of flywheel energy storage [27, 51, 63–69]. In flywheel energy storage, the ac homopolar machine has been considered in both outer and inner rotor configurations [27,51,69] with varying degrees of rotor/flyweel integration. It was shown in [27] that a solid steel rotor can be used, which in this case also served as the flywheel, while still achieving acceptable losses. As a bearingless motor, existing literature has focused on the suspension force capability [56, 60–62], neglecting the complete bearingless machine model and only considering a single rotor geometry. In [62], it was shown that acceptable suspension performance can be achieved for 6-pole configurations via

Table 2.1: Chapter nomenclature

$B_{j,l}$, $B_{j,u}$	Flux density produced by winding phase-j in the lower (l) and upper (u) airgap.
$\mathcal{F}_j$	MMF waveform of winding phase-j.
F_x, F_y	Force acting on the rotor in x and y direction.
g_l, g_u	Lower and upper airgap length profile.
$g_{\max}$, $g_{\min}$	Maximum and minimum length of airgap.
l	Axial length of one rotor segment.
n_j	Conductor turn density of winding phase-j.
N_f	Number of turns in the field winding.
N_s	Number of turns in a torque winding phase.
N_{ss}	Number of turns in a suspension winding phase.
p	Number of poles.
r	Mean airgap radius in minimum airgap region.
δ_j	Angle of winding phase-j axis: $\delta_a = 0$, $\delta_b = \frac{2\pi}{3}$, $\delta_c = -\frac{2\pi}{3}$, $\delta_x = 0$, and $\delta_y = \frac{\pi}{2}$.
$\lambda_{j,k}$	Flux produced by winding phase-k that links winding phase-j.
ϕ_{rs}	Angle measured from the rotor's direct axis.
ϕ_{ss}	Angle measured from phase a-axis.
θ_{ms}	Angle between the rotor's direct axis and phase a-axis.
τ	Torque produced on the rotor.

creative winding design, which enables lower electrical frequencies at high rotational speeds than the conventionally used 8-pole configuration.

In this chapter: the complete bearingless motor model is developed. Motor/generator operation is first considered, three choices of suspension winding configurations are then presented, suspension force expressions are developed, and finally it is shown that certain configurations of suspension windings can be used to magnetize the machine. Nomenclature used throughout the chapter is defined in Table 2.1.

2.2 Description of bearingless ac homopolar motor

A 3D sketch of the ac homopolar motor is shown in Fig. 2.1a where it can be seen that the rotor consists of two sections of salient iron poles connected by a shaft. The iron poles are rotated 180° electrically from each other. The iron may be shaped to alter the airgap profile and therefore the magnetic flux density distribution produced by the field winding. The two most common airgap profiles are considered in this chapter: *sinusoidal* and *square*. The stator consists of a back-iron and three sets of windings:

1) *Field Winding*: dc winding that encircles the rotor but is fixed to the stator and used to magnetize the machine. The magnetizing flux path, depicted in Fig. 2.1a, is both axial and radial.

2) *Torque Winding*: 3-phase winding that spans the full axial length of the motor. This is the standard $\geq$ 2-pole winding found in synchronous machines.

3) *Suspension Winding*: set of 2-phase, 2-pole windings that are responsible for producing the radial suspension forces. This winding set shares the same slots as the torque winding but extends in the axial direction only the length of one of the rotor segments. A separate suspension winding extends along the other rotor segment allowing for conical tilting to be corrected in addition to radial displacement.

2.2.1 Torque production

Both reluctance and alignment torque can be present in the ac homopolar motor. However, it will be shown in section 2.3 that it is possible to design the motor to lack either type of torque. The radial cross-section shown in Fig. 2.1b can be used to understand the alignment torque. By looking down the rotor axially, the iron magnetized as north poles on one end will appear beside magnetized south poles from the other end. As the rotor spins, the torque winding, which spans the full axial length of the rotor, will see alternating north and south poles.

2.2.2 Suspension force production

Radial suspension force production can be understood by again considering a radial cross-section. Referring to Fig. 2.1c, this time only looking at one of the rotor sections,

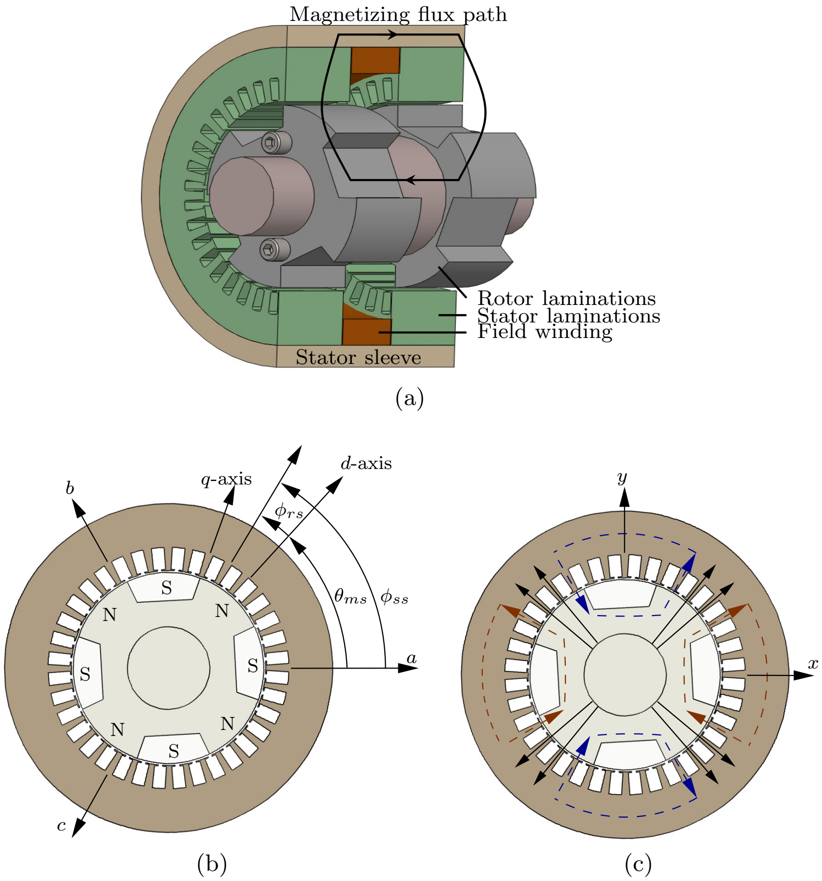

(a)

(b)

(c)

Figure 2.1: Bearingless ac homopolar motor: (a) full motor with square airgap profile, (b) magnetized cross-section depicting the notation for angles and phase axes, (c) cross-section depicting flux paths for suspension windings given a positive terminal current; blue lines correspond to the x-phase winding, brown lines correspond to the y-phase winding, and the black lines are the magnetization flux.

the flux path of the 2-phase, 2-pole suspension winding can be seen. Note that most of the flux will cross the airgap where an iron pole is present. The superposition of this flux onto the magnetizing flux leads to a radial force and when an ac homopolar motor has eight or more poles this force is independent of the rotor's angular position. This means that the radial forces can be controlled with a dc current–a key feature of the ac homopolar motor and something that conventional bearingless motors do not possess [56].

2.3 Analysis of torque production

The analytical model of the ac homopolar motor is now developed for two different rotor types. For each type, an inductance matrix and torque expression is derived. In this section, the machine is studied purely as a motor/generator; analysis of torque due to the suspension windings is deferred to section 2.7. The methodology presented in [70,71] is followed. As will be shown, the terminal characteristics of the ac homopolar motor are the same as that of a synchronous generator.

An ideal, sinusoidally-distributed, 3-phase torque winding is assumed with the following conductor density for each phase (substitute j for the phase of interest – a, b, or c):

$$n_j\left(\phi_{ss}\right) = \frac{N_s}{2}\sin\left(\frac{p}{2}\phi_{ss}-\delta_j\right)$$

It is assumed that the iron of the machine has infinite permeability, flux only crosses the airgap radially, and the flux density does not vary in the radial direction within the airgap. Under these assumptions, it can be shown that the MMF generated by the sinusoidally distributed torque windings is the same as a classical radial flux machine:

$$\mathcal{F}_j\left(\phi_{ss}\right) = \frac{N_s}{p}\cos\left(\frac{p}{2}\phi_{ss}-\delta_j\right)i_j \tag{2.1}$$

The MMF generated by the field winding acts upon the top and bottom airgaps in opposite directions and is uniform along the circumference of the airgaps:

$$\mathcal{F}_{f,u} = \frac{N_f i_f}{2} \tag{2.2}$$

$$\mathcal{F}_{f,l} = -\mathcal{F}_{f,u} \tag{2.3}$$

The airgap length profile for each type of rotor is given by the functions $g_u\left(\phi_{rs}\right)$ and $g_l\left(\phi_{rs}\right)$ for the upper and lower airgap segments respectively, as defined in sections 2.3.1 and 2.3.2. Referring to Fig. 2.1b, it can be seen that $\phi_{rs} = \phi_{ss} - \theta_{ms}$. Using this relation, the flux densities can be expressed in terms of ϕ_{ss} and θ_{ms} for $j = a$, b, c, or f:

$$\begin{aligned} B_{j,u}\left(\phi_{ss},\theta_{ms}\right) &= \frac{\mu_0 \mathcal{F}_j\left(\phi_{ss}\right)}{g_u\left(\phi_{ss}-\theta_{ms}\right)} \\ B_{j,l}\left(\phi_{ss},\theta_{ms}\right) &= \frac{\mu_0 \mathcal{F}_j\left(\phi_{ss}\right)}{g_l\left(\phi_{ss}-\theta_{ms}\right)} \end{aligned}$$

The flux produced by the phase-j winding that links a single-turn torque winding coil, which spans 180° electrical and is centered at angle ϕ_{ss}, is given by ($j = a$, b, or c):

$$\begin{aligned} \Phi_j\left(\phi_{ss},\theta_{ms}\right) &= \int_{\phi_{ss}-\frac{\pi}{p}}^{\phi_{ss}+\frac{\pi}{p}} B_{j,u}\left(\xi,\theta_{ms}\right) rl\,\mathrm{d}\xi \\ &\quad + \int_{\phi_{ss}-\frac{\pi}{p}}^{\phi_{ss}+\frac{\pi}{p}} B_{j,l}\left(\xi,\theta_{ms}\right) rl\,\mathrm{d}\xi \\ &= \mu_0 rl \int_{\phi_{ss}-\frac{\pi}{p}}^{\phi_{ss}+\frac{\pi}{p}} \frac{\mathcal{F}_j\left(\xi\right)}{g'\left(\xi-\theta_{ms}\right)}\,\mathrm{d}\xi \end{aligned}$$

Here, $g'\left(\phi_{rs}\right)$ can be interpreted as an *effective airgap*, given by (2.4). This idea of an effective airgap allows for easy comparison of the ac homopolar motor to classical machines and will be explored more later.

$$g'\left(\phi_{rs}\right) = \frac{g_u\left(\phi_{rs}\right)\, g_l\left(\phi_{rs}\right)}{g_u\left(\phi_{rs}\right) + g_l\left(\phi_{rs}\right)} \tag{2.4}$$

The winding flux linkages can now be calculated. For the torque windings:

$$\lambda_{j,k}\left(\theta_{ms}\right) = \frac{p}{2}\int_{\left(\delta_j-\frac{\pi}{2}\right)\frac{2}{p}}^{\left(\delta_j+\frac{\pi}{2}\right)\frac{2}{p}} n_j(\phi_{ss}+\tfrac{\pi}{p})\,\Phi_k\left(\phi_{ss},\theta_{ms}\right)\,\mathrm{d}\phi_{ss} \tag{2.5}$$

For the field winding:

$$\begin{aligned} \lambda_{f,j}\left(\theta_{ms}\right) &= N_f \int_0^{2\pi} B_{j,u}\left(\phi_{ss},\theta_{ms}\right) rl\,\mathrm{d}\phi_{ss} \\ \lambda_{f,f}\left(\theta_{ms}\right) &= N_f \int_0^{2\pi} B_{f,u}\left(\phi_{ss},\theta_{ms}\right) rl\,\mathrm{d}\phi_{ss} \end{aligned}$$

When the airgap functions $g_u(\phi_{rs})$ and $g_l(\phi_{rs})$ are defined, the inductance matrix can be constructed. For the cases considered in this chapter, the inductance matrix takes the following form:

$$\begin{Bmatrix} \lambda_a \\ \lambda_b \\ \lambda_c \\ \lambda_f \end{Bmatrix} = \begin{bmatrix} L_{a,a} & L_{a,b} & L_{a,c} & L_{a,f} \\ L_{a,b} & L_{b,b} & L_{b,c} & L_{b,f} \\ L_{a,c} & L_{b,c} & L_{c,c} & L_{c,f} \\ L_{a,f} & L_{b,f} & L_{c,f} & L_{f,f} \end{bmatrix} \begin{Bmatrix} i_a \\ i_b \\ i_c \\ i_f \end{Bmatrix} \tag{2.6}$$

for the phase windings, where j and $k = a$, b, or c:

$$\begin{aligned} L_{j,j} &= L_{ls} + L_0 + L_g \cos(p\theta_{ms} + \delta_j) \\ L_{j,k} &= -\frac{1}{2}L_0 + L_g \cos(p\theta_{ms} - \delta_j - \delta_k) \end{aligned}$$

for the inductance terms involving the field winding, where $j = a$, b, or c:

$$\begin{aligned} L_{j,f} &= L_{f0} \cos\left(\frac{p}{2}\theta_{ms} - \delta_j\right) \\ L_{f,f} &= L_{lf} + L_f \end{aligned}$$

Here, L_g, L_0, L_{f0}, and L_f depend on the rotor shape and will be calculated later; L_{ls} and L_{lf} are leakage inductance terms and are not practical to calculate in this derivation.

To remove the dependence on rotor position and thereby simplify the equations, the system can be cast into an equivalent d-q form. The transformation as presented in [72] is used with the d-winding axis aligned with the rotor as shown in Fig. 2.1b, and the d and q windings each having $\sqrt{\frac{3}{2}}N_s$ turns. Following the procedure outlined in [71], (2.6) can be partitioned as:

$$\begin{aligned} \{\lambda_{abc}\} &= [L_{abc}]\{i_{abc}\} + [L_{mf}]\, i_f \qquad (2.7) \\ \lambda_f &= [L_{mf}]^{\mathrm{T}}\{i_{abc}\} + L_{f,f}\, i_f \qquad (2.8) \end{aligned}$$

which can then be transformed into

$$\begin{aligned} \{\lambda_{dq}\} &= [T][L_{abc}][T]^{-1}\{i_{dq}\} + [T][L_{mf}]\, i_f \\ \lambda_f &= [L_{mf}]^{\mathrm{T}}[T]^{-1}\{i_{dq}\} + L_{f,f} i_f \end{aligned}$$

using the following transformation matrix ($\theta_m = \frac{p}{2}\theta_{ms}$):

$$T = \sqrt{\tfrac{2}{3}} \begin{bmatrix} \cos\theta_m & \cos\left(\theta_m - \frac{2\pi}{3}\right) & \cos\left(\theta_m + \frac{2\pi}{3}\right) \\ -\sin\theta_m & -\sin\left(\theta_m - \frac{2\pi}{3}\right) & -\sin\left(\theta_m + \frac{2\pi}{3}\right) \\ 1 & 1 & 1 \end{bmatrix}$$

The resulting system is shown below. Note that the zero-sequence terms have been discarded.

$$\begin{aligned} \begin{Bmatrix} \lambda_d \\ \lambda_q \end{Bmatrix} &= \begin{bmatrix} L_d & 0 \\ 0 & L_q \end{bmatrix} \begin{Bmatrix} i_d \\ i_q \end{Bmatrix} + \begin{bmatrix} L'_{mf} \\ 0 \end{bmatrix} i_f \\ \lambda_f &= \begin{bmatrix} L'_{mf} & 0 \end{bmatrix} \begin{Bmatrix} i_d \\ i_q \end{Bmatrix} + L_{f,f}\, i_f \end{aligned}$$

where:

$$\begin{aligned} L_d &= L_{ls} + \frac{3}{2}\left(L_0 + L_g\right) \\ L_q &= L_{ls} + \frac{3}{2}\left(L_0 - L_g\right) \\ L'_{mf} &= \sqrt{\tfrac{3}{2}} L_{f0} \end{aligned}$$

This gives the following torque expression:

$$\begin{aligned} \tau &= \frac{p}{2}\left(\lambda_d i_q - \lambda_q i_d\right) && (2.9) \\ &= \frac{p}{2} i_q \left(\left[L_d - L_q\right] i_d + L'_{mf}\, i_f\right) \\ &= \frac{p}{2} i_q \left(3L_g i_d + \sqrt{\tfrac{3}{2}} L_{f0}\, i_f\right) && (2.10) \end{aligned}$$

The first term in (2.10) corresponds to reluctance torque and can be derived by considering a classical machine with an effective airgap as defined by (2.4). The second term corresponds to alignment torque and does not fit into the effective airgap paradigm. Therefore the torque production of the ac homopolar motor can be viewed as the superposition of two torque producing motors: a synchronous reluctance motor and a cylindrical synchronous motor.

The torque expressions developed for each rotor structure can be compared against torque expressions derived in textbooks such as [70] for synchronous reluctance and

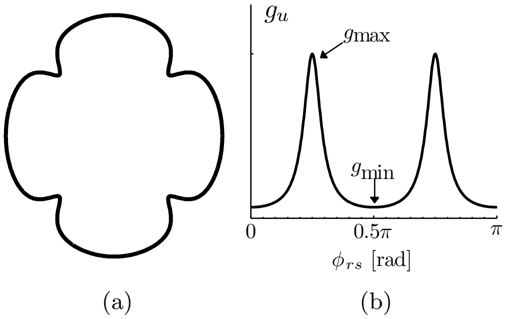

(a) (b)

Figure 2.2: Sinusoidal airgap: (a) Cross-section, (b) Profile; $p = 8$-poles.

wound-rotor synchronous generators. Because the axial length l in torque expressions derived here refers to the axial length of only one of the two rotor segments, it can be shown that the ac homopolar motor has a torque density of approximately one-half that of a classical machine.

2.3.1 Sinusoidal airgap profile

The case of a sinusoidal airgap profile is depicted in Fig. 2.2. The upper and lower airgap profiles are defined as:

$$g_u(\phi_{rs}) = \frac{1}{h_1 + h_2 \cos\left(\frac{p}{2}\phi_{rs}\right)} \tag{2.11}$$

$$g_l(\phi_{rs}) = \frac{1}{h_1 + h_2 \cos\left(\frac{p}{2}\phi_{rs} + \pi\right)} \tag{2.12}$$

where:

$$h_1 = \frac{1}{2}\left(\frac{g_{\max} + g_{\min}}{g_{\max}\, g_{\min}}\right) \tag{2.13}$$

$$h_2 = \frac{1}{2}\left(\frac{g_{\max} - g_{\min}}{g_{\max}\, g_{\min}}\right) \tag{2.14}$$

The effective airgap $g'(\phi_{rs})$ used to calculate the phase inductances is found to be uniform along the rotor circumference – implying that no saliency, and therefore no reluctance torque, is present for the case of a sinusoidal airgap.

$$g'(\phi_{rs}) = \frac{g_{\max}\, g_{\min}}{g_{\max} + g_{\min}} \tag{2.15}$$

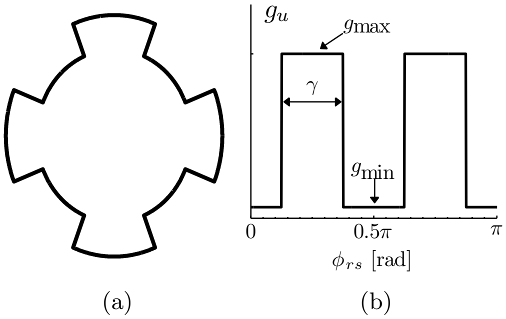

Figure 2.3: Square airgap: (a) Cross-section, (b) Profile; $\gamma = \frac{2}{p}\alpha$, $p = 8$-poles, $\alpha = \pi$.

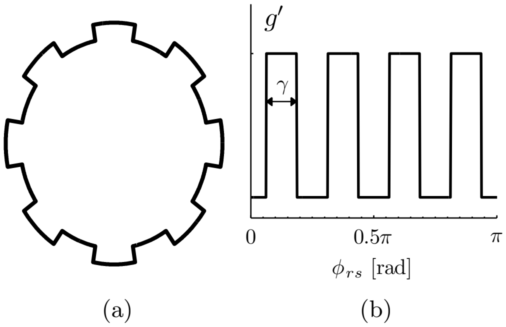

Figure 2.4: Effective airgap: (a) Cross-section, (b) Profile; $\gamma = \frac{2}{p}|\alpha - \pi|$, $p = 8$-poles, $\alpha = 1.5\pi$.

The inductance matrix confirms the non-saliency, as the phase winding inductances remain constant with respect to the rotor position ($L_g = 0$):

$$\begin{aligned} L_0 &= 2\pi\mu_0 h_1 r l \left(\frac{N_s}{p}\right)^2 \\ L_g &= 0 \\ L_{f0} &= \pi\mu_0 h_2 r l N_f \frac{Ns}{p} \\ L_f &= \pi\mu_0 h_1 r l N_f^2 \end{aligned}$$

2.3.2 Square airgap profile

The case of a square airgap profile is depicted in Fig. 2.3 and is specified in terms of a variable duty-cycle square wave:

$$g_u\left(\phi_{rs}\right) = \frac{1}{h_1 + h_2\,\mathrm{SQ}_\alpha\left(\frac{p}{2}\phi_{rs}\right)} \tag{2.16}$$

$$g_l\left(\phi_{rs}\right) = \frac{1}{h_1 + h_2\,\mathrm{SQ}_\alpha\left(\frac{p}{2}\phi_{rs} + \pi\right)} \tag{2.17}$$

where h_1 is defined by (2.13) and h_2 by (2.14). $\mathrm{SQ}_\alpha\left(\theta\right)$ can be expressed as a Fourier series:

$$\mathrm{SQ}_\beta\left(\theta\right) = 1 - \frac{\beta}{\pi} - \frac{4}{\pi}\sum_{n=1}^{\infty}\frac{1}{n}\sin\frac{n\beta}{2}\cos\left(n\theta + n\pi\right)$$

The effective airgap defined in (2.4) to calculate the phase inductances is given below:

$$g'\left(\phi_{rs}\right) = \frac{1}{g_1 + g_2\,\mathrm{SQ}_{2|\alpha-\pi|}(p\phi_{rs})} \tag{2.18}$$

where g_1 and g_2 depend on the value of α:

$$g_1 = \begin{cases} k_g\left(3g_{\max} + g_{\min}\right) & \text{if } \alpha \le \pi, \\ k_g\left(3g_{\min} + g_{\max}\right) & \text{if } \alpha \ge \pi. \end{cases}$$

$$g_2 = \begin{cases} k_g\left(g_{\min} - g_{\max}\right) & \text{if } \alpha \le \pi, \\ k_g\left(g_{\max} - g_{\min}\right) & \text{if } \alpha \ge \pi. \end{cases}$$

and $k_g = \left(2g_{\max}\,g_{\min}\right)^{-1}$.

The terms of the inductance matrix are evaluated as:

$$L_0 = 2\mu_0 rl\left(\pi h_1 + h_2\left[\pi - \alpha\right]\right)\left(\frac{Ns}{p}\right)^2$$

$$L_g = -2\mu_0 h_2 rl\left(\frac{N_s}{p}\right)^2\sin\alpha$$

$$L_{f0} = 4\mu_0 h_2 rlN_f\left(\frac{N_s}{p}\right)\sin\frac{\alpha}{2}$$

$$L_f = \mu_0 rl\left(\pi h_1 + h_2\left[\pi - \alpha\right]\right)N_f^2$$

Notice that when $\alpha = \pi$, (2.18) reduces to (2.15), L_g becomes 0, and the reluctance torque term in (2.10) vanishes. Therefore, $\alpha = \pi$ corresponds to a non-salient rotor

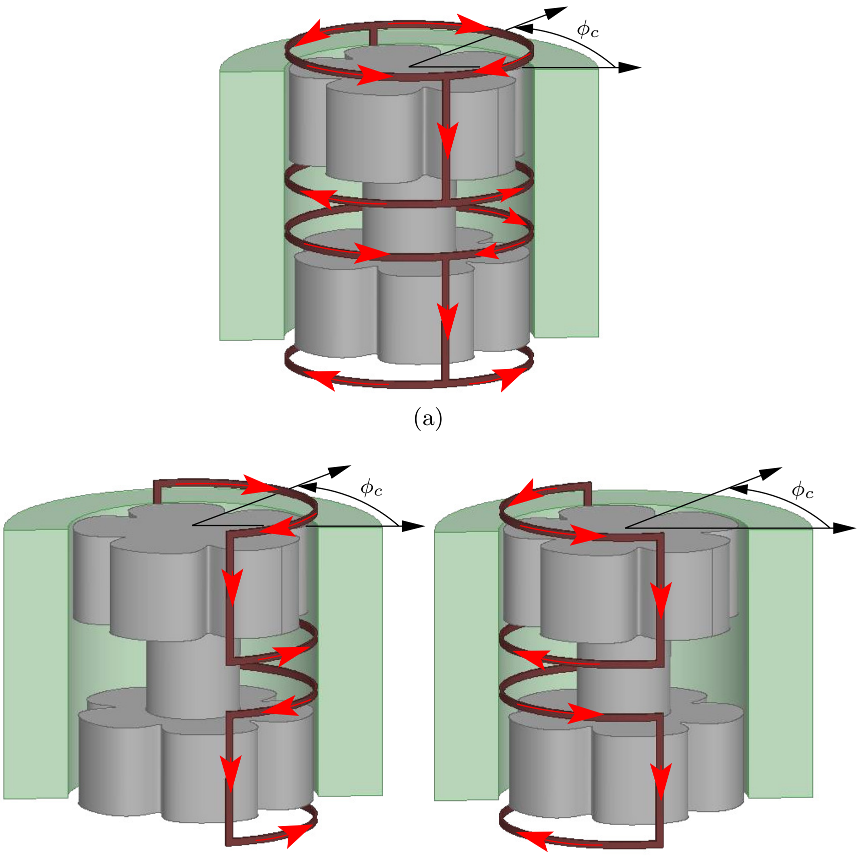

(a)

(b)

(c)

Figure 2.5: Top and bottom suspension winding configurations on a $p = 10$ pole sinusoidal rotor: (a) config. 1, (b) config. 2, (c) config. 3.

structure. As previously suggested, to understand the effect of saliency, this motor can be considered as the superposition of two motors: a synchronous reluctance motor with an airgap profile given by (2.18) and a cylindrical wound-rotor synchronous generator. The airgap of such a synchronous reluctance motor is shown in Fig. 2.4 for the same g_{min} and g_{max} as the rotor depicted in Fig. 2.3. Notice that the axial length of this equivalent motor is l, whereas the actual motor consists of two segments each with an axial length l.

2.4 Suspension winding configurations

Unlike the torque winding, the choice of end-turn configuration of each phase of the suspension winding has implications for the machine operation. The reason for this is that one of the end-turn sections is located in the middle of the axial length of the rotor, similar to the field winding, allowing for a circulating flux to flow axially from the bottom of the rotor to the top, cross the airgap radially, and return axially from the top of the stator to the bottom. The three choices of end-turn configuration are depicted for a single turn in Fig. (2.5). Note that configuration 1 corresponds to a double layer, full-pitch winding.

2.4.1 MMF calculations

The curl and divergence of the magnetic field can be imposed to solve for the MMF generated by a current flowing through N-turns of the suspension winding centered at an angle ϕ_c and spanning the ψ rotor section ($\psi = u$ for the upper rotor section, $\psi = l$ for the lower rotor section):

$$\begin{aligned} f_{p,h,\psi}\left(\phi_c, \phi_{ss}, \theta_{ms}\right) = \frac{NI}{2}\Big[&\frac{\mathrm{gh}_{\psi}\left(\phi_c, \theta_{ms}\right)}{\mathrm{gav}} + \mathcal{P}_h \\ &+ \mathrm{SQ}_{\pi}\left(\phi_c - \phi_{ss}\right)\Big] \end{aligned} \tag{2.19}$$

$$f_{s,h,\psi}\left(\phi_c, \phi_{ss}, \theta_{ms}\right) = \frac{NI}{2}\left[\frac{\mathrm{gh}_{\psi}\left(\phi_c, \theta_{ms}\right)}{\mathrm{gav}} + \mathcal{S}_h\right] \tag{2.20}$$

where the subscript p indicates that the MMF is acting on the rotor section that the suspension winding spans (specified by ψ), the subscript s indicates that the MMF is acting on the other rotor section, the subscript h denotes the style of the suspension winding (1, 2, or 3) as labeled in Fig. 2.5, it is assumed that $g_l\left(\phi_{rs}\right) = g_u\big(\phi_{rs} + \frac{2}{p}\pi\big)$, and:

$$\begin{aligned} \mathrm{gh}_{\psi}\left(\phi_c, \theta_{ms}\right) &= \int_{\phi_c + \frac{\pi}{2}}^{\phi_c + \frac{3\pi}{2}} \frac{1}{g_{\psi}\left(\phi_{ss} - \theta_{ms}\right)} \mathrm{d}\phi_{ss} \\ \mathrm{gav} &= \int_0^{2\pi} \frac{1}{g_u\left(\phi_{ss} - \theta_{ms}\right)} \mathrm{d}\phi_{ss} \\ &= \int_0^{2\pi} \frac{1}{g_l\left(\phi_{ss} - \theta_{ms}\right)} \mathrm{d}\phi_{ss} \end{aligned}$$

$$\mathcal{P}_h = \begin{cases} -\frac{1}{2} & \text{if } h = 1, \\ 0 & \text{if } h = 2, \\ -1 & \text{if } h = 3. \end{cases} \qquad \mathcal{S}_h = \begin{cases} -\frac{1}{2} & \text{if } h = 1, \\ -1 & \text{if } h = 2, \\ 0 & \text{if } h = 3. \end{cases}$$

Similar to the torque winding, the number of conductors at an angular location ϕ_{ss} of phase-j of the suspension winding spanning rotor section ψ, is defined by:

$$n_{j\psi}\left(\phi_{ss}\right) = \frac{N_{ss}}{2} \sin\left(\phi_{ss} - \delta_j\right)$$

The resultant MMF produced by this phase winding is obtained from superimposing the MMF generated by the conductors located at each angle where N is replaced by $n_{j\psi}\left(\phi_c + \frac{\pi}{2}\right)$ and I is replaced by the phase winding current $i_{j\psi}$. Since $n_{j\psi}\left(\phi_{ss}\right)$ is a continuous function, this is done in the form of an integral. Each of the two rotor structures considered in this chapter yield the same resultant MMFs:

$$\begin{aligned} \mathcal{F}_{p,j,h,\psi}\left(\phi_{ss}\right) &= \int_{\delta_j - \frac{\pi}{2}}^{\delta_j + \frac{\pi}{2}} f_{p,h,\psi}\left(\phi_c, \phi_{ss}, \theta_{ms}\right) \mathrm{d}\phi_c \\ &= \frac{N_{ss}}{2}\left[-\frac{\mathcal{K}_h}{2} + \cos\left(\phi_{ss} - \delta_j\right)\right] i_{j\psi} \qquad (2.21) \\ \mathcal{F}_{s,j,h,\psi}\left(\phi_{ss}\right) &= \int_{\delta_j - \frac{\pi}{2}}^{\delta_j + \frac{\pi}{2}} f_{s,h,\psi}\left(\phi_c, \phi_{ss}, \theta_{ms}\right) \mathrm{d}\phi_c \\ &= \frac{\mathcal{K}_h}{2} \frac{N_{ss}}{2} i_{j\psi} \qquad (2.22) \end{aligned}$$

where the subscript j indicates the phase winding, the remaining subscripts are as defined for (2.19) and (2.20), and

$$\mathcal{K}_h = \begin{cases} 0 & \text{if } h = 1, \\ -1 & \text{if } h = 2, \\ 1 & \text{if } h = 3. \end{cases} \qquad (2.23)$$

2.4.2 Flux linkage calculations

The flux linkage calculations also vary based on the style of suspension winding configuration. Taking note of Fig. 2.5, the flux linking a single turn centered at angle ϕ_{ss} for each configuration is given below.

$$\begin{aligned}
\Phi_{1,\psi}\left(\phi_{ss},\theta_{ms}\right) &= \frac{1}{2}\left[\Phi_{2,\psi}\left(\phi_{ss},\theta_{ms}\right)+\Phi_{3,\psi}\left(\phi_{ss},\theta_{ms}\right)\right] \\
\Phi_{2,\psi}\left(\phi_{ss},\theta_{ms}\right) &= \int_{\phi_{ss}-\frac{\pi}{2}}^{\phi_{ss}+\frac{\pi}{2}} B_{\psi}\left(\xi,\theta_{ms}\right) rl\,\mathrm{d}\xi \\
\Phi_{3,\psi}\left(\phi_{ss},\theta_{ms}\right) &= -\int_{\phi_{ss}+\frac{\pi}{2}}^{\phi_{ss}+\frac{3\pi}{2}} B_{\psi}\left(\xi,\theta_{ms}\right) rl\,\mathrm{d}\xi
\end{aligned}$$

where B_{ψ} is the flux density in the airgap of the rotor section specified by ψ. These expressions can then be used to obtain the flux linkage for a phase-j suspension winding of configuration h:

$$\lambda_{h,j,\psi}\left(\theta_{ms}\right) = \int_{\delta_j-\frac{\pi}{2}}^{\delta_j+\frac{\pi}{2}} n_{j\psi}(\phi_{ss}+\tfrac{\pi}{2})\,\Phi_{h,\psi}(\phi_{ss},\theta_{ms})\mathrm{d}\phi_{ss} \tag{2.24}$$

2.5 Complete machine inductance matrices

The inductance matrices related to the suspension winding are now calculated for each rotor structure to complete the inductance matrix model of the motor. These matrices include the self inductance of the suspension winding, the mutual inductances between the torque and suspension windings, and the mutual inductances between the field and suspension windings. To calculate these, (2.24) is evaluated when the magnetic field in the airgap is produced by each of the various windings and the result is divided by the current flowing in that winding. The system inductance matrices can be partitioned as shown below:

$$\begin{aligned}
\{\lambda_{abc}\} &= [L_{abc}]\{i_{abc}\}+[L_{mf}]\,i_f+[L_{mtxy,u}]\{i_{xyu}\} \\
&\quad+[L_{mtxy,l}]\{i_{xyl}\} && (2.25)\\
\{\lambda_{xyu}\} &= [L_{mtxy,u}]^{\mathrm{T}}\{i_{abc}\}+[L_{mfxy,u}]\,i_f \\
&\quad+[L_{sxy,u}]\{i_{xyu}\}+[L_{mxy,l}]\{i_{xyl}\} && (2.26)\\
\{\lambda_{xyl}\} &= [L_{mtxy,l}]^{\mathrm{T}}\{i_{abc}\}+[L_{mfxy,l}]\,i_f \\
&\quad+[L_{sxy,l}]\{i_{xyl}\}+[L_{mxy,u}]\{i_{xyu}\} && (2.27)\\
\lambda_f &= [L_{mf}]^{\mathrm{T}}\{i_{abc}\}+[L_{mfxy,u}]^{\mathrm{T}}\{i_{xyu}\} \\
&\quad+[L_{mfxy,l}]^{\mathrm{T}}\{i_{xy,l}\}+L_{f,f}\,i_f && (2.28)
\end{aligned}$$

where $[L_{abc}]$, $[L_{mf}]$, and $L_{f,f}$ were previously calculated in (2.6). For the two rotor structures considered in this chapter the remaining matrices take the following general forms:

$$
\begin{aligned}
[L_{mtxy,\psi}] &= \begin{bmatrix} L_{a,x,\psi} & L_{a,y,\psi} \\ L_{b,x,\psi} & L_{b,y,\psi} \\ L_{c,x,\psi} & L_{c,y,\psi} \end{bmatrix} \\
L_{j,k,\psi} &= \mathcal{K}_{h_{k\psi}} L_{ts,\psi} \cos\left(\tfrac{p}{2}\theta_{ms} - \delta_j\right) \\
[L_{mfxy,\psi}] &= L_{sf,\psi} \begin{bmatrix} \mathcal{K}_{x_\psi} \\ \mathcal{K}_{y_\psi} \end{bmatrix} \\
[L_{sxy,\psi}] &= L_{ss} \begin{bmatrix} 1 + \mathcal{K}_{h_{x\psi}}^2 & \mathcal{K}_{h_{x\psi}} \mathcal{K}_{h_{y\psi}} \\ \mathcal{K}_{h_{y\psi}} \mathcal{K}_{h_{x\psi}} & 1 + \mathcal{K}_{h_{y\psi}}^2 \end{bmatrix} \\
[L_{mxy,u}] &= -L_{ss} \begin{bmatrix} \mathcal{K}_{h_{xu}} \mathcal{K}_{h_{xl}} & \mathcal{K}_{h_{xu}} \mathcal{K}_{h_{yl}} \\ \mathcal{K}_{h_{yu}} \mathcal{K}_{h_{xl}} & \mathcal{K}_{h_{yu}} \mathcal{K}_{h_{yl}} \end{bmatrix} \\
[L_{mxy,l}] &= [L_{mxy,u}]^T
\end{aligned}
$$

where $\mathcal{K}_h$ is defined by (2.23) and $h_{k\psi}$ is the suspension winding configuration of phase k spanning rotor section ψ.

In certain situations it is desirable to have two different end-turn configurations for the same suspension phase. For example, if the upper x-phase and y-phase windings each consisted of two separate windings with different configurations and the corresponding terminal currents $i_{xu1}, i_{yu1}, i_{xu2}, i_{yu2}$, the following mutual inductance matrix must be defined:

$$
\begin{aligned}
\{\lambda_{xy,u1}\} &= ... + [L_{sxy,hu,12}]\,\{i_{xy,u2}\} \\
[L_{sxy,hu,12}] &= L_{ss} \begin{bmatrix} 1 + \mathcal{K}_{h_{xu1}} \mathcal{K}_{h_{xu2}} & \mathcal{K}_{h_{xu1}} \mathcal{K}_{h_{yu2}} \\ \mathcal{K}_{h_{yu1}} \mathcal{K}_{h_{xu2}} & 1 + \mathcal{K}_{h_{yu1}} \mathcal{K}_{h_{yu2}} \end{bmatrix} \\
[L_{sxy,hu,21}] &= [L_{sxy,hu,12}]^T
\end{aligned}
$$

2.5.1 Sinusoidal airgap profile

For the sinusoidally-shaped rotor airgap profile previously defined in (2.11), the inductance constants become:

$$\begin{aligned}
L_{ts,u} &= -\pi\mu_0 h_2 r l \frac{N_s}{p}\frac{N_{ss}}{2} \\
L_{ts,l} &= -L_{ts,u} \\
L_{sf,u} &= 2\pi\mu_0 h_1 r l \frac{N_f}{2}\frac{N_{ss}}{2} \\
L_{sf,l} &= -L_{sf,u} \\
L_{ss} &= \pi\mu_0 h_1 r l \left(\frac{N_{ss}}{2}\right)^2
\end{aligned}$$

2.5.2 Square airgap profile

For the square-shaped rotor airgap profile previously defined in (2.16), the inductance constants become:

$$\begin{aligned}
L_{ts,u} &= -4\mu_0 h_2 r l \frac{N_s}{p}\frac{N_{ss}}{2}\sin\tfrac{\alpha}{2} \\
L_{ts,l} &= -L_{ts,u} \\
L_{sf,u} &= 2\mu_0 r l \frac{N_f}{2}\frac{N_{ss}}{2}\left(\pi h_1 + h_2\left[\pi - \alpha\right]\right) \\
L_{sf,l} &= -L_{sf,u} \\
L_{ss} &= \mu_0 r l \left(\frac{N_{ss}}{2}\right)^2\left(\pi h_1 + h_2\left[\pi - \alpha\right]\right)
\end{aligned}$$

2.6 Analysis of suspension force production

Expressions for suspension forces produced by the bearingless ac homopolar motor are now developed for the two rotor structures and three suspension winding configurations.

Radial forces acting upon the rotor can be calculated from the Maxwell Stress Tensor:

$$F_{x,\psi} = \int_0^{2\pi} \frac{1}{2\mu_0} B_{g,\psi}\left(\phi_{ss}\right)^2 lr\cos\phi_{ss}\,\mathrm{d}\phi_{ss} \tag{2.29}$$

$$F_{y,\psi} = \int_0^{2\pi} \frac{1}{2\mu_0} B_{g,\psi}\left(\phi_{ss}\right)^2 lr\sin\phi_{ss}\,\mathrm{d}\phi_{ss} \tag{2.30}$$

where $B_{g,\psi}\left(\phi_{ss}\right)$ is the net or resultant flux density in the airgap of the ψ rotor section.

For both airgap profiles considered, it is found that as long as the bearingless ac homopolar motor has $p \geq 8$-poles, θ_{ms} does not appear in the resulting suspension force expressions, meaning that the suspension forces are independent of the rotor's angular position. When that is not the case, the bearingless ac homopolar motor lacks one of its primary features and therefore becomes difficult to justify as a bearingless motor. For this reason force expressions are only evaluated for the $p \geq 8$ case.

Evaluating (2.29) and (2.30) when the rotor is centered gives the following form for the force expressions:

$$F_{k,u} = \left(k_s\left[\tfrac{N_f}{2}i_f + \tfrac{N_{ss}}{4}C\left(i_{xy,ul}\right)\right] + k_d\, i_d\right) i_{ku} \tag{2.31}$$

$$F_{k,l} = -\left(k_s\left[\tfrac{N_f}{2}i_f + \tfrac{N_{ss}}{4}C\left(i_{xy,ul}\right)\right] + k_d\, i_d\right) i_{kl} \tag{2.32}$$

$$C\left(i_{xy,ul}\right) = \mathcal{K}_{h_{xl}} i_{xl} + \mathcal{K}_{h_{yl}} i_{yl} - \mathcal{K}_{h_{xu}} i_{xu} - \mathcal{K}_{h_{yu}} i_{yu}$$

where the subscript k indicates the direction of the force as well as the phase of the suspension winding, the constants k_s and k_d are dependent upon the rotor structure, $\mathcal{K}_h$ is defined by (2.23), and additional terms can be added to $C\left(i_{xy,ul}\right)$ if a phase of a suspension winding contains multiple configurations. It should be noted that if all suspension windings are of configuration 1, then $C\left(i_{xy,ul}\right) = 0$.

2.6.1 Sinusoidal airgap profile

For the sinusoidally shaped rotor structure defined by (2.11) and (2.12), the force constants become:

$$k_s = \pi\mu_0 \frac{N_{ss}}{2} rl\left(h_1^2 + \tfrac{1}{2}h_2^2\right)$$

$$k_d = \sqrt{\tfrac{3}{2}}\,\pi\mu_0 \frac{N_s}{p}\frac{N_{ss}}{2} rl h_1 h_2$$

2.6.2 Square airgap profile

For the square rotor structure defined by (2.16) and (2.17), the force constants become:

$$\begin{aligned} k_s &= \mu_0 \frac{N_{ss}}{2} rl \left[\pi \left(h_1^2 + h_2^2\right) + 2h_1 h_2 (\pi - \alpha)\right] \\ k_d &= 2\sqrt{6}\, \mu_0 \frac{N_s}{p} \frac{N_{ss}}{2} rl h_1 h_2 \sin \tfrac{\alpha}{2} \end{aligned}$$

2.7 Analysis of interference torque

Here, the analysis of section 2.3 is extended to include the effects of current in the suspension winding on the machine's torque. Analogous to section 2.6 revealing that the torque windings contribute to the suspension forces, this section shows that the suspension windings *interfere* with torque production. In most cases, this is not desirable, as any transients in the suspension winding current would then need to be compensated for by the torque controller. However in certain cases, such as when the rotor is horizontally oriented, a constant force may be desired and hence the torque interference from the suspension winding can be designed such that it is desirable.

Transforming the torque windings into the d-q representation described in section 2.3 results in the following expressions for d and q flux linkages:

$$\begin{aligned} \begin{Bmatrix} \lambda_d \\ \lambda_q \end{Bmatrix} &= \begin{bmatrix} L_d & 0 \\ 0 & L_q \end{bmatrix} \begin{Bmatrix} i_d \\ i_q \end{Bmatrix} + \begin{bmatrix} L'_{ts,xu} & L'_{ts,yu} \\ 0 & 0 \end{bmatrix} \begin{Bmatrix} i_{xu} \\ i_{yu} \end{Bmatrix} \\ &+ \begin{bmatrix} L'_{ts,xl} & L'_{ts,yl} \\ 0 & 0 \end{bmatrix} \begin{Bmatrix} i_{xl} \\ i_{yl} \end{Bmatrix} + \begin{bmatrix} L'_{mf} \\ 0 \end{bmatrix} i_f \end{aligned}$$

where $L'_{ts,h_{k\psi}} = \sqrt{3/2}\, \mathcal{K}_{h_{k\psi}} L_{ts}$. Using (2.9), an additional torque term appears in (2.10):

$$\tau_i = \frac{p}{2} i_q \left[L'_{ts,xu} i_{xu} + L'_{ts,yu} i_{yu} + L'_{ts,xl} i_{xl} + L'_{ts,yl} i_{yl}\right]$$

It is important to note here that since $\mathcal{K}_1 = 0$, suspension winding configuration 1 will result in no interference torque.

Chapter 3

Outer-Rotor AC Homopolar Motors for Flywheel Energy Storage

This chapter investigates the bearingless ac homopolar machine as a motor (no bearingless capability) for use in flywheel energy storage as an alternative to the permenant magnet (PM) motor. The primary objectives of using the ac homopolar motor is to decrease the flywheel system's idling losses, increase energy density, and decrease cost. Motor sizing equations, a comparison to the typically-used permanent magnet motor, and 3D finite element analysis of an example design are presented. It is shown that for high-performance flywheel designs, the ac homopolar motor can have a torque density comparable to that of a permanent magnet motor.[1]

3.1 Introduction

As described in Chapter 1, the traditional flywheel system design topology, which is non-integrated, is depicted in Fig. 3.1a. This dissertation proposes a fully integrated design based around an outer-rotor bearingless ac homopolar motor, depicted in Fig. 3.1b. Since most of the flywheel's energy is stored near its outer radius, removing the inner

---

[1] Portions of the material in this chapter have also been published in [51].

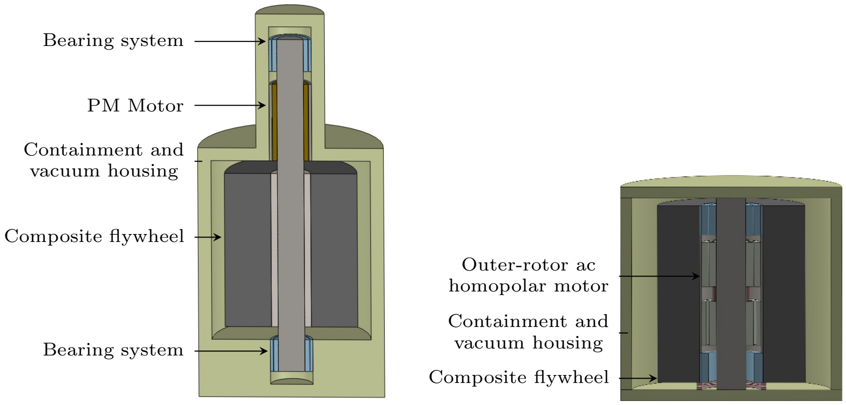

(a) Traditional flywheel design (b) Proposed design toplogy

Figure 3.1: The traditional and proposed flywheel design topologies

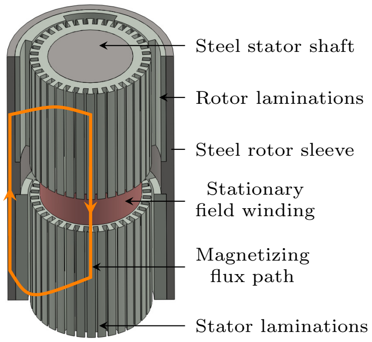

Figure 3.2: Outer-rotor ac homopolar motor

portion of the flywheel to make room for the motor does not significantly reduce the amount of energy stored but substantially reduces the volume as the electric machinery can now share the same space as the flywheel. This results in a substantially increased energy density. Compared to conventionally used PM motor, the ac homopolar motor yields lower core losses during energy transfer due to the inherently lower ac flux density and the variable excitation allows for the elimination of magnetic losses during times of idling or free-wheeling. Finally, by using current-based excitation, costly permanent magnets are avoided, reducing the electric motor cost.

3.2 Outer-rotor ac homopolar motor

The outer-rotor ac homopolar motor is shown in Fig. 3.2. It features variable excitation due to a field winding which is fixed to the stator. This means that no brushes or slip rings are required. This motor has been widely considered in the literature as an inner-rotor motor for use in superconducting and high-speed applications due to its current-based excitation and robust rotor structure, and as a high frequency generator due to its parallel arrangement of poles requiring no additional ampere-turns of field winding for an increased number of poles [27, 59, 65, 73–75].

The magnetizing flux path, depicted in Fig. 1c, is both radial and axial. The harmonics of the magnetizing flux density in the airgap can be controlled by the rotor shape, with the most common rotor shapes having an airgap length profile of a square wave and an inverted sine wave. Since the stator and rotor laminations have low magnetic permeability in the axial direction, a solid steel stator shaft and rotor sleeve are used to provide an axial flux path. The difference between the stator lamination inner diameter and outer diameter must be large enough to allow the flux to evenly distribute itself before reaching the stator shaft, or eddy currents may be induced in the steel. Several designs, such as [27, 65], have successfully used a solid rotor and, in some cases, a slot-less stator.

The machine only uses half of its magnetic circuit at any location, meaning that magnetizing flux density is always north-facing in one of the two stator/rotor sections and always south-facing in the other stator/rotor section. In this chapter, the two stator/rotor sections are referred to as the “top” section and the “bottom” section. The homopolar and fundamental magnetizing airgap flux density in the top and bottom rotor/stator segments can be described by (3.1). Using only one-half of the magnetic circuit at any location decreases both the torque density and the core losses significantly as compared to a traditional radial flux machine. This is considered in more detail later in the chapter.

$$\begin{aligned} B_{f,\text{top}}(\alpha) &= \hat{B}_{f1}\cos p\alpha + B_{f0} \\ B_{f,\text{bot}}(\alpha) &= \hat{B}_{f1}\cos p\alpha - B_{f0} \end{aligned} \tag{3.1}$$

3.3 Comparison to the PM motor

3.3.1 Torque density

The torque produced by classical radial flux machines is often written as a function of the rotor volume (or stator volume in the case of an outer-rotor motor) and tangential stress. The same is done here for the ac homopolar motor to allow for easy comparison. A peak linear current density of $\hat{A}$ is assumed, resulting in a circumferential current density defined by (3.2),

$$A(\alpha) = r_g \hat{A} \sin p\alpha \tag{3.2}$$

where p is the number of pole pairs, the average tangential stress can be found by dividing the torque τ produced by the airgap radius r_g and again by the active airgap area, which results in (3.3).

$$\begin{aligned} \langle \sigma_{f,tan} \rangle &= \frac{\tau}{r_g} \frac{1}{4\pi r_g L_s} \\ &= \frac{L_s \int_0^{2\pi} \left[B_{f,\mathrm{top}}(\alpha) + B_{f,\mathrm{bot}}(\alpha) \right] A(\alpha) \, \mathrm{d}\alpha}{4\pi r_g L_s} \\ &= \frac{\hat{B}_{f1} \hat{A}}{2} \end{aligned} \tag{3.3}$$

The torque can then be expressed as a function of the total active stator volume V_s, resulting in (3.4).

$$\tau = 2V_s \langle \sigma_{f,\mathrm{tan}} \rangle \tag{3.4}$$

Equations (3.3) and (3.4), which are the same expressions used for radial flux machines [76], allow the following comparison to a PM motor:

- In a PM motor there is no homopolar magnetizing flux ($B_{f0} = 0$), and therefore, neglecting harmonics, the peak airgap flux density corresponds to $\hat{B}_{f1}$. In the ac homopolar motor, $\hat{B}_{f1}$ is, at the most, one-half of the peak airgap flux density. This means that the ac homopolar motor results in less than one-half of the torque density of an equivalently dimensioned and magnetized PM motor.

- The active volume of the stator V_s of the ac homopolar motor does not include the region that the field winding spans. This further lowers the comparable torque density of the ac homopolar motor.

- In a PM motor, (3.4) scales linearly with active length because the only dependence on length is in V_s. In the ac homopolar motor, increasing the active length while maintaining all other parameters increases the magnetizing flux crossing the airgap, which means that the cross-sectional area of the stator shaft and rotor sleeve must also increase.
- In a PM motor, $\hat{A}$ must be limited to avoid demagnetizing the magnets. No such limitation exists with the ac homopolar motor.

3.3.2 Motor losses

In a flywheel system design, the amount of core loss is a critical design parameter. Any comparison of merit between two different types of motors should be based around a point of equal magnetic loss. As a simple analysis, consider the well-known Steinmetz loss equation for iron losses in the presence of a sinusoidaly varying flux density (3.5). This equation can be fit to steel manufacturer's loss data with reasonable accuracy, typically resulting in β values near 2. Note that $\hat{B}_{\mathrm{ac}}$ is the amplitude of the ac flux density (removing any dc bias) and f is its frequency.

$$P = K f^{\alpha} \hat{B}_{\mathrm{ac}}^{\beta} \tag{3.5}$$

From (3.5), it can be seen that for a PM motor to have the same iron losses as the ac homopolar motor, its peak airgap flux density must be reduced to the corresponding $\hat{B}_{f1}$ of the ac homopolar motor's flux density. Referring to (3.3), this will decrease the PM motor's torque density to a value near that of the ac homopolar motor–with the only difference caused by the volume occupied by the ac homopolar motor's field winding.

During times of idling, when no torque is being produced, the PM motor will continue to incur nearly the same iron losses as when torque is being produced. This is because the field excitation $\hat{B}_{f1}$ from the permanent magnets remains constant. In contrast, the ac homopolar motor's excitation is provided by a field winding current. This means that during times when no torque is produced, the field current can be removed, thereby eliminating all iron losses. However, when torque is being produced, the field winding current will lead to additional ohmic losses. Depending on the design, these ohmic losses may be compensated for by being able to adjust the excitation to the most efficient point–i.e. decreasing the excitation with increasing rotor speed.

3.4 Machine sizing equations for flywheel energy storage

The integrated flywheel and rotor can be viewed as two concentric hollow rotating cylinders where the inner hollow cylinder is the ac homopolar rotor and the outer hollow cylinder is the flywheel. The ac homopolar rotor can be dimensioned according the motor design requirements with a maximum tip speed $v_{sl,\text{tip}}$ limiting the outer-diameter of the rotor sleeve. The flywheel dimensions are determined by the required storage capacity, rotational speed, and outer diameter of the homopolar rotor.

Simplistic design equations follow, with relevant dimensions labeled in Fig. 3.3. These equations use the stored energy and parameters based around losses as inputs and provide the module dimensions and power rating as outputs. This approach is appropriate for the application of long-term flywheel energy storage, where the storage capacity and power losses are more important than the power rating. These equations neglect leakage flux, of which this machine caries a considerable amount, and assume an infinetly permeable back-iron. An approximation of the machine size and design trade-off's can be obtained from these equations; however, a more precise design requires 3D FE modeling.

3.4.1 Flywheel sizing

The total amount of energy stored in the flywheel is approximated as that stored in a hollow rotating cylinder, $E = \frac{1}{2}I\omega^2$. To obtain the maximum energy density, the outer diameter is chosen to be the maximum that the flywheel's material can support (3.6) and the length is scaled to achieve the required storage capacity (3.7), where $v_{f,\text{tip}}$ is the flywheel material's maximum surface speed, ρ_f is the material's mass density, and $r_{sl,\text{out}}$ is the outer radius of the rotor sleeve.

$$r_{f,\text{out}} = v_{f,\text{tip}}/\omega \tag{3.6}$$

$$L_f = \frac{4E}{\pi\rho_f v_{f,\text{tip}}^2\left(r_{f,\text{out}}^2 - \frac{r_{sl,\text{out}}^4}{r_{f,\text{out}}^2}\right)} \tag{3.7}$$

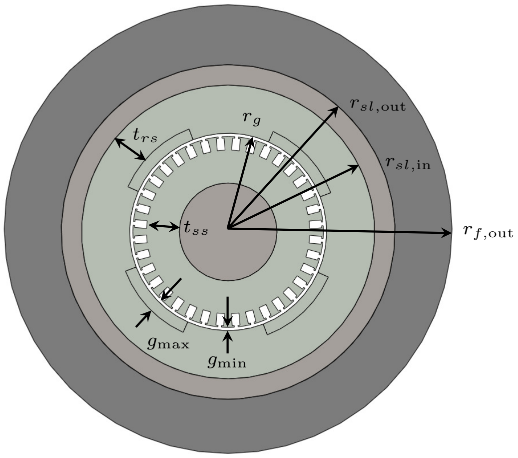

Figure 3.3: Cross-section of the integrated flywheel and ac homopolar motor.

The energy E in (3.7) must be increased if the module doesn't use the full speed range. Typical designs operate over half of their speed range as a compromise between usable energy and the torque requirement to provide constant power regardless of the state of charge.

3.4.2 AC homopolar motor sizing

The two stator/rotor segments of the ac homopolar motor can be dimensioned using (3.4) combined with a constraint based around the maximum tip speed of the rotor sleeve material and a constraint based around the magnetizing flux path: the magnetizing flux crossing the airgap is limited by the amount that the stator shaft and rotor sleeve can support. For mechanical and magnetic reasons, the following fixed lengths are assumed:

- t_{rs} between the rotor lamination notch and sleeve,
- t_{ss} between the stator teeth and the shaft,
- g_{min} minimum airgap length.

In addition to this, it is assumed that $\hat{B}_{f1}$ and $\hat{A}$ of (3.3) and maximum flux densities of the airgap B_{max}, stator shaft B_{sh}, and rotor sleeve B_{sl} are chosen based on loss and material saturation considerations. With these design choices, combined with the amount of energy to be stored in the flywheel, the following approach can be used to dimension the machine.

The homopolar flux density B_{f0} is calculated from $B_{\max}$ and $\hat{B}_{f1}$ for a square rotor in (3.8). The minimum airgap flux density (3.9), the required field winding ampere-turns (3.10), the axial length needed for the field winding (3.11), and the maximum airgap length (3.12) can then be calculated. Note that J_f is the field winding current density (including any packing factors) and $g'_{\min}$ and $g'_{\max}$ are effective airgap lengths.

$$B_{f0} = B_{\max} - \tfrac{2}{\pi}\hat{B}_{f1} \tag{3.8}$$

$$B_{\min} = 2B_{f0} - B_{\max} \tag{3.9}$$

$$z_Q i_f = \tfrac{2}{\mu_0} B_{\max} g'_{\min} \tag{3.10}$$

$$L_p = \frac{z_Q i_f}{t_{ss} J_f} \tag{3.11}$$

$$g'_{\max} = \frac{\mu_0 z_Q i_f}{2B_{\min}} \tag{3.12}$$

The stator slot depth d_s is determined by the peak linear current density $\hat{A}$, the winding layout, and the slot geometry. For example, a double layer winding featuring a rectangular slot with a tooth width w_t related to the slot width w_s by $w_t = kw_s$ would result in a slot depth as defined by (3.13). Here Q is the number of stator slots, N is the number of coils in series per phase, k_{w1} is the winding factor for the fundamental, and J_s is the slot current density (including any packing factors).

$$d_s = \frac{\hat{A} Q \left(1 + k\right)}{3N k_{w1} J_s} \tag{3.13}$$

The magnetizing flux passing through the stator shaft, airgap, and rotor sleeve must be equivalent, which can be used to express the following dimensions as a function of the airgap radius r_g: the axial length of each stator/rotor section (3.14), the inner radius of the rotor sleeve (3.15), and the outer radius of the rotor sleeve (3.16).

$$
\begin{aligned}
t_r &= -\tfrac{1}{2}g_{\min} + g_{\max} + t_{rs} \\
t_s &= \tfrac{1}{2}g_{\min} + d_s + t_{ss} \\
L_s &= \frac{(r_g - t_s)^2}{2r_g}\frac{B_{sh}}{B_{f0}} && (3.14) \\
r_{sl,\text{in}} &= r_g + t_R && (3.15) \\
r_{sl,\text{out}} &= \sqrt{\left(1+\tfrac{B_{sh}}{B_{sl}}\right) r_g^2 + 2\left(t_r - t_s\tfrac{B_{sh}}{B_{sl}}\right) r_g + t_r^2 + t_s^2\tfrac{B_{sh}}{B_{sl}}} && (3.16)
\end{aligned}
$$

Finally, the axial length of the machine is combined with the flywheel axial length L_f from (3.7), resulting in (3.17) where L_b is the axial length reserved for the bearing system. This equation can be solved for the airgap radius r_g which determines the remaining dimensions.

$$2L_s + L_p + L_b = L_f \tag{3.17}$$

For high speed designs, the outer radius of the motor sleeve is constrained by the material's maximum tip speed. This limits the amount of magnetizing flux the machine can contain, which reduces the maximum stator/rotor section length and therefore the torque density. In this case, the airgap radius can be solved directly from the outer radius of the rotor sleeve (3.18).

$$
\begin{aligned}
a &= 1 + \tfrac{B_{sh}}{B_{sl}} \\
b &= 2\left(t_r - t_s\tfrac{B_{sh}}{B_{sl}}\right) \\
c &= t_r^2 - r_{sl,\text{out}}^2 + t_s^2\tfrac{B_{sh}}{B_{sl}} \\
r_g &= \frac{-b}{2a} + \sqrt{\tfrac{b^2}{4a^2} - \tfrac{c}{a}} && (3.18)
\end{aligned}
$$

The resulting machine's torque capability can be estimated from (3.4). The power rating of the flywheel module is determined by the motor's rated torque at the lowest operational speed, as this is the largest power that can be maintained over the entire speed range.

Consider the design specifications in Table 3.1. In Fig. 3.4, the maximum rotational speed is varied while the usable energy is fixed at 10 kWh. The resulting estimated power

Table 3.1: Example flywheel design parameters

B_{sh}, B_{sl}	1.8 T, 1.8 T
$\hat{B}_{f1}$, $B_{\max}$	0.25 T, 0.4 T
$\hat{A}$	12 A/m
$g_{\min}$	1.25 mm
t_{rs}, t_{ss}	5.5 mm, 7.5 mm
J_f, J_s[a]	2.3 A/mm, 3.5 A/mm
Q, p	36 slots, 4 pole-pairs
k_{w1}, k	0.9452, 1.2
ρ_f[b]	1600 kg/m^3
$v_{f,\text{tip}}$, $v_{sl,\text{tip}}$	940 m/s, 200 m/s

---

[a] The current densities incorporate achievable packing factors.

[b] Typical data for carbon composite material is used for the flywheel.

and machine dimensions are shown, assuming that the flywheel module's operating speeds range from full to half. This is then repeated with the maximum rotational speed fixed at 24 kRPM and the usable energy varied. It is clear that in terms of power density, there is an optimal energy-stored and rotational-speed combination. If either the stored energy or rotational speed of this optimal point is exceeded, the maximum tip speed of the rotor sleeve limits the rotor's diameter and prevents the machine design from using the available axial length. When more power is desired, the PM motor has an advantage over the ac homopolar motor, since its axial length is independent of its rotor radius.

3.5 Example design

To validate the sizing equations, the design corresponding to the largest power density in Fig. 3.4 (24 kRPM, 10 kWh) was explored with 3D FE analysis. Magnetization data for an iron cobalt alloy was used for modeling the solid steel rotor sleeve and stator shaft [77] and a thin silicon steel was used for the rotor/stator laminations [78]. All simulations were solved in Infolytica MagNet software as 3D static nonlinear and used quarter symmetry. The model used is shown in Fig. 3.5a.

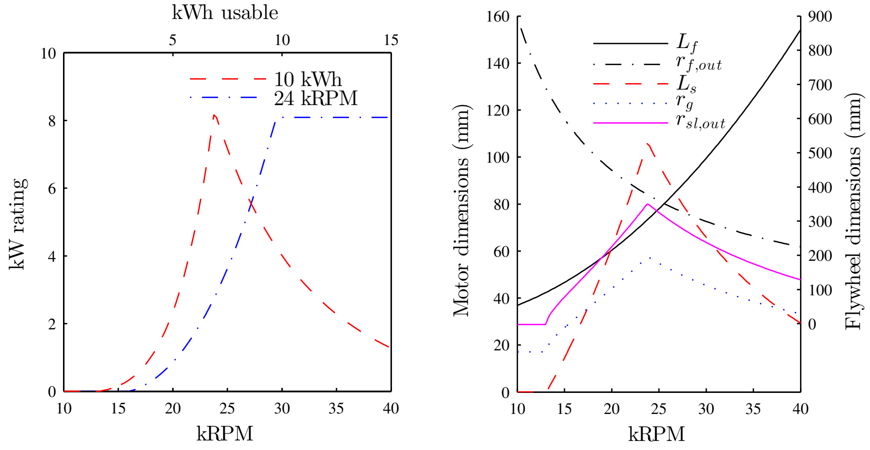

(a) Power rating

(b) Dimensions, $E = 10$ kWh

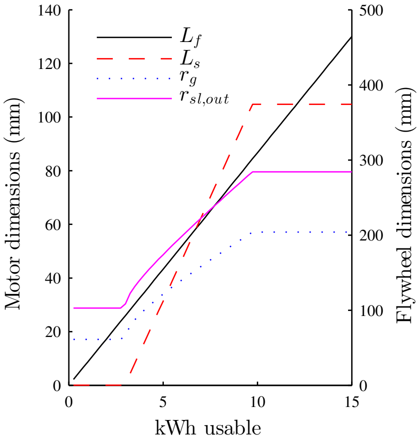

(c) Dimensions, 24 kRPM

Figure 3.4: The flywheel module power and dimensions estimated by the sizing equations for different maximum rotational speeds and amount of energy stored. All other parameters are specified in Table 3.1. Note that as the maxium operating speed changes, the energy density of the flywheel design remains nearly constant but the length-to-width ratio varies.

FE results under full-load and no-load are shown in Fig. 3.5. The excitation current had to be increased by 30% from that calculated by the sizing equations to obtain the required airgap flux density and the torque estimated by the sizing equations was approximately 1.2 Nm greater than that obtained through the FE results. This illustrates the inaccuracies of the sizing equations and the need for 3D FE analysis when designing the ac homopolar motor. In a future work, 3D transient nonlinear modeling will be conducted to analyze losses in the laminations and solid steel and to determine values for t_{ss} and t_{rs}.

3.6 Conclusion

The outer-rotor ac homopolar motor has been investigated for use in flywheel energy storage technology. It was shown that for low power designs, where magnetic losses are a key design parameter, the ac homopolar motor has a similar torque density to the typically-used PM motor. The PM motor has magnetic losses while idling but the ac homopolar motor does not. For these reasons, it is concluded that this motor is a promising machine for developing a flywheel system with long storage intervals.

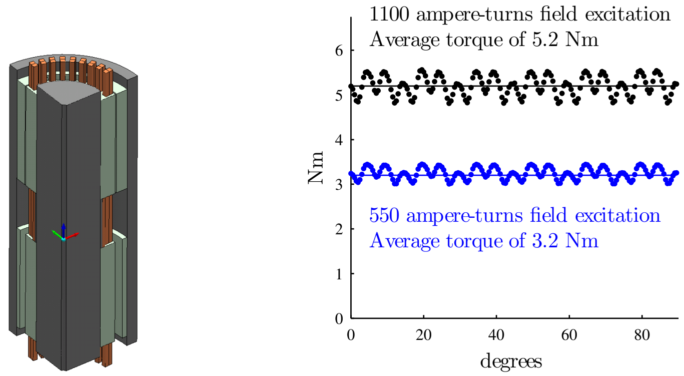

(a) FE Model (b) Torque waveform

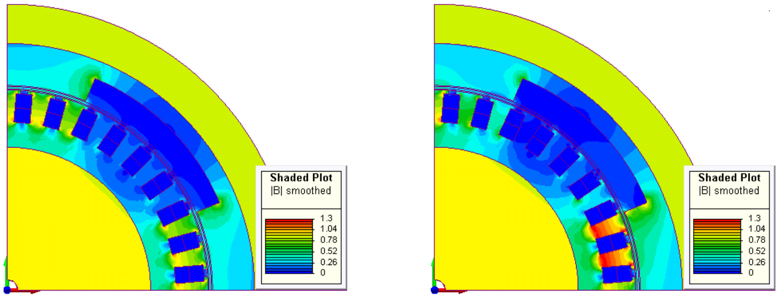

(c) No load (d) Full load

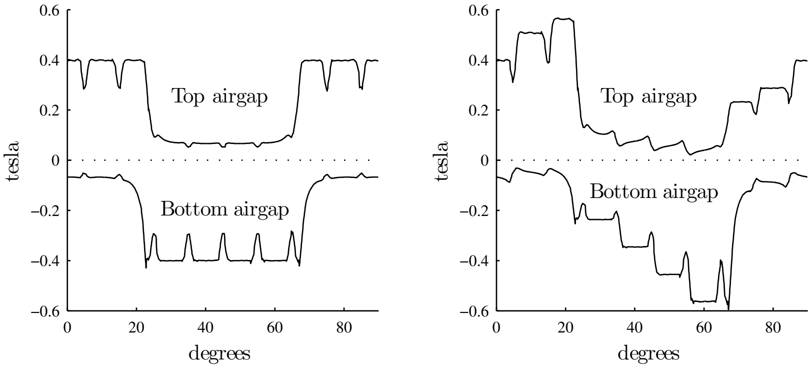

(e) No load airgap flux density (f) Full load airgap flux density

Figure 3.5: Results from 3D FE analysis of a 10kWh, 24 kRPM design; the full field excitation of 1100 ampere-turns is to be used at half-speed while 550 ampere-turns of field excitation is to be used at full-speed; (b), (c), (e), and (f) correspond to full field excitation and are evaluated at an axial location in the middle of each stator/rotor section.

Chapter 4

Magnetic Equivalent Circuit Modeling of the AC Homopolar Motor

This chapter develops a magnetic equivalent circuit model suitable to the design and optimization of the synchronous ac homopolar motor. This machine features both axial and radial magnetizing flux paths, which requires finite element analysis to be conducted in 3D. The computation time associated with 3D finite element modeling is highly prohibitive in the design process. The magnetic equivalent circuit model developed in this chapter is shown to be a viable alternative for calculating several design performance parameters and has a computation time which is orders of magnitude less than that of 3D finite element analysis. Results obtained from the developed model are shown to be in good agreement with finite element and experimental results for varying levels of saturation.[1]

---

[1] Portions of the material in this chapter have been submitted for publication in [48].

4.1 Introduction

The complex geometry and flux paths of the ac homopolar machine make the machine particularly difficult to design. The magnetizing flux flows in all three directions, requiring that finite element (FE) models be constructed in 3D. The computation time to evaluate 3D FE models is significant, making them impractical for use in optimizing the machine's design. Obtaining a less computationally expensive model of this machine for use in the design process has been the focus of several recent papers [31, 79–82]. These papers have used techniques including magnetic equivalent circuits (MEC), analytic modeling, and a 2D equivalent FE model and either fail to accurately model saturation, exhibit poor agreement with 3D FE results, are highly specific to a certain design's unique geometry, or take too long to solve. To the author's knowledge, there is not yet a sufficiently accurate model of the ac homopolar machine which is computationally efficient enough to be used in a design optimization.

The main contribution of this chapter is to develop a model of the ac homopolar machine which is both sufficiently accurate and has a short enough solve-time that it can be used in the design process. This model is based on MEC theory and is constructed in a manner which allows the designer to easily select a desired trade-off between accuracy and solve time. Simple, 1D flux tubes are used within a 3D magnetic circuit that includes both leakage flux paths and the effects of saturation. The geometry and path of each flux tube is presented. Symmetry is exploited based on the number of machine pole pairs and additional axial symmetry is used for evaluating the machine under no-load conditions. A mesh-based solution is used, as opposed to the conventional nodal-based solution, because it has been shown in [83, 84] that this solution exhibits better non-linear convergence and therefore reduces the computation time when portions of the model are saturated. Finally, both 3D FE and experimental results are used to validate the developed model. In Section 4.2, background information and literature on ac homopolar machine and MEC are presented; in Section 4.3, an overview of the MEC model as applied to the ac homopolar machine is presented; in Section 4.4, the geometry of each flux tube is defined; and in Section 4.5, results obtained from the MEC model are compared against FE and experimental results.

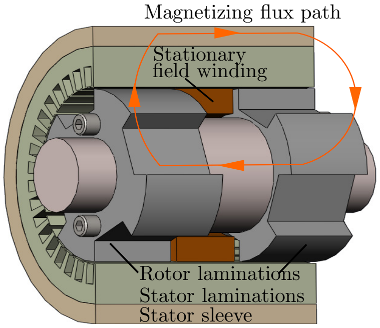

Figure 4.1: Synchronous ac homopolar machine geometry used for the MEC

4.2 Background

A diagram of the ac homopolar machine, as considered in this chapter, is shown in Fig. 4.1. As drawn here, the machine has two laminated rotor segments mounted on a magnetic shaft. A stationary field winding is mounted on the stator which encircles the rotor and causes a homopolar magnetizing flux to flow axially along the rotor shaft, radially through the rotor and stator laminations, and axially along a steel stator sleeve. The stator laminations can either be continuous, as drawn in Fig. 4.1, or they can be constructed as two separate stacks sandwiching the field winding.

Recent literature has proposed using MECs with 1D flux tubes in the design of various synchronous PM, induction, and wound-rotor machines as an alternative to 2D FE models [85–89]. It has been shown that this is an effective tool in population-based design processes, where the number of candidate designs can easily exceed 10^6 and even 2D FE models are too computationally expensive [85, 90]. The MEC model is usually solved using a nodal approach, similar to what is done in various electric circuit solvers; as previously mentioned, it has been shown in [83,84] that this solution approach can lead to convergence problems. In [91] an approach to model nonlinear magnetic materials was presented that guarantees convergence properties for mesh-based MEC solutions. While the convergence problems are eliminated with a mesh-based solution, a new problem arises due to the number of airgap flux tubes changing with rotor rotation (setting a flux tube permeance to zero results in an infinite reluctance); possible solutions to this include either using a fixed airgap mesh or the shaping algorithm defined in [84].

4.3 Overview of the MEC model

The model presented here is intended to be general enough to work for an ac homopolar machine with any combination of slots, poles, and phases. The circuit for the machine is divided into 2D “slices”, where each slice represents a cross-section. The slices are then connected via axial reluctances of the shaft, sleeve, and laminations. The circuit for a single slice is shown in Fig. 4.2a, which corresponds to an 8-pole, 12-slot machine. Here, quarter symmetry is used, so that only three stator teeth and one rotor tooth appear in the circuit. The connection of the slices to form the full 3D circuit is shown in Fig. 4.2b. Slices 3 and 4 correspond to the bottom rotor lamination stack, and have θ_m rotated by 180^{e} from the top rotor slices.

True mesh analysis only applies to planar circuits; the MEC for this model is not planar (note that the stator node in Fig. 4.2a is completely surrounded by branches) which means that it requires the more general loop analysis method. For the purposes of this chapter, this means only that certain reluctance branches will belong to three mesh fluxes, as opposed to two. The total number of required meshes is given by (4.1), where b is the number of flux tubes and n is the number of nodes.

$$N_m = b - n + 1 \tag{4.1}$$

The meshes for a slice are labeled in Fig. 4.2a with polarity defined in the clockwise direction. An additional mesh flux corresponding to the homopolar flux path must be defined between every two slices, labeled in Fig. 4.2b as ϕ_h. If these slices span the field winding, the mesh will experience the field winding’s ampere-turns as its MMF. It is important that the homopolar mesh use the same stator reluctances in each slice, so as to avoid encircling any of the stator slot current. For example, reluctances in ϕ_{h1} can be assigned as follows:

$$\begin{aligned}
\text{Path}_{\phi_{h1}} &= R_{arl1} + \text{Slice 1} - R_{asl1} - \text{Slice 2} \\
&= R_{arl1} + R_{ry,1} + R_{rt1,1} + R_{rg3,1} + R_{sg1,1} \\
&+ R_{st1,1} + R_{sby1,1} + R_{sbsl1,1} - R_{asl1} - R_{sbsl1,2} \\
&- R_{sby1,2} - R_{st1,2} - R_{sg1,2} - R_{rg3,2} - R_{rt1,2} \\
&- R_{ry,2}
\end{aligned} \tag{4.2}$$

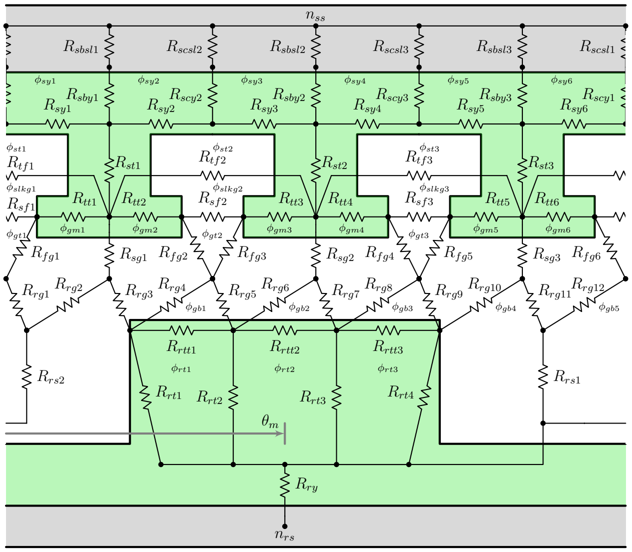

(a) MEC for a single slice

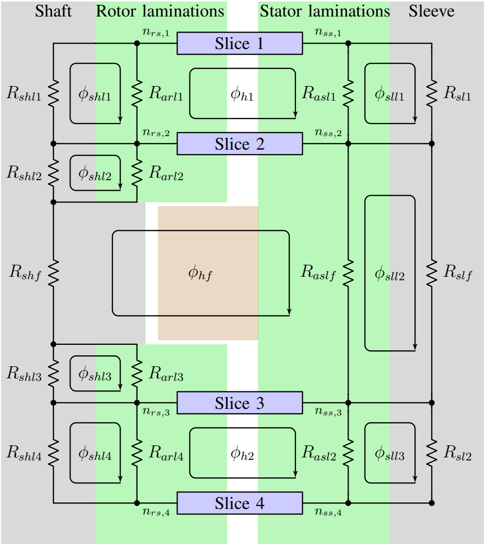

(b) Axial connection of the slices

Figure 4.2: MEC for an eight pole, 12 slot ac homopolar machine using quarter symmetry

Under no-load conditions, symmetry can be used so that the MEC only consists of the top slices. In this case, the acting ampere turns from the field winding is cut in half, the length of the flux tubes corresponding to R_{shf}, R_{aslf}, and R_{slf} is cut in half, and the homopolar mesh, which would have normally included a top and bottom slice, now only includes a single slice and is defined by (4.3).

$$\begin{aligned}\text{Path}_{\phi_{hf,\text{sym}}} &= R_{shf} + R_{arl2} + R_{ry,2} + R_{rt1,2} + R_{rg3,2} \\ &+ R_{sg1,2} + R_{st1,2} + R_{sby1,2} + R_{sbsl1,2} \\ &- R_{aslf} \qquad (4.3)\end{aligned}$$

All other aspects of the MEC remain the same. After solving, the mesh and branch fluxes in the bottom slices can be constructed from the solution for the top slices as $\phi_{\text{bot}} = -\phi_{\text{top}}$.

The system of equations is created by writing mesh loop current expressions for each mesh and solving the equations simultaneously. For example, the mesh equation for ϕ_{st1} of Fig. 4.2a is given by (4.4) where $\mathcal{F}_{st1} = NI_1$ is the MMF from the slot current in slot 1 at the instant of time the model is being solved. The only meshes which contain current and therefore an MMF source are those labeled as ϕ_{st} and $\phi_{h,f}$. The individual mesh equations are assembled into a non-linear system in matrix form, given by (4.5), where A_R is a square reluctance matrix of size N_m; ϕ and $\mathcal{F}$ are vectors of the mesh fluxes (which are the unknown variables) and MMFs (which are the known source terms), each of length N_m. The equations can be solved through well-established techniques for non-linear equations, such as the commonly used Newton-Raphson Method. A detailed description of the procedure for doing this and considerations which must be taken into account are presented in [83, 84].

$$\begin{aligned}\mathcal{F}_{st1} &= \left[R_{st3} + R_{sy6} + R_{sy1} + R_{st1} + R_{tf1}\right]\phi_{st1} \\ &\quad - R_{st1}\phi_{st2} - R_{st3}\phi_{st3} - R_{tf1}\phi_{slkg1} - R_{sy6}\phi_{sy6} - R_{sy1}\phi_{sy1} \qquad (4.4) \\ 0 &= A_R(\phi)\,\phi - \mathcal{F} \qquad (4.5)\end{aligned}$$

The designer is free to select the number of slices to be used based on the desired accuracy. The fewest number of slices possible is one, for the no-load symmetry case. For models with slot current present, an even number of slices must be used. Each slice contains $10Q - 1$ meshes, where Q is the number of stator slots in each slice's problem space (i.e. $Q = 3$ in Fig. 4.2a). Since the system of equations consists of as many equations as there are meshes, increasing the number of slices increases the required solve time.

Once the system of equations has been solved, the mesh fluxes are used to calculate the flux flowing through each flux tube of the MEC. The flux densities in various points of the machine can be calculated by dividing the flux flowing through a flux tube of interest by its cross-sectional area. This information can then be used to calculate magnetic losses. The flux linkage for each stator coil is calculated as the sum of the flux linking the coil in each slice, which [85] shows is the sum of the ϕ_{st} meshes that encircle a given coil. The model can be solved for different values of θ_m to construct a Fourier Series of the phase flux linkage, which can then be differentiated to obtain the phase back-EMF (4.7).

$$\lambda_u\left(\theta_m\right) = \lambda_0 + \sum_{v=1}^{\infty} \lambda_{u,v} \sin\left(v\theta_m + \phi_v\right) \tag{4.6}$$

$$\begin{aligned} V_u\left(t\right) &= \frac{d\lambda_u}{dt} \\ &= \frac{d\theta_m}{dt} \sum_{v=1}^{\infty} v\lambda_{u,v} \cos\left(v\theta_m + \phi_v\right) \end{aligned} \tag{4.7}$$

Torque can be calculated from the field energy in the airgap permeances [92]. When the machine winding does not contain subharmonics, enabling symmetry to be used to model a single pole-pair, the torque can be calculated from (4.8), where N_a is the number of R_{rg} flux tubes over all slices, θ_m is in electric radians, and p is the number of pole-pairs, and $P_{rg,i}$ is the permeance of the specified flux tube. Only airgap flux tubes corresponding to R_{rg} are considered in the torque expression because, as described later in Section 4.4.3, these are the only flux tubes which have permeance values that depend on rotor position. The partial derivative of these permeances can be calculated analytically and expressions are provided in Section 4.4.3.

$$T\left(\theta_m\right) = \frac{p}{2} \sum_{i=1}^{N_a} \mathcal{F}_{rg,i}^2 \frac{\partial P_{rg,i}}{\partial \theta_m} \tag{4.8}$$

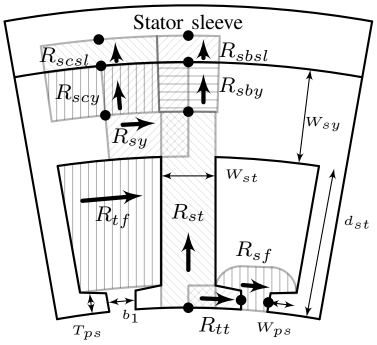

(a) Stator lamination and slot region

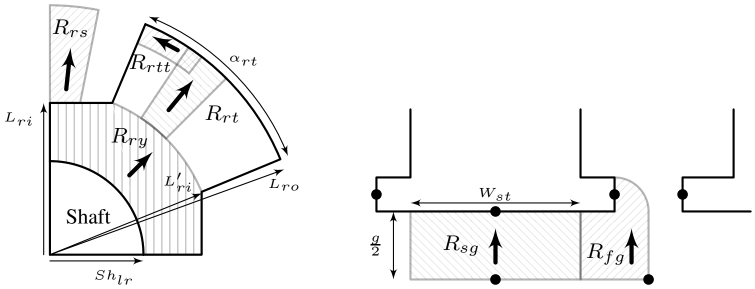

(b) Rotor lamination and slot region

(c) Stator airgap

Figure 4.3: Flux tubes in various parts of the MEC slice

4.4 Flux tube definitions

The shape of each of the flux tubes is now considered. While the flux tubes are defined with regards to the particular geometry this machine drawn in Fig. 4.1, they can easily be modified to account for different pole and tooth shapes.

4.4.1 Stator flux tubes

The stator lamination and slot flux tubes are defined in Fig. 4.3a where the nodes connecting the reluctances are labeled as black dots. The flux tubes are largely the same as what is described in [85], with two exceptions: first, pole shoes and their associated fringing fluxes are modeled (R_{tt} and R_{sf}); second, radial flux tubes are added to the stator yoke and sleeve (R_{sby}, R_{sbsl}, R_{scy}, R_{scsl}) for the homopolar flux.

Whenever the path length varies in a flux tube, such as in R_{sy} and R_{tf}, the mean path length is used. The length of the stator tooth flux tube R_{st} is assumed to extend half-way into the stator yoke; the length of the radial yoke flux tubes (R_{sby}, R_{scy}) is one-half of the yoke width; the length of the sleeve flux tubes (R_{sbsl}, R_{scsl}) is one-third of the sleeve width. The stator pole-shoe leakage reluctance R_{sf} is calculated from two separate permeances, a fringing permeance (4.9) and a direct permeance (4.10), where d is the axial depth of the slice.

$$\begin{aligned} P_{fr} &= \int_0^{W_{ps}} \frac{\mu_0 d}{b_1 + \pi r} \mathrm{d}r \\ &= \frac{\mu_0 d}{\pi} \ln\left(1 + \frac{\pi W_{ps}}{b_1}\right) \qquad (4.9) \end{aligned}$$

$$P_d = \frac{\mu_0 T_{ps} d}{b_1} \qquad (4.10)$$

4.4.2 Rotor flux tubes

The rotor lamination and slot flux tubes are defined in Fig. 4.3b. The rotor yoke is modeled very simply as a single flux tube because the flux density in this region is constant under steady state conditions and decomposing it into radial and tangential paths is not of interest. This flux tube is denoted as R_{ry} and is modeled with a path length of $L'_{ri} - Sh_{lr}$ and a cross-sectional area of $\alpha_m d \frac{L'_{ri} + Sh_{lr}}{2}$, where α_m is the angular span of the slice ($\alpha_m = \frac{\pi}{2}$ for Fig. 4.2a). The model uses $Q + 1$ radial tooth flux tubes and Q tangential tooth flux tubes with the geometry as shown. The tangential tooth flux tubes are intended to capture the flux density variation under load conditions due to slotting and localized saturation. These flux tubes are assumed to have a width equal to the airgap length. Radial leakage flux from the rotor slot to the airgap is modeled through $Q-1$ flux tubes (R_{rs}) which are assumed to have a cross-sectional area defined by (4.11) and a length defined by (4.12), where W_{rs} is the slot width and α_1 and α_2 are the angular locations of the two corners of the flux tube on the rotor slot edge with respect to the center of the slot. The fringing fluxes from the rotor tooth are taken into account through airgap flux tubes defined in Section 4.4.3.

$$A_{rsl} = \frac{W_{rs}}{Q-1} d \qquad (4.11)$$

$$\begin{aligned} L_{rsl} &= L_{ro} - \frac{l_r(\alpha_1) + l_r(\alpha_2)}{2} \qquad (4.12) \\ l_r(\alpha) &= \frac{L_{ri}}{\cos\alpha} \end{aligned}$$

4.4.3 Airgap flux tubes and rotor motion

To avoid the previously described issues pertaining to rotation, a uniform number of airgap flux tubes are used (regardless of the rotor position) which are connected to evenly spaced nodes in the center of the airgap, shown in Fig. 4.2a. The airgap nodes are centered in equal width regions which connect to stator flux tubes on the top and rotor flux tubes on the bottom. The number of airgap nodes is equal to twice the number of stator teeth so that the fringing fluxes from the stator pole shoes have a well defined path. The location of these airgap nodes does not change with rotor position, meaning that the flux tubes on the stator side of the rotor need only be calculated once. The geometry for the stator airgap flux tubes is shown in Fig. 4.3c; the reluctance value for R_{sg} is given by (4.13) and R_{fg} is calculated through two parallel permeances defined in (4.14) and (4.15).

$$R_{sg} = \frac{g/2}{\mu_0 W_{st} d} \tag{4.13}$$

$$\begin{aligned} R_{fg} &= \left(P_{fr} + P_d\right)^{-1} \\ P_{fr} &= \int_0^{T_{ps}} \frac{\mu_0 d}{g/2 + \frac{\pi}{2} r} \mathrm{d}r \\ &= \frac{2\mu_0 d}{\pi} \ln\left(1 + \frac{\pi T_{ps}}{g}\right) \end{aligned} \tag{4.14}$$

$$P_d = \frac{\mu_0 d W_{ps}}{g/2} \tag{4.15}$$

On the rotor side, an equal number of nodes are placed on the rotor at the interface to the airgap which are also assumed to reside in equal width regions. Based on the rotor's rotation (the value of θ_m), each rotor interface node is connected to the nearest two stationary airgap nodes via flux tubes. The permeance of the flux tubes is based on the overlap of the airgap and rotor interface regions. When the rotor node resides on an edge of the rotor tooth, fringing permeances are defined. Three cases which must be considered when calculating the permeances are depicted in Fig. 4.4. Note that cases 2 and 3 are depicted for when the rotor node is on the right edge of the rotor tooth; similar drawings can be made for when the rotor node is on the left edge. Calculations are now presented for the rotor airgap interface permeances and their derivatives, which are needed for use in the torque expression (4.8).

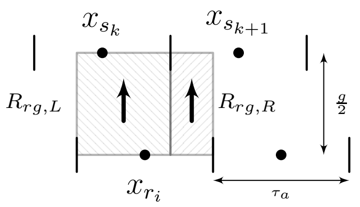

(a) Case 1: No fringing fluxes

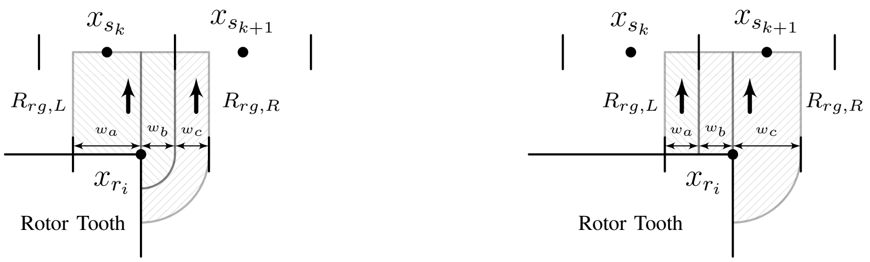

(b) Case 2: fringing fluxes in both reluctances (c) Case 3: fringing fluxes in only one reluctance

Figure 4.4: Rotor airgap interface flux tubes

Rotor airgap permeance case 1

These permeances are calculated as (4.16) and (4.17). The necessary derivatives can be calculated by differentiating these expressions with respect to x_{r_i} and multiplying by (4.19).

$$P_{rgL,1} = \mu_0 d \frac{\tau_a + x_{sk} - x_{r_i}}{g/2} \tag{4.16}$$

$$P_{rgR,1} = \mu_0 d \frac{\tau_a + x_{ri} - x_{s_{k+1}}}{g/2} \tag{4.17}$$

$$x_{r_i} = (i-1)k + \frac{L_{ro}}{p}\theta_m \tag{4.18}$$

$$\frac{dx_{r_i}}{d\theta_m} = \frac{L_{ro}}{p} \tag{4.19}$$

Rotor airgap permeance cases 2 and 3

The fringing permeances for cases 2 and 3 are calculated through integration in a manner similar to (4.9), but with the limits of integration based on the permeance channel width (w_a, w_b, w_c in Fig. 4.4). The results of these calculations are summarized in Table 4.1.

Table 4.1: Permeance calculations for rotor airgap[a]

	Case 2		Case 3	
	Left	Right	Left	Right
$x_{s_k} + \frac{\tau_a}{2}$[b]	$< x_{r_i}$	$> x_{r_i}$	$\geq x_{r_i}$	$\leq x_{r_i}$
$w_a = \tau_a +$	$-\frac{\tau_a}{2}$	$-\frac{\tau_a}{2}$	$x_{r_i} - x_{s_{k+1}}$	$x_{s_k} - x_{r_i}$
$w_b = \frac{\tau_a}{2} +$	$x_{r_i} - x_{s_{k+1}}$	$x_{s_k} - x_{r_i}$	$x_{s_k} - x_{r_i}$	$x_{r_i} - x_{s_{k+1}}$
$w_c = \tau_a +$	$x_{s_k} - x_{r_i}$	$x_{r_i} - x_{s_{k+1}}$	$-\frac{\tau_a}{2}$	$-\frac{\tau_a}{2}$
$\frac{dw_{abc}}{dx_{r_i}}$	0, 1, -1	0 -1, 1	1, -1, 0	-1, 1, 0
P_{rgL}	P_c	$P_a + P_b$	$P_b + P_c$	P_a
P_{rgR}	$P_a + P_b$	P_c	P_a	$P_b + P_c$
P_a	$\mu_0 \frac{w_a d}{g/2}$		$\mu_0 \frac{w_a d}{g/2}$	
P_b	$\frac{2\mu_0 d}{\pi} \ln\left(1 + \frac{\pi w_b}{g}\right)$		$\mu_0 \frac{w_b d}{g/2}$	
P_c	$\frac{2\mu_0 d}{\pi} \ln\left(1 + \frac{\pi w_c}{g + \pi w_b}\right)$		$\frac{2\mu_0 d}{\pi} \ln\left(1 + \frac{\pi w_c}{g}\right)$	
$\frac{\partial P_a}{\partial x_{r_i}}$	$\frac{\mu_0 d}{g/2} \frac{dw_a}{dx_{r_i}}$		$\frac{\mu_0 d}{g/2} \frac{dw_a}{dx_{r_i}}$	
$\frac{\partial P_b}{\partial x_{r_i}}$	$\frac{2\mu_0 d}{g + \pi w_b} \frac{dw_b}{dx_{r_i}}$		$\frac{\mu_0 d}{g/2} \frac{dw_b}{dx_{r_i}}$	
$\frac{\partial P_c}{\partial x_{r_i}}$	$\frac{2\mu_0 d}{g + \pi w_b + \pi w_c} \left[\frac{dw_c}{dx_{r_i}} - \frac{\pi w_c}{g + \pi w_b} \frac{dw_b}{dx_{r_i}}\right]$		$\frac{2\mu_0 d}{g + \pi w_c} \frac{dw_c}{dx_{r_i}}$	

---

[a] These expressions are used for flux tubes associated with node x_{r_i} when this node is on an edge of the rotor tooth. "Left" and "Right" columns are used based on if the node is on the left or right edge.

[b] Check this condition to determine whether Case 2 or Case 3 expressions apply

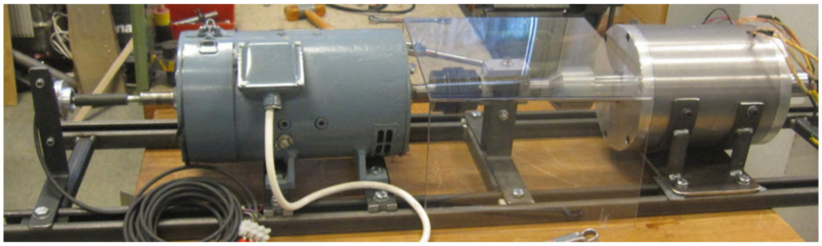

(a) Test stand

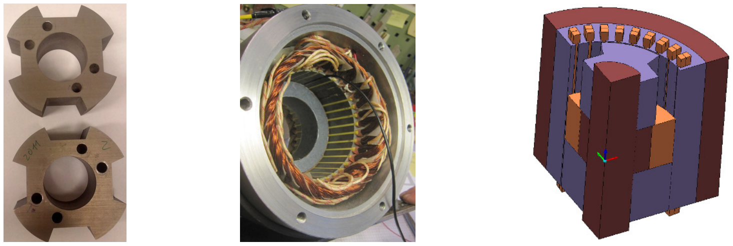

(b) Rotor laminations (c) Modified stator (d) FEA Model

Figure 4.5: (a) AC homopolar machine (right) connected to a dc motor (left) with an encoder (far left) and torque transducer (center) in the test stand; (b) the rotor laminations; (c) the modified stator with field winding installed; (d) the quarter-symmetry 3D FEA model used.

4.4.4 Axial flux tubes

The axial flux tubes that connect pairs of slices, shown in Fig. 4.2b, are assumed to have a length equal to the sum of half of each slice's thickness. The flux tubes for the shaft and sleeve (R_{shl}, R_{shf}, R_{sl}, R_{slf}) are cylindrical shapes and the dimensions are easily determined. The axial stator lamination flux tubes (R_{asl}, R_{aslf}) are in the shape of cylinder spanning the stator yoke (from the back of the stator slots to the start of the stator sleeve). The axial rotor lamination flux tubes (R_{shl}) are assumed to have a cross-sectional area equal to the entire rotor lamination cross-section.

The flux flowing through the axial lamination flux tubes encounters a large reluctance because it is flowing against the stacking direction and was initially ignored. However, in designs were the rotor shaft and stator sleeve are near saturating, significant homopolar flux flows axially in the laminated regions and is important to the machine's performance.

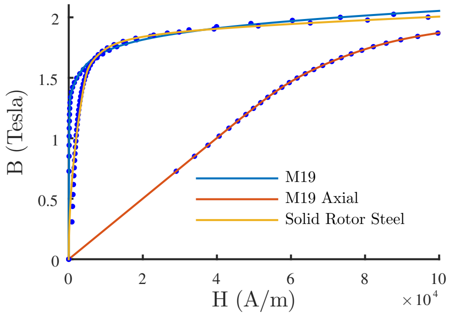

Figure 4.6: B-H curves used in the MEC and FEA models. The dotted points represent the data and the solid line is the fit. The M19 axial entry is the data used for axial lamination flux tubes.

4.5 Results

An ac homopolar machine has been constructed by modifying the stator of a commercially available induction machine. Pictures of the prototype can be seen in Fig. 4.5 and the machine parameters are described in Table 4.2. The MEC has been used to model this machine under various load and no load conditions. Quarter symmetry is used, so that the MEC consists of 9 slots and all no-load models make use of axial symmetry. The results are validated against FEA simulations conducted using Infolytica's MagNet software. The laminated steel was modeled using data provided in MagNet and a generic solid steel material model was used for the rotor shaft and stator sleeve. In the FEA models, the laminations are modeled as anistropic, with a reduced permeability in the axial direction based on the stacking factor. The BH curves used for FEA were fit to the anhysteretic permeability model presented in [91], shown in Fig. 4.6, for use in the MEC model.

Results from a no-load test and the measured torque profile are shown in Fig. 4.7. The MEC model was solved several times with differing numbers of slices to observe the trade-off between computational accuracy and effort. A single solve consistently required less than one second for up to 8 slices, while a single static solve of the 3D FEA model required approximately 2 minutes. Fig. 4.7a depicts the effect that the number of slices had on calculating the no load phase voltage for varying levels of saturation. There is a noticeable improvement when using 2 slices instead of 1 slice; much less improvement is observed when using 5 slices instead of 2 slices. The calculated voltage waveform

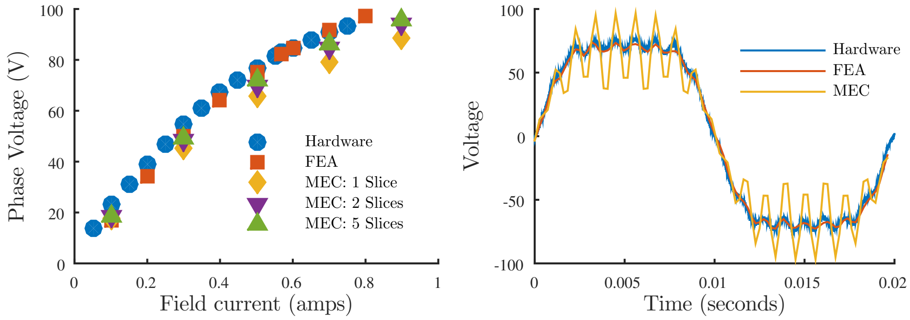

(a) Phase voltage magnitude (b) Phase voltage waveform

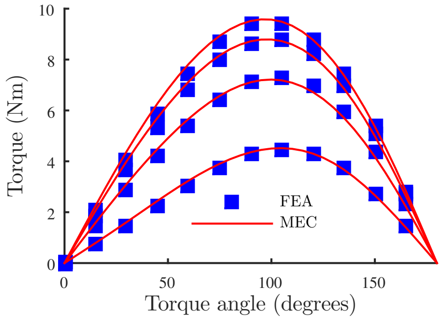

(c) Torque characteristic

Figure 4.7: Comparison of: (a) the fundamental component of the no load phase voltage at various field excitations; (b) the no load phase voltage waveform; (c) the torque profile. In (c), each line corresponds to a different field current: starting at 0.3A and increasing by 0.3A. All FEA was conducted on static models.

Table 4.2: AC homopolar prototype parameters

Field winding	2760 turns
Rated field winding current	0.57 A
Rated phase current	3.2 A (RMS)
Airgap min / max length	1 / 16.5 mm
Airgap radius	52 mm
Rated speed	750 RPM
Number of poles / slots	8 / 36
Coil span	4 slots
Laminations	24 Gauge M19

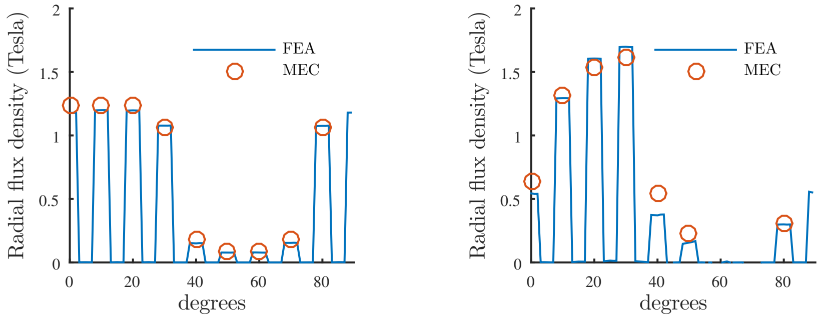

(a) No load (b) Rated load

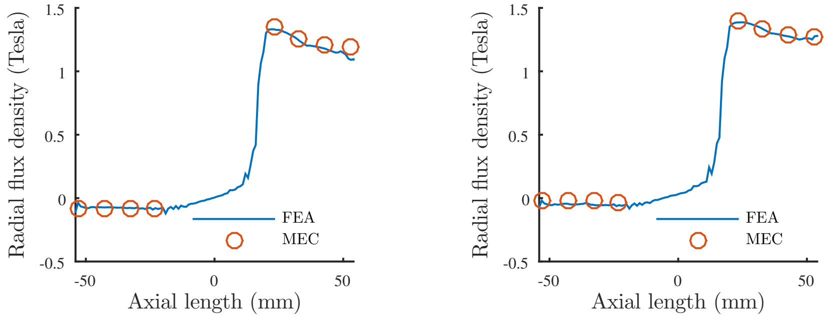

(c) No load (d) Rated load

Figure 4.8: Radial flux density in the stator teeth under rated field excitation and either no-load or rated load with a torque angle of 90°: (a), (b) in each tooth at an axial location matching the middle of the top rotor lamination stack, tooth 1 is at 10°; (c), (d) in tooth 1, each MEC data point is from a separate slice.

is shown in Fig. 4.7b where it is apparent that the MEC does a poor job of handling harmonic content. The torque angle profile calculations from both the FEA and MEC models are shown in Fig. 4.7c for a wide range of saturation levels. The MEC clearly exhibits good agreement with the FEA results. The MEC also accurately calculated the flux density in various locations of the machine. A comparison of calculations with static FEA for the stator teeth, yoke, and sleeve is shown in Fig. 4.8 and 4.9.

The machine performance is also affected by transient effects due to eddy currents in the solid steel of the rotor shaft and stator sleeve. Under steady-state operation, the rotor flux rotates at the same speed as the shaft and therefore induces no current in the shaft; however, the stator sleeve will experience a rotating flux and therefore eddy currents. These eddy currents present a greater reluctance to time varying flux, resulting in the following effects that are not modeled in the MEC or static FEA: 1) the homopolar flux will more evenly distribute itself in the stator yoke before entering the sleeve; 2) the armature reaction flux will be more constrained to the stator yoke. An example of the eddy currents and resulting field is depicted in Fig 4.10. Transient FE models were used to explore these effects and were constructed by setting the conductivity of the solid steel regions to 6.3×10^6 S/m (a typical value for low carbon steels), placing layers of 3rd order elements sized at one skin depth on the inner bore of the stator sleeve ("Eddy current region" in Fig. 4.10), and solving for 1.5 electrical periods (to allow initial "turn-on" transients to decay). Depending on the operating conditions, each model required 20 - 30 hours to solve. For the example design, transient models operated from 750RPM to 45,000 RPM yielded no significant differences from the static results presented in Fig. 4.7-4.9.

The calculated sleeve eddy current losses vary as a function of rotational speed and are shown in Fig. 4.11a. While the models that are under load exhibit more sleeve loss due to the armature reaction field, the sleeve losses remain insignificant compared to both the design's rated power and the iron losses in the laminated yoke. Next, the yoke thickness w_{sy} was decreased from 11.9mm to cause saturation in the yoke and force additional time varying flux into the sleeve, see Fig. 4.11b. Reducing the yoke thickness increases the tangential field (Fig. 4.11c), which is time varying, causing significant increases in the yoke iron losses before any observable increase in sleeve losses. Fig. 4.11c shows that the transient model always calculates the largest peak tangential

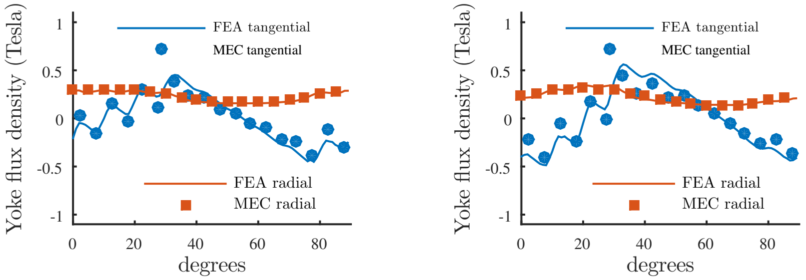

(a) No load

(b) Rated load, 90° torque angle

Figure 4.9: Flux density in the stator yoke under rated field excitation

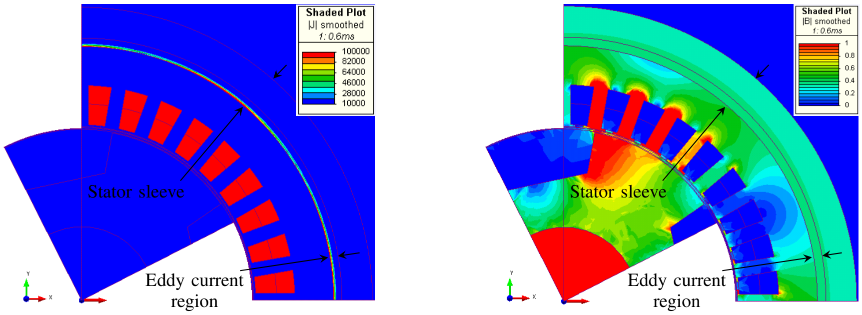

(a) Current density

(b) Flux density

Figure 4.10: Transient FEA model solved at rated current and 7500RPM.

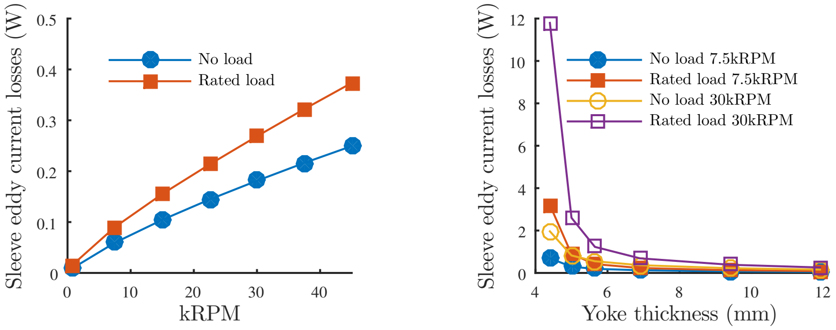

(a) Impact of rotational speed (b) Impact of yoke thickness

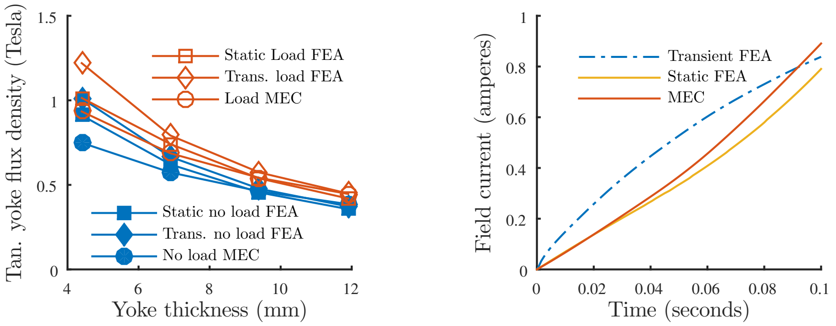

(c) Peak tangential yoke flux density (d) Transient field current

Figure 4.11: Comparison of (a), (b) calculated eddy current losses in the stator sleeve; (c) maximum tangential field in the stator yoke (averaged over one slot-tooth pitch), transient results: 30 kRPM; (d) calculated field current when a 200V dc supply is suddenly applied to the field winding.

field in the yoke, which is an expected consequence of the sleeve eddy currents. The static FEA and MEC models exhibit the same trends as the transient model and all three models are in good agreement for the more reasonable values of yoke thickness. This trend agreement combined with flywheel designs being highly sensitive to losses and lamination losses varying with small changes in yoke thickness mean that a design optimization utilizing the MEC would move away from the unreasonably thin yokes where Fig. 4.11c shows the static models to be inaccurate.

Finally, since the flux path of the field winding is through the solid steel regions, changes in the field winding current will induce eddy currents in both the stator sleeve and the rotor shaft. The machine is operated with a dc field current, meaning that this will only have an effect when the field winding is turned on or off–i.e. when the flywheel unit is transitioning into or out of idling mode. The current response to applying 200V for 100ms is shown in Fig. 4.11d. The static FEA and MEC models are used to calculate this current by transforming $V = RI + \dot{L}I + \dot{I}L$ into a difference equation using a backwards-difference approximation. The eddy currents cause the flux paths in the transient model to initially have a greater reluctance, reducing the inductance and allowing current to build up more rapidly. When the current exceeds 500mA, the flux paths in the static FEA and MEC models start to saturate, causing them to experience less inductance than the transient model and an accelerated increase in current. While this current response is the most notable discrepancy between the static and transient models, it is not typically an important design parameter of flywheel systems and can most likely be ignored in a design optimization.

4.6 Conclusion

AC homopolar machines have unique features which could be leveraged to design a long-term, low self-discharge flywheel energy storage module. However, a significant challenge in designing and optimizing the ac homopolar machine is the computation time required by 3D FEA models. This chapter has developed a general MEC model which can be solved in a fraction of the time required by 3D FEA models and has been shown to exhibit sufficient accuracy in key performance parameters, including: torque, no load voltage magnitude, and flux density (enabling loss calculations). It was shown that inacuracies due to static assumptions either do not matter for flywheel designs or only occur in unsuitable designs. The author envisions this MEC model being used in the design optimization process of ac homopolar machines, with a transient 3D FEA reserved for final design validation.

Chapter 5

Rigid Body Rotor Model Under Variable Excitation

One of the primary reasons that this dissertation is proposing the use of the bearingless ac homopolar motor for flywheel energy storage is the ease at which the machine can be operated under reduced excitation to minimize idling losses. This chapter investigates the impact of the excitation level on the magnetic bearing capabilities of the machine.[1]

5.1 Introduction

A complication arises in the radial force production when operating the bearingless ac homopolar motor under various excitation levels. The magnetic bearing position stiffness, which determines the unstable pole locations of the magnetic suspension system, and the bearing current stiffness are dependent upon the field excitation level. This means that a suspension controller proven to be stable for one level of field excitation may be unstable or perform unsatisfactorily for another level of field excitation. Since variable field excitation is an important ability of a bearingless ac homopolar machine applied to flywheel energy storage systems, it is necessary to have a suspension force model that can account for different excitation levels. The bearingless ac homopolar motor has been considered in [52, 56, 60, 62], none of which analyze this dependency. In

---

[1] Portions of the material in this chapter have also been published in [50].

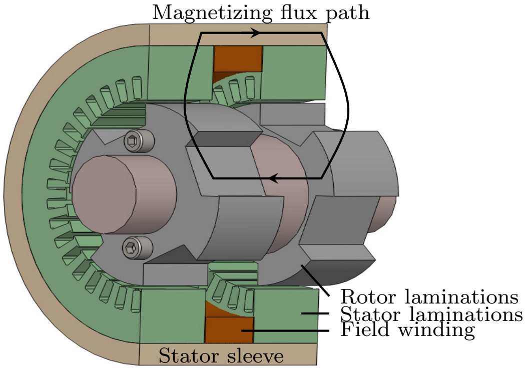

Figure 5.1: Bearingless ac homopolar machine with a square rotor.

this chapter, the classic, linearized suspension force model is modified by replacing the position and current stiffness constants with simple polynomial functions of the field current. These polynomials are fitted to 3D finite element simulation results where the field current has been varied over a wide range to include values where the machine's iron is largely unstaturated as well as moderately saturated.

The inner-rotor bearingless ac homopolar motor is considered, as depicted in Fig. 5.1, with two different rotor structures. First a rigid body suspension model is presented for the bearingless ac homopolar machine; next, the machine design and finite element simulation models are presented for two different rotor structures; finite element simulation models are used to investigate radial force dependence upon angular position and the cross-axis coupling for each rotor structure; finally, the finite element results are used to analyze the dependence of the suspension position stiffness and current stiffness on the field excitation, and the accuracy of modeling these quantities with simple polynomial functions of different degrees is evaluated.

5.2 Rigid body model

The classical linearized suspension force model of a magnetic bearing [93] is shown in (5.1), where k_s is the bearing position stiffness and k_f is the bearing current stiffness. For the bearingless ac homopolar machine this equation can be interpreted as describing the force produced along either the x or y axis upon one of the two rotor segments; δ is then the deviation from the center position along that axis; and i_s is the corresponding

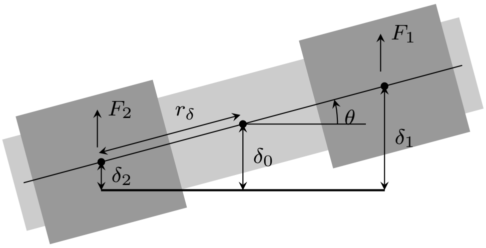

Figure 5.2: Diagram of the bearingless ac homopolar machine depicting the rigid body model notation.

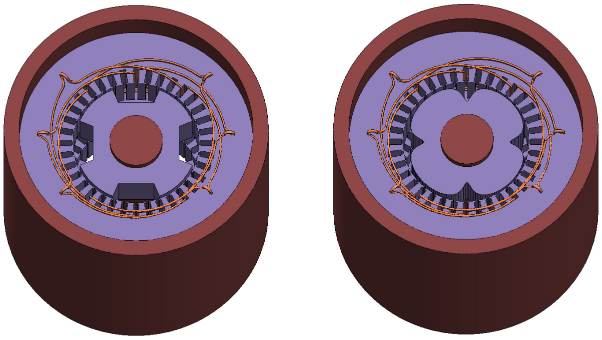

(a) Square rotor (b) Sinusoidal rotor

Figure 5.3: Models used for 3D finite element simulation.

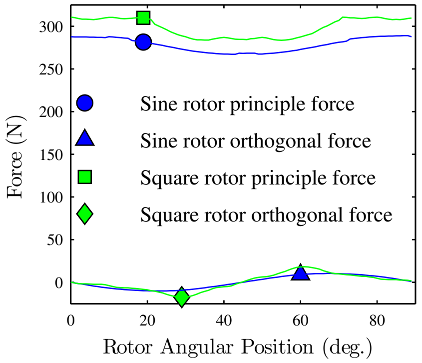

(a) Radial force profile

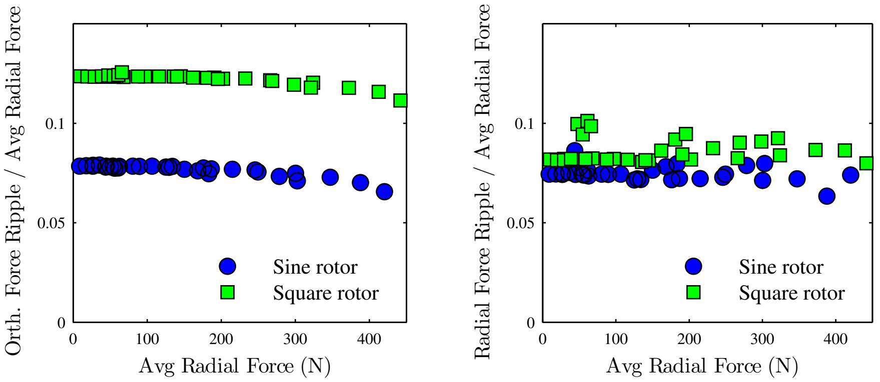

(b) Orthogonal direction force ripple (c) Principle direction force ripple

Figure 5.4: (a) Radial force values as a function of the rotor's angular position when $i_f = 2.33$A, and $i_s = 5$A; (b) normalized force ripple in the orthogonal direction; (c) normalized force ripple in the principle direction. In all cases, the rotor is centered; for (b) and (c), i_f is swept from 0.33A to 2.67A and i_s is swept from 1A to 7A.

suspension phase current.

$$F(\delta, i_s) = -\frac{k_s}{2}\delta + k_f i_s \tag{5.1}$$

While a high-speed flywheel rotor should be modeled as a flexible dynamic body, such a model adds complexity not necessary for the purposes of this chapter. Instead, it is quite illustrative to consider the rotor as a stationary rigid body. In this case, the x and y axes are decoupled. Referring to Fig. 5.2, the forces on each of the rotor segments are denoted as F_1 and F_2 which can be interpreted as either the x- or the y-axis forces and i_{s1} and i_{s2} are the corresponding suspension phase currents. The equation of motion can be applied and the results linearized to derive the following state-space representation with two states, δ_0 and θ [93]:

$$\begin{Bmatrix} \dot{\delta}_0 \\ \ddot{\delta}_0 \\ \dot{\theta} \\ \ddot{\theta} \end{Bmatrix} = \begin{bmatrix} 0 & 1 & 0 & 0 \\ -\frac{k_s}{m} & 0 & 0 & 0 \\ 0 & 0 & 0 & 1 \\ 0 & 0 & -\frac{r_\delta^2 k_s}{I} & 0 \end{bmatrix} \begin{Bmatrix} \delta_0 \\ \dot{\delta}_0 \\ \theta \\ \dot{\theta} \end{Bmatrix} + \begin{bmatrix} 0 & 0 \\ \frac{k_f}{m} & \frac{k_f}{m} \\ 0 & 0 \\ \frac{r_\delta k_f}{I} & -\frac{r_\delta k_f}{I} \end{bmatrix} \begin{Bmatrix} i_{s1} \\ i_{s2} \end{Bmatrix} \tag{5.2}$$

where m is the mass of the shaft, I is the moment of inertia of the shaft about the magnetic bearing axis (either the x- or y-axis). The characteristic polynomial[2] has unstable poles located at $\sqrt{\frac{|k_s|}{m}}$ and $\sqrt{\frac{r_\delta^2 |k_s|}{I}}$. The suspension controller must stabilize these poles in order to levitate the rotor.

5.3 Machine design

This chapter considers two different designs with the same stator but different rotors. Each rotor structure has the same minimum and maximum airgap length and in both cases backup bearings prevent the rotor from being displaced more than 1mm. The remaining machine design parameters are summarized in Table 5.1.

5.4 Finite element analysis

Infolytica's MagNet software was used for finite element modeling. Since the flux paths are both axial and radial, the analysis must be done in 3D. In addition to this, the suspension winding end-turns needed to be fully modeled as they reside between the two stator stacks. All results were taken with only the field winding and a single suspension winding phase excited (i.e. the x-direction phase) under static analysis. The rotor's angular position, the rotor's lateral displacement, the field winding's excitation,

---

[2] Note that for magnetic bearings k_s is always negative

Table 5.1: Machine design parameters

Field winding	1100 turns
Airgap minimum length	2 mm
Airgap maximum length	17.5 mm
Number of rotor poles	8
Stator slots	36
Suspension winding type	Double layer lap
Coils per suspension phase	6
Suspension coil pitch	18 slots

and the suspension winding's excitation were all varied. The models used for simulation are shown in Fig. 5.3. A single static solve typically used approximately 1.1 million elements and took approximately 13 minutes to solve on a PC with an Intel i7 3770 processor.

5.5 Force ripple and interference

While the bearingless ac homopolar machine is able to produce suspension forces largely independent of the rotor's angular position, there is still some unwanted dependency upon the angular position. This is depicted in Fig. 5.4 and is a result of harmonics in the suspension winding's MMF. The principle direction is defined as the desired force direction (i.e. the x direction when the x-phase winding is excited) and the orthogonal direction is defined as the direction orthogonal to the principle direction (i.e. the y direction when the x-phase winding is excited). The ripple in both the principle and orthogonal directions have a period of 90 degrees. For this reason, when a single data point is required for a force and the rotor's angular position is not of interest, the data point is taken as the average of the force over 90 degrees of rotor rotation. Notice that the sinusoidal rotor has less unwanted force ripple in both the principle and orthogonal directions. However, the square rotor is able to produce a greater force per ampere of suspension winding current.

5.6 Dependence on field excitation

To modify (5.1) to model multiple values of the field excitation, this chapter replaces ks and k_f with the polynomial functions indicated in (5.3) and (5.4). To do this, each polynomial is fitted to finite element results using the least squares method, as described below, and the results are displayed in Fig. 5.5. Here, Fig. 5.5a validates the linear approximation of δ for small displacements, Fig. 5.5b-d show the data points used to fit the polynomials, and Fig. 5.6a and 5.6b are used to validate the model.

$$k_s = \begin{cases} P_1(i_f) & = k_{s1} i_f \\ P_2(i_f) & = k_{s1} i_f + k_{s2} i_f^2 \\ P_3(i_f) & = k_{s1} i_f + k_{s2} i_f^2 + k_{s3} i_f^3 \end{cases} \tag{5.3}$$

$$k_f = \begin{cases} S_1(i_f) & = k_{f1} i_f \\ S_2(i_f) & = k_{f1} i_f + k_{f2} i_f^2 \\ S_3(i_f) & = k_{f1} i_f + k_{f2} i_f^2 + k_{f3} i_f^3 \end{cases} \tag{5.4}$$

To fit k_s, the simulations are run with $i_s = 0$A, $\delta = 0.1$mm, and the field current i_f is swept from a small value up to a current density of approximately 5A/mm^2, where portions of the machine's iron are moderately saturated. To fit k_f, the simulations are run with the rotor centered ($\delta = 0$mm), i_f is swept over the same range as for fitting k_s, and i_s is swept over a wide range.

5.7 Discussion

The quality of the polynomial fit can be evaluated by taking the error for each data point, normalizing this by the stiffness magnitude, and taking the average for each polynomial, as described by (5.5) and (5.6). In this expression, the subscript indicates whether the error is for the position or current stiffness and the superscript $*$ indicates the value predicted by the polynomial. The results are shown in Fig. 5.7 where it is clear that the third order polynomial gives the best fit for both the position and current stiffness. However, it is of note that only minor improvement in fit is gained from increasing the current stiffness polynomial from second to third order (2.1% to 0.2% for the sinusoidal rotor and 2.4% to 0.2% for the square rotor). For the position stiffness,

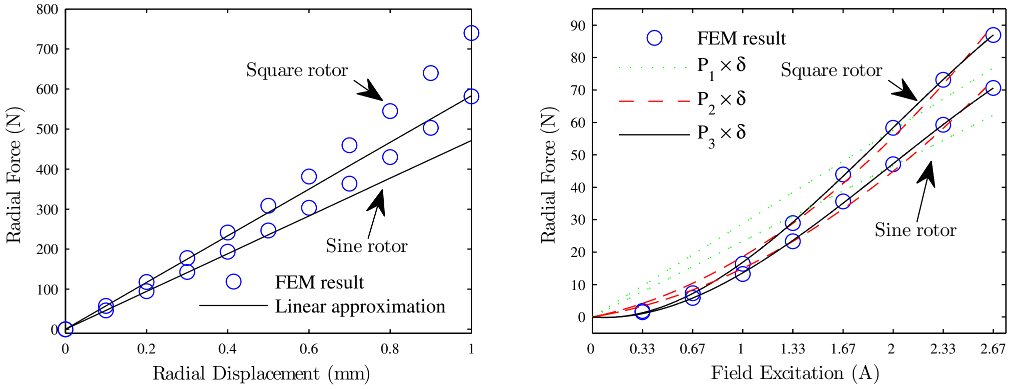

(a) $i_f = 2\text{A}$, $i_s = 0\text{A}$ (b) Data used to fit (5.3)

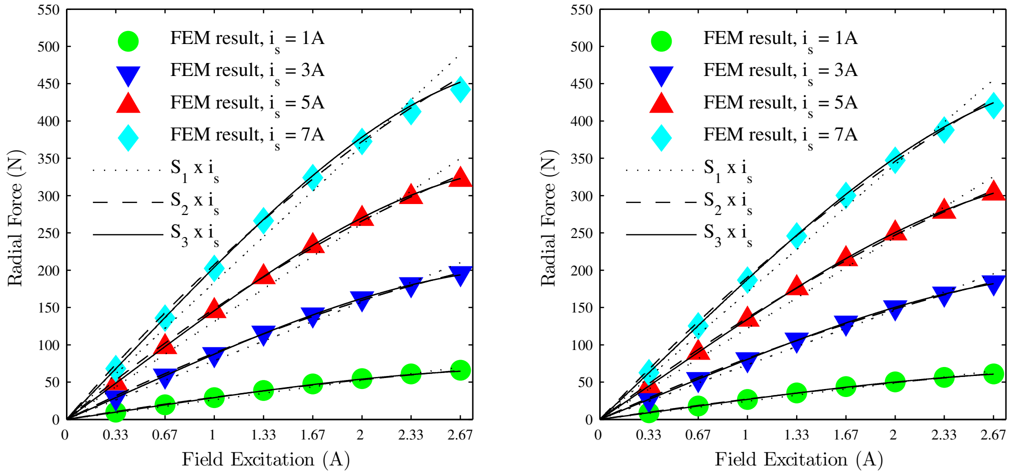

(c) Square rotor: data used to fit (5.4) (d) Sine rotor: data used to fit (5.4)

Figure 5.5: (a) Radial force versus δ, $i_f = 2\text{A}$ and $i_s = 0\text{A}$; (b) data points used to fit P_1-P_3, $\delta = 0.1\text{mm}$; (c) square rotor and (d) sinusoidal rotor datapoints used to fit S_1 - S_3, $\delta = 0\text{mm}$.

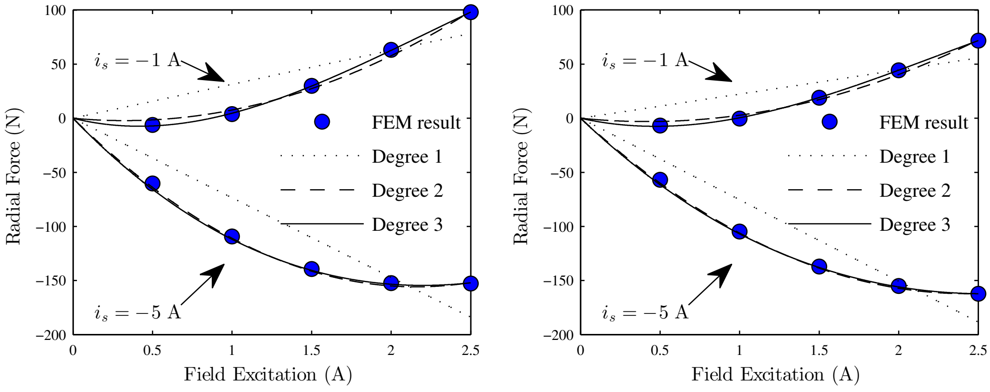

(a) Square rotor: $\delta = 0.2$mm (b) Sine rotor: $\delta = 0.2$mm

Figure 5.6: (a) square rotor and (b) sinusoidal rotor radial force validation of the fitted polynomials against finite element results, ‘Degree n’ indicates which P_n and S_n were used, $\delta = 0.2$mm.

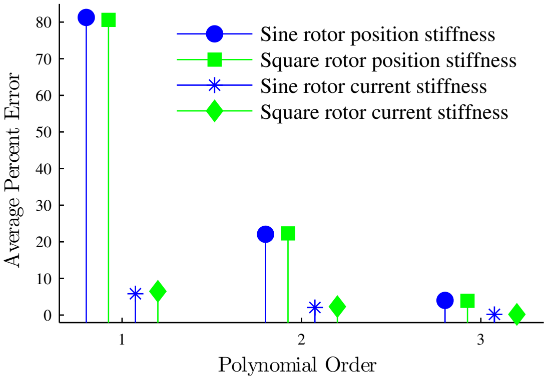

Figure 5.7: Average of the normalized fit error magnitude for the data points used for least squares fit in Fig. 5.5b-d of the polynomial functions (5.3) and (5.4).

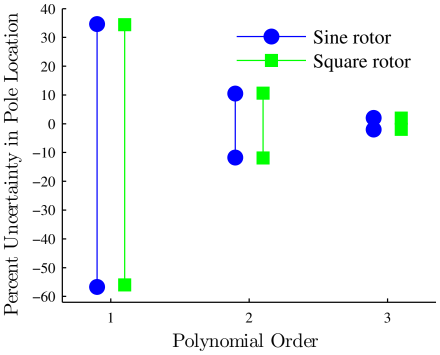

Figure 5.8: Uncertainty in suspension pole locations due to error in the position stiffness polynomial approximation.

this improvement is significant (22.1% to 4.0% for the sinusoidal rotor and 22.3% to 3.9% for the square rotor).

$$\epsilon_s = \left\langle \frac{|k_s^* - k_s|}{|k_s|} \right\rangle \tag{5.5}$$

$$\epsilon_f = \left\langle \frac{\left|k_f^* - k_f\right|}{|k_f|} \right\rangle \tag{5.6}$$

As shown in Section 5.2, the unstable poles' locations vary by the square root of the position stiffness. If the uncertainty in the position stiffness is taken as ϵ_s from (5.5), then the uncertainty in the predicted pole locations can be defined as (5.7). The results are depicted in Fig. 5.8, where it can be seen that the third order polynomial gives a very accurate estimation for the pole locations.

$$\begin{aligned} \epsilon_p &= \frac{P^* - P}{P} \\ &= \sqrt{1 \pm \epsilon_s} - 1 \end{aligned} \tag{5.7}$$

5.8 Conclusion

The classic, linearized magnetic bearing force equation has been revised to model the bearingless ac homopolar machine's suspension force under various excitation values. It has been found that the revised model accurately reflects the finite element simulations when the current stiffness is modeled with a second or third order polynomial function of the field current and the suspension stiffness is modeled with a third order polynomial function of the field current. All simulations and analysis have been conducted on a practical design of the bearingless ac homopolar machine which is currently being constructed.

The model presented in this chapter allows a control designer to accurately predict the field excitation's impact on the unstable suspension pole locations. The ability to do this is crucial to utilizing the bearingless ac homopolar machine in flywheel energy storage technology.

Chapter 6

Dual Purpose No Voltage Winding Design for Bearingless Motors

This chapter develops a winding design approach to create a single motor winding which is able to produce both radial force and torque. This approach can be used to design new bearingless motors as well as to transform conventional motor designs into bearingless motors by simply modifying the winding end-connections. The resulting winding has two sets of terminal connections: one for torque and one for suspension. The suspension terminals experience no motional-EMF when the rotor is centered, which means that the suspension drive can have a low voltage rating and that rotor vibrations can be passively dampened by simply short-circuiting the suspension terminals. Bearingless motors that use these so-called "dual purpose no voltage windings" can be designed to have higher torque density and lower losses associated with the magnetic suspension operation than traditional bearingless motors which utilize separate torque and suspension windings. It will be shown that many popular winding designs, including fractional-slot and concentrated windings, can be realized as dual purpose no voltage windings. The proposed approach applies to traditional $p \pm 1$ pole-pair bearingless motors as well as the bearingless consequent-pole and ac homopolar motors.[1]

---

[1] Portions of the material in this chapter have been submitted for publication in [46].

6.1 Introduction

Traditional bearingless motors are created by adding a $p \pm 1$ pole-pair suspension winding to a p pole-pair motor. Both windings are fed with currents at the synchronous frequency and the suspension current phase angle determines the force direction. This has been widely developed for both synchronous motors, such as permanent magnet and synchronous reluctance, and asynchronous motors [94–97]. More recently, the bearingless consequent pole [98] and ac homopolar motors [60], which this dissertation is primarily interested in, have been proposed which use a 2-pole suspension winding. These motors have decoupled magnetic bearing and torque functionality, enabling them to use a dc suspension current to produce a constant direction force regardless of the rotor's rotation as long as the rotor has at least 8-poles.

All of the aforementioned bearingless motors rely on separate torque and suspension windings which share the same slots. This creates a trade-off in slot space allocation that translates to a trade-off between radial force capability and torque density: whether the device is a "good" magnetic bearing or a "good" motor. The slot space must be allocated to the suspension winding based on the maximum force required. Many implementations of bearingless motors, such as those with vertical shafts, require relatively small suspension forces during normal operation and large forces during certain events, i.e. when accelerating through a critical speed. During normal operation, such machines effectively waste slot space which could otherwise carry torque current. Furthermore, to create radial forces, the suspension winding carries current to cancel torque winding current in certain slots, causing increased copper loss [99, 100]. For these reasons, there has been recent interest in combining the suspension and torque winding into a single winding [47, 99–111]. Such a winding is referred to as a "dual purpose" winding in this chapter. Efforts to create dual purpose windings have included:

1. various types of "split-windings" [100–104, 106–108], where the stator winding is divided into several separate windings located adjacent to one another so that the phase currents in each winding can be varied to adjust the airgap flux density at different locations;

2. a "middle-point-current-injection" design [110], where suspension currents are injected into certain coils in an otherwise-standard torque winding;

3. “no-voltage” designs based around a bridge [99, 105, 109] or a parallel winding structure [111]; the phrase “no-voltage” refers to the fact that the suspension terminals experience no motional-EMF when the rotor is centered.

In cases 1) and 2), the drive must overcome a motional-EMF to inject a suspension current. This requires a higher drive voltage to achieve satisfactory response times which can lead to significant increases in the inverter cost and losses [110, 111]. On the other hand, the terminal characteristics of the no-voltage winding approaches (case 3) are similar to that of the traditional separate winding approach in that the suspension terminals see no motional-EMF. This also means that the suspension terminals can be short-circuited to passively provide corrective forces when the rotor is rotating eccentrically [105], which can be an inexpensive way to dampen rotor vibrations in conventional machines with mechanical bearings. For these reasons, the case 3 windings, referred to as dual purpose no voltage (DPNV) windings, are seen to be at a significant advantage to the other types of dual purpose windings. DPNV technology is still relatively immature, with existing papers describing only specific example bearingless designs [99,105,109,111], all of which utilize integral-slot windings. These days, fractional-slot windings are often preferred over integral-slot windings because they can reduce torque ripple, manufacturing cost, and end-turn length. In [47], fractional-slot DPNV windings are explored, but the results only apply to bearingless consequent-pole and ac homopolar motors. There is not currently any design method or analysis of the acceptable combination of slots, poles, and phases to construct DPNV windings for a general machine.

This chapter overcomes the above shortcomings by deriving DPNV winding requirements and proposing a design procedure applicable to a general machine. Other notable contributions include presenting examples of many popular winding designs, including concentrated windings, where the end-connections have been modified to construct DPNV windings; and investigating performance differences of example bearingless motors utilizing conventional and DPNV winding designs. Because the required end-connection modifications come at virtually no penalty in terms of machine performance or cost, the results of this chapter will be useful to bearingless motor designers looking for complete magnetic levitation as well as designers of conventional motors looking to suppress rotor vibrations while still utilizing mechanical bearings.

In this chapter, Section 6.2 introduces the DPNV winding concept; Section 6.3 describes the chapter's use of the phasor star and defines terminology necessary for understanding the derivations; Section 6.4 derives the DPNV winding requirements; Section 6.5 proposes and describes a DPNV winding design procedure; Section 6.6 uses FEA results to validate the DPNV winding concept–example bearingless motor designs are explored and compared using both DPNV windings and conventional bearingless windings; Section 6.8 summarizes relevant fractional slot winding theory. Nomenclature used throughout the chapter is defined in Table 6.1.

6.2 Dual purpose no voltage windings

As described in the introduction, bearingless radial-flux motors can be classified into two categories as follows: $p_s = p \pm 1$ (bearingless versions of traditional motors) and $p_s = 1$ (bearingless consequent-pole and ac homopolar motors); the operating principles for each can be found in Chapters 7 and 14 of [56] and are briefly described in Section 7.2. The stator winding for any category of a bearingless motor is responsible for generating two airgap flux densities: a p pole-pair field for torque production and a p_s pole-pair field for suspension force production. While conventional bearingless motors use separate windings (and therefore separate coils) for creating each field, the DPNV windings described in this chapter use a single winding (the same coils) for creating both fields.

The defining features of a DPNV winding can be summarized as: 1) using the same coils to construct a p pole-pair torque MMF and a p_s pole-pair suspension MMF; 2) having suspension terminals which connect to the same coils as the torque terminals, but with half of the coils' direction reversed so that these terminals experience no motional-EMF. Two different styles of drive connection have been proposed to interface with a DPNV winding. The first is the bridge configuration, shown in Fig. 6.1a. This was proposed in [109] with further development in [99, 105]. It features coils connected in a manner resembling a wheatstone bridge and uses isolated single-phase inverters to inject currents into the suspension terminals. The second is the parallel configuration, proposed in [111] and shown in Fig. 6.1b. Here, the suspension winding terminals appear as a virtual "neutral" for the motor winding, meaning that the suspension inverter must also carry half of the motor current, and non-isolated multi-phase inverters are used to

Table 6.1: Chapter nomenclature

α_{ph}	Winding phase angle, $= 360/m$, $180/m$ for normal and reduced phase machines.
$\alpha^{\mathrm{e}}_{i,h}$	Phasor angle of slot i coil-side at frequency h.
α^{e}_{s}, α^{e}_{t}	Electrical angle at the sus., torque frequency.
$\alpha^{\mathrm{e}}_{u,h}$	Angular separation between slot phasors of adjacent slots at frequency h, $= h \times 360/Q$.
h	Harmonic index or electric frequency.
$k_{t,h}$, $k_{s,h}$	Torque, sus. winding factor at frequency h.
m	Number of winding phases.
n	Reduced denominator of q.
$\mathbb{N}$	Set of natural numbers.
$\mathbb{N}_{\mathrm{even}}$	Set of even natural numbers.
$\mathbb{N}_{\mathrm{odd}}$	Set of odd natural numbers.
p, p_s	Pole-pairs of the torque, sus. winding.
p'	Number of pole-pairs before torque magnetic conditions repeat for a slot, $= p/t$.
p^*	Pole-pairs in a torque base winding.
q	Slots per pole per phase, $= z/n$.
Q	Number of stator slots.
Q_{ph}	Number of slots separating adjacent phases.
Q'	Number of phasors in the torque phasor star, $= Q/t$.
Q^*	Number of slots in the torque base winding.
Q^*_{ph}	Number of slots separating adjacent phases in a base winding.
t	Greatest common divisor of Q and p.
y	Coil span, specified as a number of slots.
z	Reduced numerator of q.
z_c	Number of stator coils.

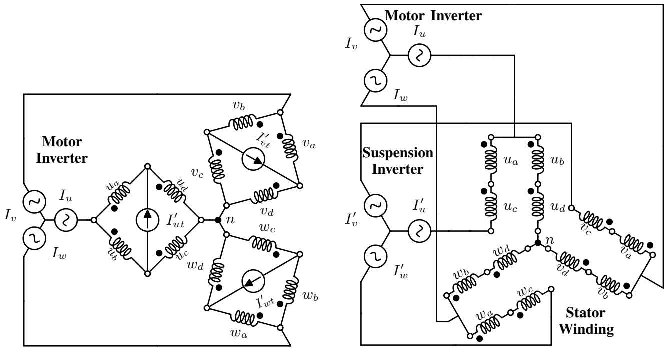

(a) Bridge connection (b) Parallel connection

Figure 6.1: Drive connections of the two styles of DPNV drives for use with $p \pm 1$ and consequent-pole bearingless motors. Modified diagrams are shown in Fig. 7.3 for the bearingless ac homopolar motor.

inject currents.

An example machine with a DPNV winding is shown in Fig. 6.2. The slot current direction and airgap MMF are indicated in Fig. 6.2a and 6.2b when the coils are excited with current from the torque and suspension terminals. The airgap field when a radial force is being produced is shown in Fig. 6.2c. Every inductor symbol in Fig. 6.1 represents a group of coils, denoted by the subscript *a*-*d* for each phase. For this simple example, each coil group consists of only a single coil, which is indicated in Fig. 6.2d for phase u.

A coil group can be modeled as shown in Fig. 6.2e where the voltage source represents the sum of the motional-EMF and coupling with other coil groups. The DPNV winding is designed so that the voltage source magnitude and phase are equivalent for groups a and b and groups c and d. In both connection styles, the voltage sources cancel from the suspension terminal perspective, which results in the no-voltage characteristic. However, in the parallel connection, a voltage drop across the RL branch due to suspension current appears at the torque terminals, which is minimal if the machine is designed with low leakage inductance. To obtain these characteristics, careful winding design is needed. This chapter derives generalized design requirements and a procedure, presented in Sections 6.4 and 6.5.

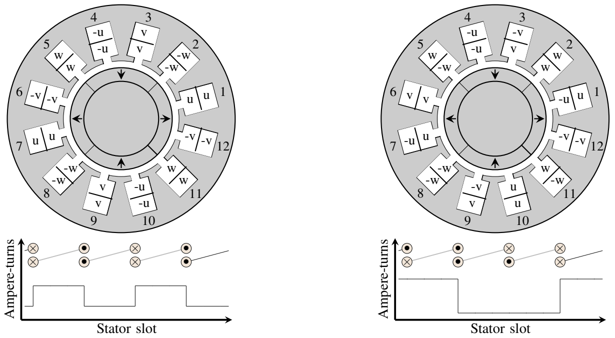

(a) Torque excitation (4-poles) (b) Sus. excitation (2-poles)

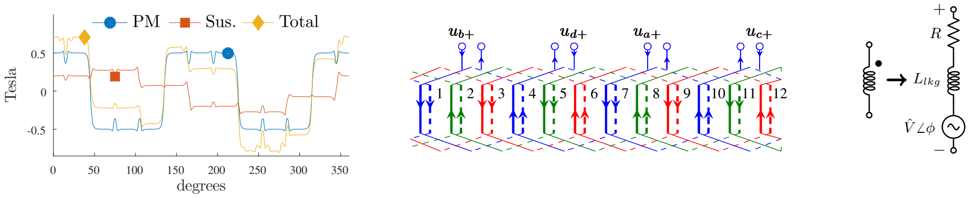

(c) Airgap field (d) Winding schematic (e) Coil group model

Figure 6.2: Example DPNV winding for a PM motor with $Q = 12$, $p = 2$, $p_s = 1$: (a), (b) slot current direction and phase u MMF when positive current is flowing into the torque or suspension terminals; (c) the airgap field when excited with x-force producing suspension current and no torque current; (d) the winding schematic with phase u terminal connections labeled ('+' terminals correspond to the dotted terminals in Fig. 6.1); (d) equivalent model of a coil group.

6.3 Winding design theory and properties

This chapter relies heavily on fractional-slot winding design theory and a summary of the relevant details and terminology can be found in Section 6.8. This section describes how the chapter utilizes various concepts of this theory as well as important properties of bearingless motors.

6.3.1 Phasor star diagram

The phasor star, or star of slots, is a diagram that indicates the phasor of a particular harmonic of EMF that would be induced in each coil-side if the airgap contained a rotating sinusoidal radial flux density at that harmonic frequency. An example is shown in Fig. 6.3. The individual phasors of the star are termed "slot phasors" and are numbered to indicate the slot where the coil-side is located. Separate phasor star diagrams are constructed for each frequency of interest. For the fundamental frequency, there will be t phasors at each angular location and therefore t levels to the phasor star. The winding factor for a particular harmonic can be calculated from that hamonic's phasor star by (6.1), for a phase consisting of N coil sides. The electrical frequency is the frequency of the harmonic of interest (for the fundamental frequency, $h = p$). Coils are made up of two coils-sides: one connected in a positive direction and one connected in a reverse direction. When coils are placed in the final winding, individual coils may be connected in reverse. For coil-sides connected in reverse, $\alpha^{\mathrm{e}}_{i,h}$ is rotated by 180^{e} when used in (6.1). The phasor star is always drawn without regard to the connection direction.

$$k_h = \mathrm{abs}\left(\frac{1}{N}\sum_{i=1}^{N} e^{j\alpha^{\mathrm{e}}_{i,h}}\right) \tag{6.1}$$

To simplify the case of a double-layer winding, all coils are assumed to span the same number of slots and the returning coil-side is neglected from the phasor star, meaning that only a single phasor is drawn for each slot. The terms "slot phasor" and "coil phasor" are used interchangeably when referring to a double layer winding. The only effect this has on the analysis is that the winding factor calculation of (6.1) is redefined as being the winding distribution factor (where N is redefined as the number of coils).

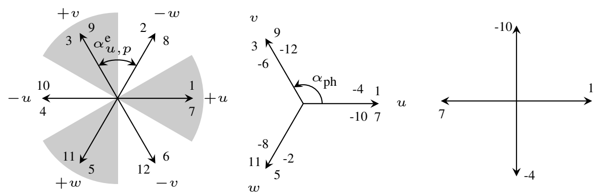

Torque phasor star

Torque connection star

Torque phase u connection star drawn at $h = p_s$

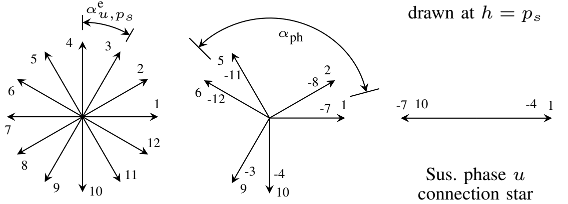

Sus. phasor star

Sus. connection star

Sus. phase u connection star drawn at $h = p$

Figure 6.3: Phasor and connection star diagrams for the winding of Fig. 6.2; the torque phasor star has 60^{e} phase belts drawn. The phasor numbers indicate the coil-side slot, with negative numbers for coil sides connected in reverse.

To calculate the total winding factor, the distribution factor is then multiplied by a pitch factor.

6.3.2 Key terminology

The torque and suspension frequencies are defined as the fundamental frequencies of the torque and suspension windings, which is equal to p and p_s. A torque or suspension phasor is a slot phasor drawn at the torque or suspension frequency. The terms torque phasor, suspension phasor, and slot phasor always indicate a coil-side's phasor without regard to the connection direction (without the 180^{e} rotation for reverse connections). The torque and suspension winding factors are calculated assuming that only the torque or suspension terminals are present. The winding phase angle α_{ph} is the angular separation of winding phases. Torque and suspension phasor stars are phasor stars drawn at the torque and suspension frequencies. A winding connection star is a phasor star redrawn to take into account the connection direction of the coil-sides in the final winding. Torque and suspension connection stars are drawn for the torque or suspension terminal connections at their fundamental frequency (p or p_s, respectively) unless otherwise indicated. The individual phasors of the connection star are referred to as connection phasors. These concepts are illustrated in Fig 6.3.

6.3.3 Winding layout techniques

Winding layout techniques are used to assign the coil-side direction and to assign the coils to each phase. The two most common techniques are referred to as the zone diagram and phasor star approaches. The zone diagram is often used for laying out single layer windings because it typically results in a more even distribution of coil groups and therefore more satisfactory harmonic content and end-connection length. The phasor star approach can be used for both single and double layer windings, but is most popular for double layer windings. In this approach, phase bands, typically with an angular width of $180^{\mathrm{e}}/m$, are drawn on top of the phasor star to assign coils to each phase. An example of this is shown in Fig. 6.3. More information on both approaches can be found in Chapter 2 of [76]. Restrictions on these approaches for DPNV windings are considered in Section 6.4.4.

6.3.4 Relevant bearingless motor and DPNV winding properties

Relevant properties are summarized in the following paragraphs that are used throughout the chapter.

The radial flux bearingless motors considered have co-prime values of p and p_s.

From Fig. 6.1 it is seen that windings used in the bridge configuration must have a multiple of four coils per phase,

$$\frac{z_c}{m} = 4k. \tag{6.2}$$

Windings used in the parallel configuration must have a multiple of two coils per phase,

$$\frac{z_c}{m} = 2k. \tag{6.3}$$

Combining (6.2) and (6.3) with (6.22) - (6.27) of Appendix 6.8, it can be shown that (6.4) is true for all DPNV windings.

$$\frac{p}{n} \in \mathbb{N} \tag{6.4}$$

Fractional slot winding definitions and calculations (i.e. q, t, Q', classification as first- or second-grade winding, etc.) are all based on the torque frequency.

Table 6.2: DPNV winding symmetry requirements derived in Section 6.4.1

Standard [76]	$z_c/m \in \mathbb{N}$ m and n must be co-prime
New	p and m must be co-prime p_s and m must be co-prime

6.4 Winding design requirements

Realizing the features of a DPNV winding imposes restrictions on the acceptable combinations of the number of stator slots Q, phases m, motor pole-pairs p, and suspension pole-pairs p_s. These restrictions are now investigated using fractional-slot winding theory and the necessary results are summarized in Tables 6.2, 6.3, and 6.4.

6.4.1 Symmetry requirements

Standard winding symmetry conditions that must be met to obtain a symmetric torque winding are summarized in the first two rows of Table 6.2.

Since the torque and suspension terminals connect to the same coils, the phase that a coil-side is assigned to when designing a torque winding will remain the same when viewed from the suspension terminals. For this to result in a symmetric winding from the suspension terminal perspective, there must exist pairs of slot phasors which are separated by a multiple of the winding phase angle α_{ph} at both the torque and suspension frequencies. This requirement can be written as

$$\begin{aligned} b\alpha_{\mathrm{ph}} &= \alpha^{\mathrm{e}}_{u,s} Q_{\mathrm{ph}} \\ &= p_s \frac{360}{Q} \left[Q^*_{\mathrm{ph}} + cQ^* \right] \end{aligned} \tag{6.5}$$

where b is an integer which must be co-prime with m to obtain unique phase angles; c is an integer for a normal phase machine and an integer multiple of $1/2$ for a reduced phase machine. It can be shown that suitable values for b and c can only be obtained when both p_s and p are co-prime with m. Note that this means that reduced phase machines can only result in symmetric DPNV windings for the consequent pole and ac homopolar bearingless motors.

Table 6.3: DPNV winding no-voltage requirements derived in Section 6.4.2

	First-grade		Second-grade	
Layers	Single	Double	Single	Double
Parallel configuration	$\frac{Q}{4m} \in \mathbb{N}$	$\frac{Q}{2m} \in \mathbb{N}$	$\frac{t}{4} \in \mathbb{N}$	$\frac{t}{2} \in \mathbb{N}$
Bridge configuration	$\frac{Q}{8m} \in \mathbb{N}$	$\frac{Q}{4m} \in \mathbb{N}$	$\frac{t}{8} \in \mathbb{N}$	$\frac{t}{4} \in \mathbb{N}$

Table 6.4: DPNV winding suspension winding distribution factor requirements derived in Section 6.4.3

	Defining features[a]	Requirement[b]
Type 1	Identical torque, opposing suspension	$p \in \mathbb{N}_{\text{even}}$
Type 2	Opposing torque, identical suspension	$p \in \mathbb{N}_{\text{odd}}$, $p_s \in \mathbb{N}_{\text{even}}$
Type 3	All other cases	$p \in \mathbb{N}_{\text{odd}}$, $p_s = 1$, $t > 1$

---

[a] The features are given in terms of the phasor behavior, shown in Fig. 6.4.

[b] Windings must also meet the requirements summarized in Tables 6.2 and 6.3.

6.4.2 No voltage requirements

For the DPNV winding to have no motional-EMF present at the suspension terminals, the suspension winding factors must be zero at the torque frequency and its harmonics. This is achieved by reversing half of the coils' direction for connection to the suspension terminals and can be illustrated through the torque connection star. In this diagram, there needs to be an even number of phasors present at each angular location so that half of the phasors can be rotated 180^{e} (by reversing the direction of half of the coils) to cancel the non-rotated phasors. In order to obtain these phasors in the torque connection star, necessary limitations on Q, m, and p are now considered. Furthermore, it is also necessary that the phasors which are to cancel each other belong to different coils in the same phase; this restricts the winding layout approach and is considered in Section 6.4.4. Symmetric windings are classified as being either first or second grade (see Appendix 6.8) and requirements for each of these types are considered separately.

First-grade windings

These windings produce torque phasor stars that have slot phasors in 180^{e} pairs. When the torque connection star is drawn, each base winding will have two identical torque phasors at each angular location. In other words, the base winding automatically satisfies the no voltage condition and the designer must only make sure that the winding has enough coils. Using (6.26) and (6.27) in (6.3) and (6.2), the requirements can be obtained, as summarized in Table 6.3.

Second-grade windings

The torque phasor stars produced by these windings do not contain phasors in 180^{e} pairs, which means that a base winding must repeat an even number of times to satisfy the no voltage requirement. Doing so guarantees an even number of coils per phase, satisfying the parallel configuration's coil requirement. Since the number of coils per phase of second-grade base windings is odd, the bridge winding further requires that the base winding repeat a multiple of four times. Single layer second-grade base windings are twice the length of their double-layer counterpart, doubling t. The result is summarized in Table 6.3.

6.4.3 Non-Zero suspension winding distribution factor

In addition to canceling the motional-EMF (Section 6.4.2), reversing the direction of half of the coils must also result in a non-zero suspension winding factor. Windings where this is possible can be grouped into three categories based on their slot phasors, as follows:

1. For each slot, there exists a corresponding slot which has an identical torque phasor and a suspension phasor which is 180^{e} out of phase, see Fig. 6.4a.

2. For each slot, there exists a corresponding slot which has a torque phasor 180^{e} out of phase and an identical suspension phasor, see Fig. 6.4b.

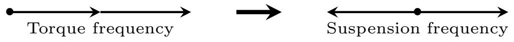

(a) Type 1 slot phasor transformation

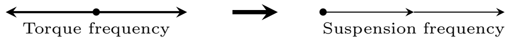

(b) Type 2 slot phasor transformation

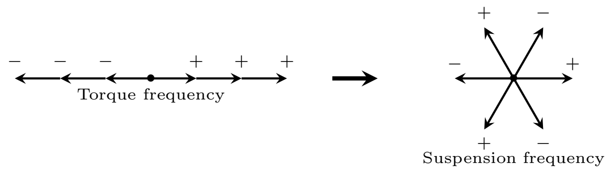

(c) Type 3 slot phasor transformation

Figure 6.4: DPNV winding type classification. Winding phasor star diagrams drawn at the torque and suspension frequencies to depict the slot phasor behavior that defines (a) Type 1, (b) Type 2, and (c) Type 3 windings. Note that the phasor stars are incomplete and only depict the relevant slot phasors. In (c), the − and + signs are used to keep track of the transformation of the two groups of slot phasors.

3. The slot phasors do not meet Type 1 or Type 2 conditions but the winding can still be configured to produce a non-zero suspension MMF, see Fig. 6.4c.

Requirements of each of these types of windings is summarized in Table 6.4 and derived below.

Type 1

Two slot phasors displaced by a specific multiple of 360^{e} at the torque frequency must be displaced by an odd multiple of 180^{e} at the suspension frequency,

$$k_s \times 180 = \tfrac{p_s}{p} h_1 \times 360 \tag{6.6}$$

where h_1 is the integer number of pole-pairs between the identical torque phasors that allows an integer k_s and must be less than p; k_s represents the number of suspension poles between the 180^{e} suspension phasors and is therefore an odd integer less than $2p_s$. Since $p_s h_1$ is an integer, p must be restricted to (6.7). Equation (6.6) can be solved for

h_1 (6.8).

$$\frac{p}{2} \in \mathbb{N} \tag{6.7}$$

$$h_1 = \frac{k_s}{p_s}\frac{p}{2} \tag{6.8}$$

Since p and p_s are co-prime, $k_s = p_s$ and therefore $h_1 = p/2$. This means that a slot must exist every h_1 pole-pairs, requiring

$$\frac{h_1}{p^*} \in \mathbb{N}. \tag{6.9}$$

Using the values of p^* from Table 6.8, it can be shown that any first-grade and double-layer second-grade winding requires

$$\frac{t}{2} \in \mathbb{N} \tag{6.10}$$

while any second-grade single-layer winding requires

$$\frac{t}{4} \in \mathbb{N}. \tag{6.11}$$

It can be seen from (6.23) and (6.10) that any first-grade winding satisfying (6.7) will be a Type 1 winding. Any second-grade winding satisfying the requirements of Table 6.3 will satisfy (6.10) or (6.11) and, it can be seen from (6.25), will satisfy (6.7) and therefore be a Type 1 winding. In summary, any winding that meets the no-voltage requirements and has an even number of pole-pairs will be a Type 1 winding.

Type 2

Two slot phasors displaced by a specific odd multiple of 180^{e} at the torque frequency must be separated by a multiple of 360^{e} at the suspension frequency,

$$k_s' \times 360 = \tfrac{p_s}{p} h_2 \times 180 \tag{6.12}$$

where k_s' is the number of pole-pairs between the identical suspension phasors and must be less than p_s; h_2 is the number of poles separating the torque phasors and must be an odd integer less than $2p$. This can be re-written as

$$h_2 = \frac{2k_s'}{p_s} p. \tag{6.13}$$

Since p and p_s are co-prime and h_2 is odd, it is required that:

$$p \in \mathbb{N}_{\text{odd}} \tag{6.14}$$

$$p_s \in \mathbb{N}_{\text{even}} \tag{6.15}$$

which results in $k'_s = p_s/2$ and $h_2 = p$. In addition to this, the torque phasor star needs to have 180^{e} torque phasor pairs present, which means the winding must be a first-grade winding. In fact, first-grade windings are the only windings that can meet both (6.14) and the no-voltage conditions of Table 6.3; this can be seen from (6.4) and Table 6.8, which indicate that a second grade no voltage winding will have $t \in \mathbb{N}_{\text{even}}$, which is not possible when (6.14) is true.

In summary, any no-voltage winding that satisfies (6.14) and (6.15) will be a Type 2 no-voltage winding.

Type 3

The remaining windings have

$$p \in \mathbb{N}_{\text{odd}} \tag{6.16}$$

$$p_s \in \mathbb{N}_{\text{odd}} \tag{6.17}$$

which corresponds to the case of a bearingless consequent pole or ac homopolar motor when $p \in \mathbb{N}_{\text{odd}}$. These are first-grade windings and will therefore have $t \in \mathbb{N}_{\text{odd}}$ due to (6.16), torque phasors separated by 180^{e}, and may have torque phasors separated by 360^{e} if $t > 1$. Slots which have torque phasors separated by multiples of 180^{e}, will have suspension phasors separated by

$$\alpha_s^{\text{e}} = \tfrac{1}{p} h' \times 180 \tag{6.18}$$

where h' is the number of poles between all torque phasors displaced by multiples of 180^{e}. Since 180^{e} phasors occur every p' poles, h' will take on values of all integer multiples of p' less than $2p$. The resulting suspension angles will be

$$\alpha_s^{\text{e}} = k' \frac{180}{t}, \qquad k' = 1, ..., 2t - 1. \tag{6.19}$$

Therefore, to have a non-zero suspension winding factor after half of the phasors have been rotated 180^{e}, it is required that

$$t > 1. \tag{6.20}$$

6.4.4 Layout requirements

In the case of Type 1 windings, the no-voltage requirement is satisfied between the different base windings. For any winding with $Q^* = Q'$, this means that stator slots can be assigned using any winding layout approach that realizes the minimum base winding length Q^*. For second grade, single layer windings (where $Q^* = 2Q'$), the layout approach must guarantee that adjacent phases are repeated with a slot separation of Q^*_{ph}, which the zone diagram approach guarantees, but the phasor star approach does not.

In Type 2 and Type 3 windings, the no-voltage requirement is satisfied within a single base winding by the inclusion of 180^{e} separated torque phasors in the same phase. The phasor star approach with $180^{\mathrm{e}}/m$ phase belts guarantees that these phasors will be present in the same phase, while the zone diagram approach does not. Therefore, the phasor star approach is recommended for both single and double layer windings when the winding type is 2 or 3.

6.5 Winding design procedure

The design procedure proposed here is intended to enable the designer to modify a conventional motor winding to function as a DPNV winding. It is assumed that the designer will specify the number of motor poles and phases required which complies with Table 6.2. To transform an existing winding design into a DPNV winding, the designer should first verify that the winding satisfies the requirements of Tables 6.2, 6.3, and 6.4 and then skip ahead to Section 6.5.3.

6.5.1 Table of permissible windings

It is recommended that the designer construct a table of permissible designs that meet their torque winding requirements. To do this, the following procedure is proposed:

1. Table 6.2 is used to determine acceptable values for p_s.
2. A list of potential values of n is created using (6.4).
3. For each value of n:

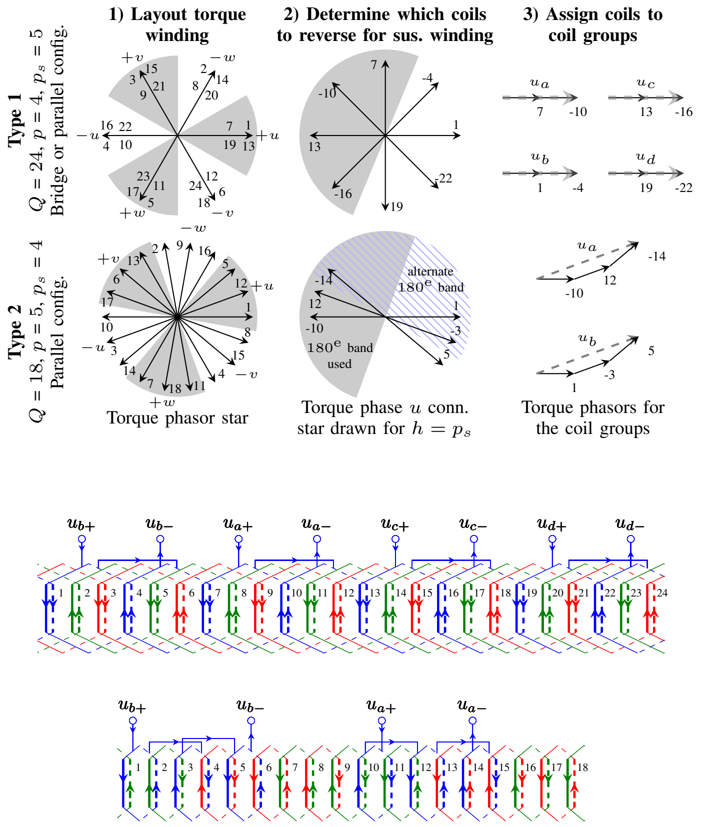

Resulting winding layouts

Figure 6.5: The design steps of Section 6.5.3 applied to two example DPNV winding entries in Table 6.5.

(a) the winding grade is determined from Table 6.8;

(b) t is calculated using (6.23) or (6.25);

(c) for a second-grade winding, t is checked against Table 6.3; for a Type 3 winding, t is checked against Table 6.4. Any values of n which fail are removed.

4. Permissible values of z are determined by requiring that z and n are co-prime.

5. Acceptable values of Q are found using (6.22) and (6.24). For first grade windings, Q is checked against Table 6.3.

6. The results are compiled into a table with rows for each Q value; i.e. see Table 6.5, discussed later.

6.5.2 Select coil span

The effect of coil span should be carefully considered. When all coils have the same span, the pitch factor is (6.21)

$$k_{p,h} = \sin(h\frac{\alpha_y}{2}) \tag{6.21}$$

where α_y is the angular pitch of each coil [76]. Maximizing the coil pitch factor for the torque frequency may result in a low value at the suspension frequency and an unacceptably low suspension force rating. This is especially true when the relative difference in the two frequencies is very large, i.e. when p is small or when $p_s = 1$. The pitch factor may also be used to prevent harmonics that would otherwise create force ripple. The design in Section 6.5.3 is significantly constrained and will often result in large suspension winding distribution factors for $h \neq p_s$ which can be suppressed by $k_{p,h}$.

6.5.3 Design each winding in the table

For each entry in the design table generated in Section 6.5.1, the designer should perform the following steps.

First, the layout should be conducted for the torque winding. Section 6.4.4 should be used to select a layout approach.

Second, the torque connection star of a single phase should be drawn at the suspension frequency and half of the connection phasors should be selected to rotate 180^{e} (the coils to reverse for connection to the suspension terminals) in a way that 1) cancels all phasors at the torque frequency and 2) results in a non-zero suspension winding distribution factor. The approach to doing this is described below for each of the winding types defined in Table 6.4.

Finally, the designer must assign the coils to coil groups *a*-*d*, depicted in Fig. 6.1. Groups *a* and *c* should only contain coils which have been reversed for connection to the suspension terminals. Furthermore, the vector sum of the torque connection phasors of groups a and b must be equivalent and groups c and d must be equivalent. For parallel drive connections, groups c and d need not exist.

Type 1 and Type 2

The results of Section 6.4.3 indicate that any 180^{e} band of connection phasors (from each phase of the torque connection star drawn at the suspension frequency) can be selected for rotation. The angular separation of the connection phasors is not guaranteed to be uniform, meaning that in some cases selecting one 180^{e} band over another will result in more optimal suspension winding distribution factors. An example of the design steps applied to these types of windings is shown in Fig. 6.5.

Type 3

The results of Section 6.4.3 indicate that unlike Type 1 and 2 windings, an arbitrary 180^{e} band of torque connection phasors cannot be used for rotation. From (6.19) and noting that $t \in \mathbb{N}_{\text{odd}}$, it can be shown that the resulting torque connection star (drawn at the suspension frequency) will consist of $2t$ phasors at t equally spaced angular locations, as shown in Fig. 6.6a. From this star, acceptable combinations of torque connection phasors can be identified and rotated to cancel the motional-EMF and create a non-zero suspension winding factor. If the torque phase connection star contains phasor groups rotated $\alpha_t^{\mathrm{e}} \neq 180^{\mathrm{e}}$, each of these phasor groups will result in additional suspension phasor groups as shown in Fig. 6.6b. Type 3 windings use suspension current in an especially inefficient manner, as the MMFs of some coils end up canceling each other.

6.5.4 Design selection

The designer must now select the final winding to use. To do this, it is recommended to add performance metrics as columns in the table generated in Section 6.5.1. Common metrics have been added to Table 6.5. These include the ratio of k_{s,p_s} to $k_{t,p}$, which predicts how effectively the machine uses current to produce radial forces, and results obtained via FEA: the rated average force along an axis (i.e. $\langle F_x \rangle$ for an x-axis force), the normalized maximum deviation from the average of the force waveform along the principle axis (i.e. $\Delta F_x / \langle F_x \rangle$), and the normalized maximum value in the force waveform

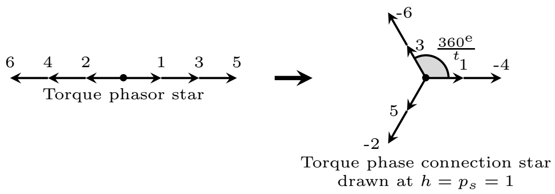

(a) Single set of torque phasors displaced by 180^e

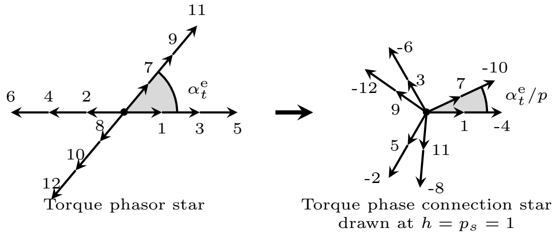

(b) Multiple sets of torque phasors displaced by 180^e

Figure 6.6: Example single phase Type 3 winding diagrams when $t = 3$

along an axis orthogonal to the desired force direction (i.e. $\Delta F_y / \langle F_x \rangle$).

6.6 Validation of DPNV winding design

FEA and experimental results are now used to validate the DPNV concept. This is done by considering several designs based around popular motor windings: first as transformed DPNV windings and second with conventional (separate) suspension windings. Finally, experimental validation of the DPNV concept is presented through results from a hardware prototype of a bearingless ac homopolar motor.

6.6.1 Survey of various DPNV designs

Performance parameters calculated with FEA for several example bearingless motors are summarized in Table 6.5. Each of these DPNV windings was designed using the procedure proposed in Section 6.5. To make an accurate comparison between designs, several parameters were normalized, as specified in Table 6.6, using slot dimensions defined in Fig. 6.8a. Concentrated slot windings are in bold and indicated by $y = 1$. The quality of the designs varies significantly in terms of force ripple and capability.

Table 6.5: Example winding design table[a]

p	p_s	Q	q	y	$\frac{k_{s,p_s}}{k_{t,p}}$	T[b]	$\frac{\langle F_x \rangle}{\text{Len}}$ [c]	% $\frac{\Delta F_x}{\langle F_x \rangle}$	% $\frac{\Delta F_y}{\langle F_x \rangle}$
$p \pm 1$ bearingless motors									
1	2	6	1	2	1	P	11.5/8.6	45 / 4	44 / 2
		12	2	5	0.464	BP	5.9/4.2	62 / 3	52 / 2
2	1	**6**	$\boldsymbol{\frac{1}{2}}$	**1**	**0.577**	**P**	**9.3/5.6**	**16 / 11**	**15 / 14**
		12	1	3	0.5	BP	9.0/5.6	26 / 3	21 / 2
		18	$\frac{3}{2}$	4	0.501	P	9.8/6.0	13 / 1	14 / 0
		24	2	6	0.513	BP	10.4/6.3	10 / 1	9 / 1
4	5	**12**	$\boldsymbol{\frac{1}{2}}$	**1**	**0.789**	**BP**	**5.1/4.0**	**6 / 4**	**9 / 5**
		18	$\frac{3}{4}$	2	1	P	6.6/5.2	22 / 2	20 / 1
		24	1	3	0.604	BP	4.1/3.2	31 / 1	25 / 1
		36	$\frac{3}{2}$	4	0.707	BP	4.8/3.8	20 / 0	20 / 0
5	4	**12**	$\boldsymbol{\frac{2}{5}}$	**1**	**0.804**	**BP**	**2.7/1.3**	**30 / 26**	**33 / 29**
		18	$\boldsymbol{\frac{3}{5}}$	**1**	**0.839**	**P**	**3.0/1.5**	**9 / 5**	**8 / 2**
		30	1	3	0.616	P	2.3/1.1	44 / 0	49 / 0
$p_s = 1$ bearingless motors									
4	1	**12**	$\boldsymbol{\frac{1}{2}}$	**1**	**0.211**	**BP**	**3.5/4.2**	**48 / 40**	**53 / 41**
		18	$\frac{3}{4}$	2	0.305	P	5.5/6.6	15 / 11	13 / 11
		24	1	3	0.25	BP	4.7/5.7	13 / 11	17 / 12
		36	$\frac{3}{2}$	4	0.216	BP	4.0/5.0	13 / 11	12 / 11

---

[a] All designs have $m = 3$ and are double layer. Several of the winding layouts are depicted in Fig. 6.2, 6.5, and 6.8b.

[b] Configurations that are supported: 'B' for bridge, 'P' for parallel.

[c] $\frac{\langle F_x \rangle}{\text{Len}}$, $\frac{\Delta F_x}{\langle F_x \rangle}$, $\frac{\Delta F_y}{\langle F_x \rangle}$ are specified as Square/Sine. $\frac{\langle F_x \rangle}{\text{Len}}$ is in units of $\frac{\text{N}}{\text{mm}}$

Table 6.6: Model parameters for designs in Table 6.5

	$p \pm 1$	$p_s = 1$
$\hat{A}_p$ (A/mm)[a]	40	20
$\hat{B}_{m,p}$ (T)[b]	0.6	0.2
b_1/τ_u	0.15	0.15
w_t/w_s	0.85	0.85
t_{ps} (mm)	1.25	1.25
Airgap Length (mm)	2	2
Airgap Radius (mm)	53	53
Laminations	Hiperco 50A	M19

---

[a] Linear current density at the torque frequency

[b] Magnitude of magnetizing airgap flux density at the torque frequency

Machines with less harmonic content in the magnetizing field (‘sine’ data points, explained below) have much less force ripple, which indicates that careful optimization of the machine geometry (slot opening, tooth thickness, pole pitch, etc.) will yield large improvements in machine performance. Modeling details specific to the two types of bearingless machines are as follows:

$p \pm 1$ designs

Transient 2D, non-linear FEA was carried out on surface-mount PM machines with full pitch magnets. Both radially and sinusoidally mangetized PMs were considered, referred to as “square” and “sine” rotors. This represents a worst and best case scenario for unwanted airgap flux density harmonics, and gives an indication of the range of force ripple that a given winding may achieve. To obtain the magnetic loading specified in Table 6.6, the sinusoidally magnetized PMs are substantially thicker than the radially magnetized PMs (approx. 5.8mm vs 2.7mm). These thicker magnets have the effect of decreasing the armature reaction flux density, which results in lower rated radial forces. Fig. 6.7a shows an example of the flux density distribution for these two cases.

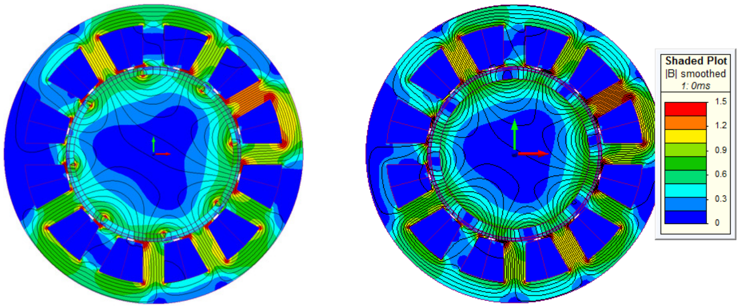

(a) $Q = 12$, $p = 4$, $ps = 5$ flux density while producing x force

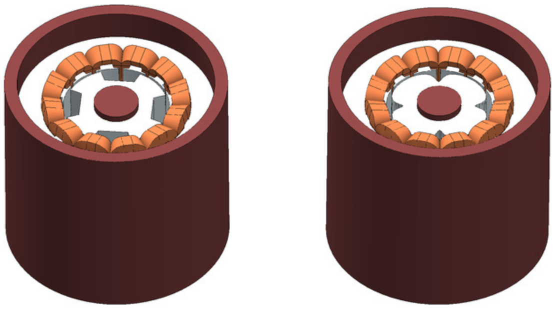

(b) 3D FE models for $Q = 12$ ac homopolar winding design

Figure 6.7: FEA models. The left-most images correspond to “square” rotors and the right-most to “sine” rotors.

$p_s = 1$ designs

Static 3D non-linear FEA was carried out on ac homopolar machines where the rotor’s angular position was swept. Only 8 pole designs were considered as this is the most common implementation. Two rotor structures were used to change the harmonic content of the magnetizing flux density: a “square” rotor (square airgap length profile) and a “sine” rotor (inverted sinusoidal airgap length profile), see Fig. 6.7b. The airgap has the same minimum length (specified in Table 6.6), which requires a greater field excitation to be used with a sine rotor to obtain the same $B_{m,p}$ value. This resulted in the sine rotor having a greater circulating homopolar flux and therefore a greater force capability. However, note that from a motor design perspective, the sine rotors are at a disadvantage because the machine has to carry greater flux to achieve the same torque as the square rotors.

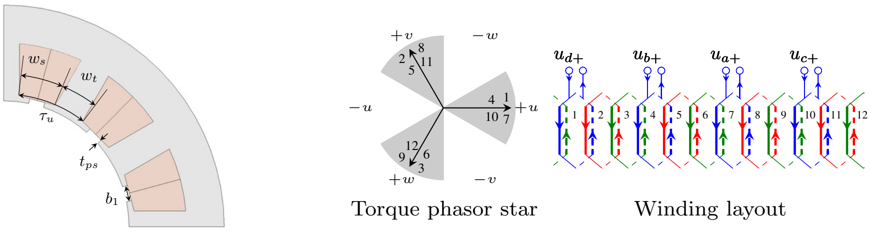

(a) Stator slot dimensions (b) Winding design

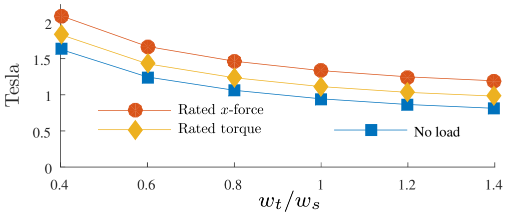

(c) Maximum flux density at tooth center

Figure 6.8: Design information for the $Q = 12$, $p = 4$, $p_s = 5$ entry in Table 6.5.

6.6.2 Detailed study of $Q = 12$, $p = 4$, $p_s = 5$ DPNV winding

The square rotor design from Table 6.5 is now studied in more detail. The winding layout is shown in Fig. 6.8b and terminal voltage waveforms are shown in Fig. 6.9. As expected, the suspension terminals do not experience any voltage due to the rotor's rotation or the torque terminal current; under rated suspension current, a suspension terminal voltage appears due to the RL branch of each coil group (Fig. 6.2e). The parallel configuration's torque terminals see a voltage due to these same RL branches (described at the end of Section 6.2) which may need to be accounted for in the motor drive if the designer is unable to sufficiently reduce it.

Next, the impact of the slot opening and tooth thickness was considered for three operating conditions: 1) no stator currents; 2) rated torque, no suspension current; and 3) rated suspension, no torque current. The ratio of the tooth thickness to slot width was swept to obtain designs with varying degrees of tooth staturation, as shown in Fig. 6.8c. In all resulting designs, the suspension terminals never exhibit any voltage for cases 1 and 2. For case 3, the peak suspension terminal voltage of the parallel configuration is plotted as a function of slot opening and tooth thickness on the left side of Fig. 6.10. This voltage exhibits a large dependence on the slot opening, but less dependence on the tooth thickness, indicating that tooth-tip leakage inductance is the primary cause.

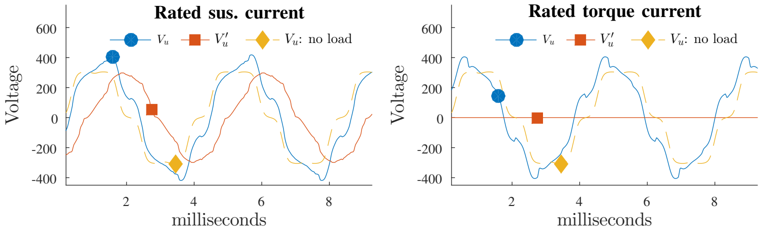

(a) Parallel connection

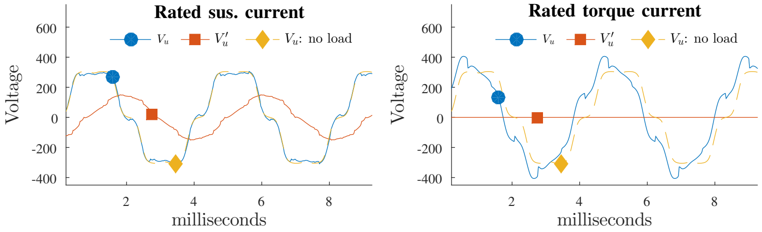

(b) Bridge connection

Figure 6.9: FEA voltage waveforms for the $Q = 12$, $p = 4$, $p_s = 5$ DPNV example. V_u corresponds to the torque phase u terminal voltage, V'_u corresponds to the suspension phase u terminal voltage, and "V_u: no load" corresponds to the torque phase u terminal voltage observed with no stator currents.

The impact of tooth thickness and slot opening on the force ripple (case 3) and torque ripple (case 2) is also shown in Fig 6.10. Increasing the slot opening decreases the force ripple at the expense of increasing torque ripple.

Finally, cross-coupling between force and torque production is investigated by solving the models under the following currents, specified as a fraction of rated current: 1) 75% torque, 25% suspension; 2) 75% torque, no suspension; 3) no torque, 25% suspension. The torque ripple and force ripple difference between case 1 and cases 2 or 3 are plotted in Fig 6.11, where very little difference in performance is observed. The results of this section indicate that this DPNV winding example functions well under various load conditions and that design optimization can be conducted to minimize problems of force ripple and suspension terminal voltage.

6.6.3 Comparison to conventional bearingless windings

Several DPNV designs from Table 6.5 were redesigned with conventional bearingless windings and their performance evaluated using FEA. In all cases, a square rotor is

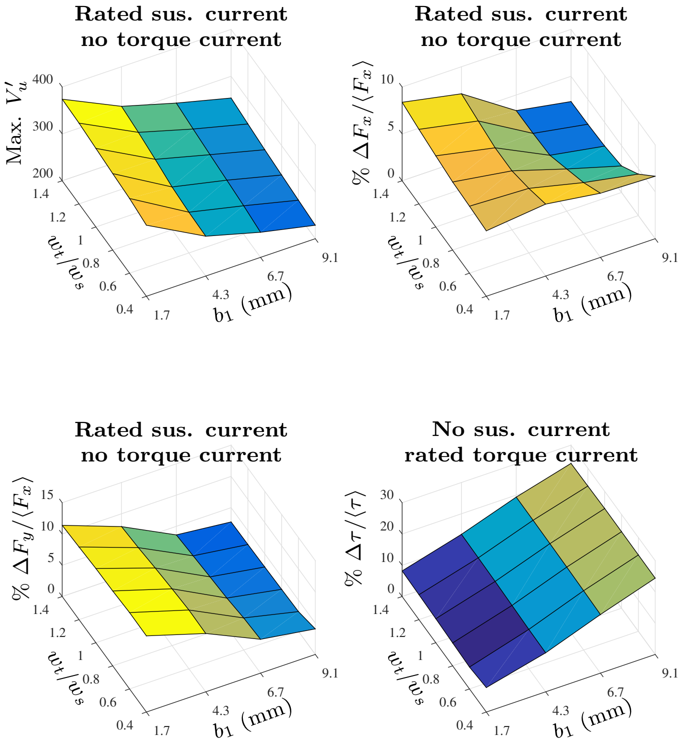

Figure 6.10: FEA results for the $Q = 12$, $p = 4$, $p_s = 5$ DPNV example design performance when the slot opening and tooth thickness are varied; $\Delta\tau/\langle\tau\rangle$ indicates the normalized torque ripple.

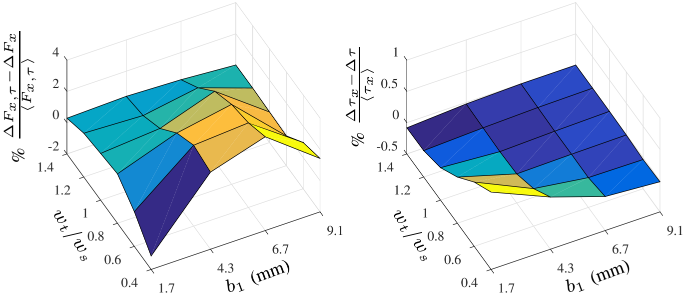

Figure 6.11: FEA results evaluating the machine performance during simultaneous force and torque production. $F_{x,\tau}$ is the x radial force produced with simultaneous torque and τ_x is the torque produced with simultaneous x force.

used, the double layer winding of the DPNV design becomes the torque winding, and a new suspension winding is added to the same slots. The resulting designs have three or four winding layers depending on whether a single or double layer suspension winding is used, whereas the DPNV windings had only two layers. To enable a direct comparison, the new designs have the same dimensions with the exception that 75% of the slot space is now permenantly allocated to the suspension windings, reducing the torque winding turns and therefore the machines' rated torque to 75% of the value of the DPNV designs.

The results from this study are presented in Table 6.7. Concentrated-slot designs are again indicated in bold. The difference in force ripple between conventional or DPNV windings for a design largely varies on a per-design basis, with each winding approach outperforming the other in certain designs. Many designs with conventional windings feature higher $k_{s,p_s}/k_{t,p}$ ratios, indicating that they would have higher suspension force capabilities if the entire slot space could be allocated to the suspension winding. However, this is not possible since the machine must also be able to produce the required torque. In the $Q = 6$, $p = 2$ example, the double layer suspension winding is actually identical to the DPNV design (from the suspension terminal perspective).

The winding layouts for the $Q = 12$, $p = 4$, $p_s = 5$ design are shown in Fig. 6.12 and voltage waveforms are shown in Fig. 6.13. These results can be compared to the DPNV waveforms for the same design in Fig. 6.9. Since the number of turns of the torque winding is reduced from the DPNV winding, the torque terminal voltage magnitude is also reduced. The single layer suspension winding has non-zero winding factors at multiples of the torque frequency, and therefore its suspension terminals experience a

Slot	1	2	3	4	5	6	7	8	9	10	11	12
L1	u	-u	w	-w	v	-v	u	-u	w	-w	v	-v
L2	-w	v	-v	u	-u	w	-w	v	-v	u	-u	w
L3	u'	-u'	u'	-u'	w'	-w'	w'	-w'	v'	-v'	v'	-v'

(a) With single layer suspension winding

Slot	1	2	3	4	5	6	7	8	9	10	11	12
L1	u	-u	w	-w	v	-v	u	-u	w	-w	v	-v
L2	-w	v	-v	u	-u	w	-w	v	-v	u	-u	w
L3	u'	-u'	-v'	v'	w'	-w'	-u'	u'	v'	-v'	-w'	w'
L4	u'	v'	-v'	-w'	w'	u'	-u'	-v'	v'	w'	-w'	-u'

(b) With double layer suspension winding

Figure 6.12: Slot coil sides in each stator winding layer for the example $Q = 12$, $p = 4$, $p_s = 5$ design with conventional bearingless windings. The coil sides for the torque winding are in the first two layers and are the same as the DPNV winding shown in Fig. 6.8b. The $'$ labels indicate suspension coil sides.

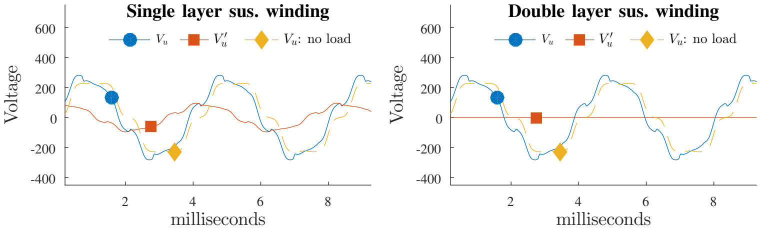

Figure 6.13: Voltage waveforms for $Q = 12$, $p = 4$, $p_s = 5$ designs with separate suspension windings when operated at rated torque and no suspension current.

motional-EMF (unlike the DPNV winding).

The conclusion of whether a DPNV winding is advantageous over a conventional winding must be made on a per-design basis. The primary benefits of a DPNV winding can be summarized as: 1) allowing the drive to dynamically allocate the fraction of the slot current used for torque or suspension forces and therefore enabling greater maximum torque or suspension forces; 2) reducing the number of winding layers to what is needed by the torque winding–this reduces manufacturing complexity and increases the winding packing factor; 3) potentially reducing copper losses–this has been shown in [99, 100] to be true for specific example designs. However, certain combinations of slots, poles, and phases do not work for DPNV designs and other combinations may yield unacceptably high force ripple or low force rating. Furthermore, in designs with constant radial forces, there is less value in being able to dynamically allocate slot current between the suspension and torque operation. The DPNV winding approach is most advantageous in designs with one or more of the following criteria: 1) the suspension forces are intermittent or variable, 2) the resulting DPNV suspension performance is similar or equivalent to what would be obtained with a conventional bearingless winding (i.e. the $Q = 6, p = 2$ entry in Table 6.7), 3) mechanical bearings are used and the suspension forces will provide vibration suppression.

6.7 Conclusion

DPNV windings use the same coils to produce both torque and radial suspension forces and thereby offer a solution to a major obstacle in the wider adaptation of bearingless motor technology: low torque density. This chapter significantly advances the state-of-the-art of DPNV winding technology by deriving the design requirements and proposing a generalized design approach which can also be used to transform existing motor designs into bearingless motors by simply modifying the end connections. Such modification comes at no extra machine cost, requires no redesign effort, and can be used to passively provide corrective forces with no additional drive circuitry.

Fractional-slot winding theory has been used to explore the DPNV winding concept and an FEA study was conducted to validate several example designs and contrast the resulting performance with conventional bearingless windings. It was shown that the

Table 6.7: Examples of separate suspension windings[a]

p	p_s	Q	q	y[b]	$\frac{k_{s,p_s}}{k_{t,p}}$	L[c]	$\frac{\langle F_x \rangle}{\text{Len}}$	% $\frac{\Delta F_x}{\langle F_x \rangle}$	% $\frac{\Delta F_y}{\langle F_x \rangle}$
$p \pm 1$ bearingless motors									
1	2	6	$\frac{1}{2}$	1	1	1	2.6	53	54
		6	$\frac{1}{2}$	1	1	2	2.8	44	45
2	1	6	1	3	1.155	1	5.1	16	14
		6	**1**	**1**	**0.577**	**2**	**2.7**	**15**	**15**
		18	3	9	1.015	1	5.1	4	4
4	5	**12**	$\boldsymbol{\frac{2}{5}}$	**1**	**0.966**	**1**	**1.6**	**10**	**6**
		12	$\boldsymbol{\frac{2}{5}}$	**1**	**1.077**	**2**	**1.8**	**5**	**4**
		36	$\frac{6}{5}$	-	0.997	1	1.7	3	3
		36	$\frac{6}{5}$	3	0.977	2	1.7	1	1
5	4	**12**	$\boldsymbol{\frac{1}{2}}$	**1**	**0.928**	**1**	**0.8**	**27**	**23**
		12	$\boldsymbol{\frac{1}{2}}$	**1**	**0.928**	**2**	**0.8**	**29**	**28**
		18	$\boldsymbol{\frac{3}{4}}$	-	1.286	1	1.2	8	9
		18	$\boldsymbol{\frac{3}{4}}$	**1**	**0.839**	**2**	**0.8**	**12**	**10**
4	1	36	$\frac{3}{2}$	18	0.991	1	4.7	3	3

---

[a] All of the information in this table pertains to the suspension winding; the torque windings are the same as those in Table 6.5.

[b] - is used for single layer windings which have coils with varying pitch

[c] Number of layers of the suspension winding.

benefits of DPNV windings vary on a per-design basis, with applications with intermittent force requirements seeing the greatest benefit. Finally, experimental validation is presented via a prototype machine in Chapter 8.

6.8 Fractional-slot winding theory

Relevant fractional slot winding information is provided in Table 6.8 and several standard terms are defined below. More detailed information can be found in textbooks such as [76].

6.8.1 Key terms

Base winding

smallest independent section of a winding. Symmetric windings consist repeated base windings.

First grade and second grade windings

defined based on the properties in Table 6.8. All symmetric windings can be classified as either first or second grade (integral-slot windings are considered first-grade since $n = 1$).

Normal phase machine

machine with $m \in \mathbb{N}_{\text{odd}}$.

Reduced phase machine

machine with $m \in \mathbb{N}_{\text{even}}$.

6.8.2 Useful relations

For the purposes of this chapter, it is useful to note that if a designer picks n, m, t, and z they will arrive at the number of poles and slots given by (6.22) and (6.23) for first

Table 6.8: Relevant fractional-slot winding information [76]

	First-grade	Second grade	
$\frac{Q'}{m}$	Even	Odd	
t	$\frac{p}{n}$	$\frac{2p}{n}$	
n	Odd	Even	
180° phasors?[a]	Yes	No	
		Single layer	Double layer
Q^*	Q'	$2Q'$	Q'
p^*	p'	$2p'$	p'

---

[a] whether the phasor star contains phasors in 180e pairs

grade windings

$$Q = 2mtz \tag{6.22}$$

$$p = nt \tag{6.23}$$

and (6.24) and (6.25) for second grade windings.

$$Q = mtz \tag{6.24}$$

$$p = \frac{nt}{2} \tag{6.25}$$

In single layer windings, the number of coils is

$$z_c = \frac{Q}{2} \tag{6.26}$$

and in double layer windings, the number of coils is

$$z_c = Q. \tag{6.27}$$

Chapter 7

Dual Purpose No Voltage Drives for Bearingless Motors

This chapter investigates the power electronic implementation of drives for bearingless motors with DPNV windings. The results are valid for conventional $p \pm 1$ pole-pair bearingless motors (i.e. bearingless permanent magnet and induction motors) and $p = 1$ bearingless motors (bearingless ac homopolar and consequent-pole motors). The advantages and disadvantages of each configuration are explored in terms of control complexity and required hardware; potential paths for circulating currents are identified along with mitigation strategies.[1]

7.1 Introduction

Literature on DPNV bearingless windings has focused on winding design and proof-of-concept prototypes. To date, there has been no detailed analysis on the use of power electronics to implement these drives. The primary contribution of this chapter is to investigate practical aspects of implementing bridge and parallel configurations of DPNV drives using two-level, three-phase and single-phase inverters. In this chapter, Section 7.2 provides an overview of the operation of the different types of bearingless motors considered; Section 7.3 introduces DPNV windings and the operation of bearingless

---

[1] Portions of the material in this chapter have also been published in [49].

motors with these windings; Section 7.4 proposes power electronic drive implementations for the two DPNV configurations and compares the hardware requirements with the conventional bearingless drive; Section 7.5 presents relevant considerations for controller design, including strategies for suppressing circulating currents; Section 7.6 uses simulation results to demonstrate the proposed control strategies and power electronic implementations; and experimental results to validate the parallel and bridge winding drive implementations for a bearingless ac homopolar motor are presented in Chapter 8.

7.2 Bearingless motor operation

Radial flux bearingless motors produce radial suspension forces by creating an unsymmetrical flux density in the airgap. The forces can be calculated via the Maxwell Stress Tensor, which for the idealized case of radial fields that do not vary with motor's axial length, can be written as (7.1),

$$\begin{aligned} F_x &= \frac{lr}{2\mu_0}\int_0^{2\pi} B_r\left(\alpha\right)^2 \cos\alpha \,\mathrm{d}\alpha \\ F_y &= \frac{lr}{2\mu_0}\int_0^{2\pi} B_r\left(\alpha\right)^2 \sin\alpha \,\mathrm{d}\alpha \end{aligned} \tag{7.1}$$

where l is the motor's active axial length, r is the airgap radius, and B_r is the cumulative radial flux density in the airgap at angular location α. From this expression, it can be shown that to create a radial force, the airgap flux density must contain components which differ in harmonic index by one. Force expressions and suspension operation are now summarized for the two types of radial flux bearingless motors. More detailed information can be found in [56]. Note that idealized current waveforms for force and torque production are presented later, in Section 7.3.

7.2.1 $p \pm 1$ bearingless motors

Conventional radial flux motors, i.e. permanent magnet (PM) or induction motors, have a radial airgap flux density given by (7.2), assuming that harmonics are neglected.

$$B_F\left(\alpha\right) = \hat{B}_F \cos\left(-p\alpha + \phi_F\right) \tag{7.2}$$

Here, p represents the number of pole-pairs of the motor and ϕ_F indicates the angular location of the magnetic field at an instant of time. The magnetic field is composed of a magnetizing field (for example, produced by PM's or a rotor winding) and armature reaction field. To transform this type of motor into a bearingless motor, a suspension winding with either $p+1$ or $p-1$ pole-pairs is added to the stator to produce a radial flux density which differs in harmonic index by one (7.3). This flux denisty is produced by balanced sinusoidal suspension currents (7.4).

$$B_s(\alpha) = \hat{B}_s \cos\left(-\left[p \pm 1\right]\alpha + \phi_s\right) \tag{7.3}$$

$$\begin{aligned} i'_u &= \hat{I}_s \cos\left(\phi_s\right) \\ i'_v &= \hat{I}_s \cos\left(\phi_s - \tfrac{2\pi}{3}\right) \\ i'_w &= \hat{I}_s \cos\left(\phi_s + \tfrac{2\pi}{3}\right) \end{aligned} \tag{7.4}$$

These currents can be transformed into an equivalent two-phase system using the well-known DQ transformation. If this is done with respect to the angle ϕ_F, convenient constant expressions for the radial force result (7.5), where i_x and i_y are the two-phase DQ currents from the transformation.

$$\begin{aligned} F_x &= k_f i_x \\ F_y &= k_f i_y \end{aligned} \tag{7.5}$$

Typically, a suspension controller specifies required values of F_x and F_y, which are then used to determine the phase currents via an inverse DQ transformation (7.6). Noting that ϕ_F increases at the speed of the armature winding frequency, it can be seen that to produce a constant force, the suspension currents will have the same frequency as the armature currents.

$$\begin{Bmatrix} i'_u \\ i'_v \\ i'_w \end{Bmatrix} = \frac{\sqrt{2/3}}{k_f} \begin{bmatrix} \cos\phi_F & -\sin\phi_F \\ \cos\left(\phi_F - \frac{2\pi}{3}\right) & -\sin\left(\phi_F - \frac{2\pi}{3}\right) \\ \cos\left(\phi_F + \frac{2\pi}{3}\right) & -\sin\left(\phi_F + \frac{2\pi}{3}\right) \end{bmatrix} \begin{Bmatrix} F_x \\ F_y \end{Bmatrix} \tag{7.6}$$

7.2.2 $p = 1$ bearingless motors

This class includes the ac homopolar and consequent-pole bearingless motors. These motors can be viewed as having a constant radial airgap flux density component which does not vary with the angular position (7.7).

$$B_{F0}(\alpha) = \hat{B}_{F0} \tag{7.7}$$

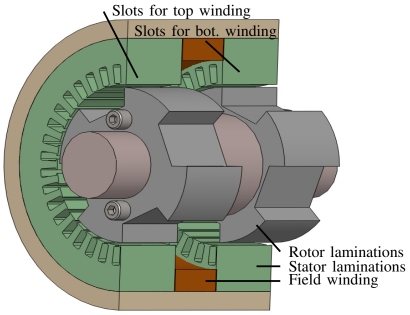

Figure 7.1: The bearingless ac homopolar motor

Radial forces are produced by adding a $p = 1$ pole-pair suspension winding to the stator, which produces a flux density given by (7.8) with suspension currents as previously defined (7.4).

$$B_s(\alpha) = \hat{B}_s \cos(-\alpha + \phi_s) \tag{7.8}$$

A DQ transformation, this time with $\phi_F = 0$, can again be used to transform the suspension currents into equivalent x-y currents and obtain simple force expressions (7.5). The same inverse transformation is used to calculate the suspension phase currents (7.6), again with $\phi_F = 0$. Since $\phi_F = 0$, it can be seen that to produce a constant force the suspension currents will be DC. Furthermore, no information regarding the airgap flux density's location is needed for suspension force creation, which is viewed as an advantage of this type of bearingless motor. It should noted that for the consequent-pole and ac homopolar motors, this requires a $p \geq 4$ pole-pair motor.

The bearingless ac homopolar motor has two airgaps, each of which is able to produce radial forces. As indicated in Fig. 7.1, a separate suspension winding is wound around the top and bottom rotor/stator sections and (7.5) is written separately for each airgap. Therefore, the bearingless ac homopolar motor has four degrees of freedom.

7.3 DPNV winding operation

Traditional bearingless motors have two separate stator windings, each with its own set of coils: an armature winding (for torque production) and a suspension winding (for radial force production). In contrast, a DPNV winding is a single winding which uses

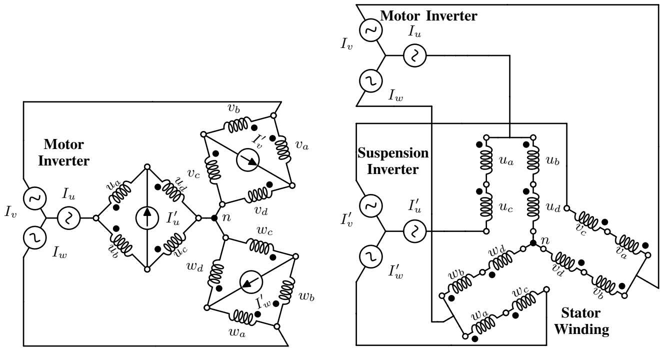

(a) Bridge Configuration (b) Parallel Configuration

Figure 7.2: Schematics for the two configurations of dual-purpose windings for bearingless motors with one airgap.

the same set of coils for both torque production and radial force production. DPNV windings have two sets of terminals connections: one for torque-producing current and one for radial-force producing suspension current. While these terminals connect to the same coils, the coil direction is reversed for half of the coils from the perspective of the suspension terminals.

A schematic depicting the bridge and parallel DPNV drive connections is shown in Fig. 7.2 for a machine with four coil groups in each phase (*a*-*d*). The inductor symbols represent each coil group, which can be modeled as a resistance and leakage inductance in series with a voltage source, Fig. 7.4. The voltage source is the result of a coupled inductance of the coil group with all other coil groups in the winding and a permanent magnet or field winding. The machine is designed so that the voltage sources in groups *a* and *b* of a particular phase are identical; the same is true for groups *c* and *d*. By doing this and noting the coil group directions, it can be seen that the voltage sources cancel out at the suspension terminals of both the bridge (Fig. 7.2a) and parallel configuration (Fig. 7.2b). The bearingless ac homopolar machine has two airgaps and therefore two DPNV windings. In practice, the motional-EMF of the two sections may be slightly mismatched, causing circulating currents if the stator torque terminals were connected in parallel. To avoid these currents, the separated parallel connection and series bridge connection depicted in Fig. 7.3 are proposed.

The terminal currents used to generate radial force and torque are shown in Fig. 7.5

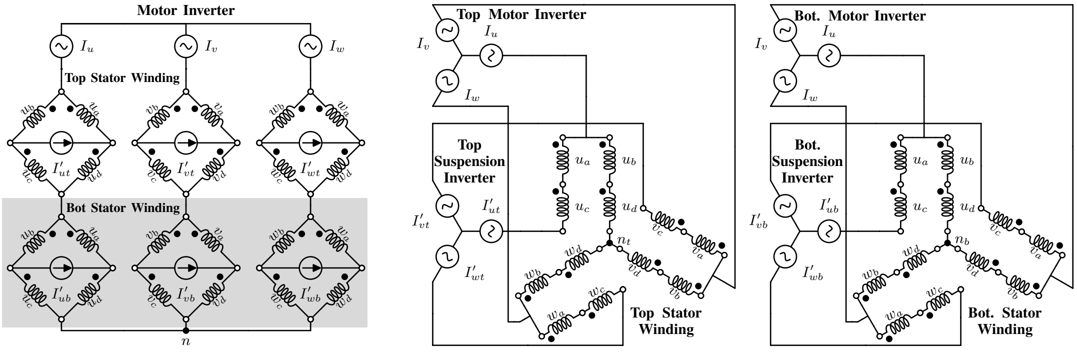

(a) Bridge Configuration

(b) Parallel Configuration

Figure 7.3: Schematics of the two DPNV configurations applied to the bearingless ac homopolar motor.

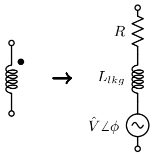

Figure 7.4: Coil group model

for the two types of bearingless motors connected in both parallel and bridge configurations. In the parallel configuration, the suspension current terminals carry half of the torque terminal current in addition to the required force-producing suspension current. This is in contrast to the bridge suspension terminals, which only carries force-producing current. The parallel configuration has a series connection to all of the coils, whereas the bridge configuration has a parallel current path to the coils, meaning that the parallel suspension terminals only carry half the force-producing current of the bridge suspension terminals. Differences in required current waveforms between the two types of bearingless motors are also readily apparent, matching the discussion in Section 7.2. Note that the shape of the terminal currents in the bridge configuration is the same as the terminal currents for a conventional bearingless winding, which has separate armature and suspension windings.

The current of each coil group is a superposition of the suspension and torque terminal currents. Based on the amount of suspension current required, the drive must

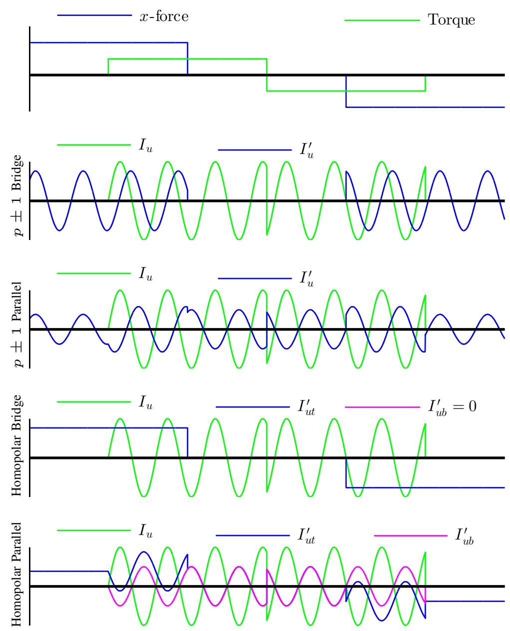

Figure 7.5: Current waveforms for producing the indicated force and torque. The waveforms for the consequent-pole motor are the same as those indicated for the bearingless ac homopolar motor, except that I'_{ub} does not exist since the bearingless consequent-pole motor has only one airgap. For the ac homopolar motor, the x-force shown in the top plot is used as the top airgap x-force and the bottom airgap x-force is zero. In all cases, the y-force is zero.

actively limit the maximum allowable torque current so as to avoid exceeding the current rating in any coil group. This is different from a conventional bearingless winding, where separate coils carry torque and suspension current and the maximum torque current (and therefore torque capability) is permanently fixed. For this reason, the DPNV winding designs are highly advantageous in applications where the amount of required suspension current varies significantly during operation; here, a machine with a DPNV winding is able to carry a greater torque producing current (and therefore create more torque) during operating times when low-suspension current is required.

Examples of $p \pm 1$ bearingless motors with DPNV windings can be found in [99, 105, 109, 111, 112], and an example of a DPNV winding design for the bearingless ac homopolar motor can be found in [47].

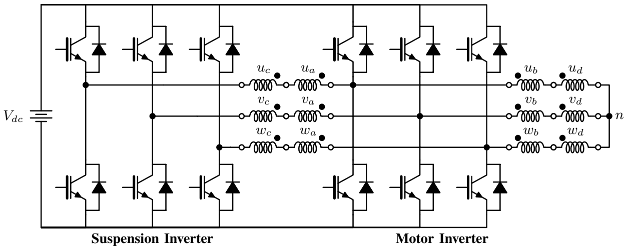

(a) Parallel configuration using a common DC bus

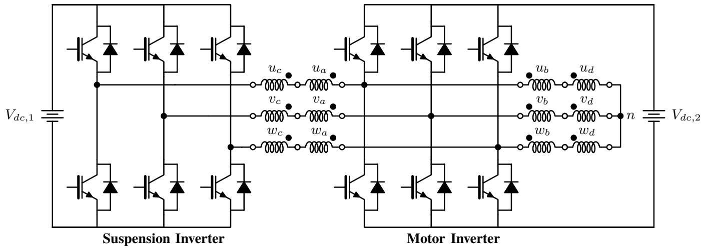

(b) Parallel configuration using isolated DC buses

Figure 7.6: Circuit diagrams of the power electronics converters proposed to realize the DPNV parallel drive.

7.4 Power electronic implementation

Power electronic implementations of the parallel and bridge DPNV drive configurations are now proposed using single- and three-phase, two-level inverters. These configurations are contrasted against the traditional bearingless winding implementation, for which the complete drive is composed of standard three-phase motor drives attached to each winding; that is, separate three-phase, two level inverters attached to the suspension and torque windings which share a common voltage bus. The results of the discussion are summarized in Table 7.1. Note that the conventional bearingless winding for the ac homopolar motor has one torque winding which spans the entire motor length and separate suspension windings spanning each airgap. This requires one three-phase inverter for the torque winding and two three-phase inverters for the suspension windings.

Table 7.1: Comparison of power electronic implementations

	Bridge		Parallel		Parallel isolated		Conventional	
Number of airgaps[a]	One	Homopolar	One	Homopolar	One	Homopolar	One	Homopolar
Switches	18	30	12	24	12	24	12	18
Current sensors	5	8	5	10	4	8	4	6
Isolated voltage buses	4	7	1	1	2	2	1	1
Usable sus. v. bus[b]	1		$\frac{1}{2}$		$\frac{1}{\sqrt{3}}$		$\frac{1}{\sqrt{3}}$	
Usable torque v. bus[c]	$\frac{1}{\sqrt{3}}$		$\frac{1}{2}$		$\frac{1}{\sqrt{3}}$		$\frac{1}{\sqrt{3}}$	
Sus. inverter current rating	2× coil rating		coil rating		coil rating		coil rating	
Sus. inverter voltage rating	$\leq$ torque inverter		torque inverter		$\leq$ torque inverter		$\leq$ torque inverter	

---

[a] "One" corresponds to a $p \pm 1$ or consequent pole machine, "Homopolar" corresponds to the ac homopolar machine

[b] Usable fraction of sus. voltage bus

[c] Usable fraction of torque voltage bus

7.4.1 Parallel configuration

The parallel DPNV drive can be implemented using three-phase, two-level inverters sharing a common voltage bus, as shown in Fig. 7.6a. For the bearingless consequent-pole and $p \pm 1$ pole-pair motors, this requires 12 switches. For the bearingless ac homopolar motor, two sets of these inverter pairs are required, one for the top airgap and one for the bottom airgap, requiring 24 switches. Care must be taken to avoid circulating currents between the two inverters in each set. There are two primary factors that can lead to significant circulating currents:

1) instantaneous mismatch between the applied common mode voltages at the terminals of each inverter;

2) unbalanced phase impedances or the unexpected presence of a small voltage at the suspension terminals.

Item 1) prevents the use of modulation schemes that apply different common mode voltage when averaged over a switching period, such as the widely used Conventional Space Vector Pulse Width Modulation (CSVPWM) which allows output phase voltages as large as $\frac{V_{dc}}{\sqrt{3}}$ [113]. The Sine Triangle Comparator PWM method can be used, as it applies a constant common mode voltage, but this limits the output phase voltage to $\frac{V_{dc}}{2}$ [113]. Since slight asymmetries in the phase impedance are inevitable and slight variations from the "no voltage" property of the suspension winding may arise, item 2) requires that five current sensors be used for each set of inverters so that circulating currents can be detected and actively removed.

Alternatively, the two inverters of each set can be operated from isolated dc buses to eliminate all concern of circulating currents, shown in Fig. 7.6b. In this configuration, CSVPWM can be used and only four current sensors are required for each two inverter set (two current sensors for each three-phase inverter). The suspension inverter voltage bus can now have a different value than the torque inverter bus. This is a useful feature because the "no voltage" property of the suspension terminals means that the suspension inverter can utilize a lower voltage bus than the torque inverter in most designs; using a lower bus voltage (for the same output current) results in lower suspension inverter losses and enables the suspension inverter to use less expensive switches that have lower voltage blocking capability. For the bearingless ac homopolar motor, the same dc buses can be reused in the second inverter set because there is no path for circulating currents between the top and bottom windings; this means a single voltage source can be used for $V_{dc,1}$ of Fig 7.6b between the top and bottom inverter set, and a single voltage source can be used for $V_{dc,2}$ between the top and bottom inverter set. Note that providing isolated dc buses for this configuration has the significant downside of requiring additional hardware.

Fault tolerance is a concern in either realization of the parallel implementation. This suspension controller operation is dependent upon valid operation of the torque inverter, which increases the number of components for which a failure could result in unstable operation.

7.4.2 Bridge configuration

The bridge DPNV configuration can be implemented by using a three-phase, two-level inverter for the motor inverter and isolated H-Bridges for each suspension phase, see Fig. 7.7. For the bearingless consequent-pole and $p \pm 1$ pole-pair motors, this requires 18 switches; for the bearingless ac homopolar motor, this requires 30 switches. A current sensor must be used on each phase of the suspension terminal connection and on two of the phases of the torque terminal connections. This translates to requiring five current sensors for the machines with a single airgap and eight current sensors for the bearingless ac homopolar motor. Furthermore, each converter must use a dc bus isolated from all other converters. It is therefore concluded that the bridge configuration requires substantially more hardware than the parallel configuration.

The bridge configuration also has advantages over the parallel configuration. The only risk of circulating currents in this configuration is in the suspension phases, since voltages are applied to each phase independently from the other phases. The three phase torque inverter can use CSVPWM to obtain a higher output voltage ($\frac{V_{dc}}{\sqrt{3}}$), and the individual H-Bridges are able to apply the full bus voltage as their phase voltage. The H-Bridge converters have to carry twice the suspension current, but none of the torque current, meaning that in designs were the suspension current is normally low, they will have less losses in the suspension inverter. Furthermore, because the H-Bridge converters are on isolated voltage buses, they can have a lower bus voltage than

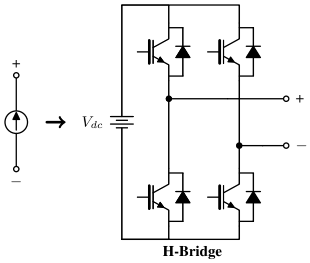

Figure 7.7: Implementation of bridge suspension inverter

the torque inverter; this has the same advantages that were described for the isolated implementation of the parallel drive.

In terms of fault redundancy, the bridge configuration is also at an advantage. Since the torque inverter is completely isolated from the suspension inverter, a failure in the torque inverter circuit or current sensor, would not impact the suspension operation. Furthermore, utilizing isolated voltage buses for each of the H-Bridges provides more redundancy, since a shorted-inverter would only disrupt a single suspension phase and it is possible to provide $x - y$ forces with two of the three phases.

7.5 Control considerations

The typical control system for a bearingless motor drive is illustrated in Fig. 7.8a. This same implementation can be used for a bridge configured bearingless drive. In the parallel configuration, the suspension terminals carry half of the torque current, which must be added to the suspension current references; this is shown in Fig. 7.8b. The blocks labeled as “PI-based motor/suspension current controller” correspond to the vector control approach taken in motor drives [72]. The operation of the blocks labeled as “Deterimine k_f and ϕ_f” and “Determine suspension currents” correspond to the discussion in Section 7.2, primarily (7.5); in the case of a $p = 1$ bearingless motor, k_f is a constant and $\phi_f = 0$ which significantly simplifies these blocks. The blocks labeled as “Convert UVW to DQ0” and “Convert DQ0 to UVW” correspond to DQ and inverse-DQ transformations, respectively. The “PWM” blocks represent the interface to the power electronics and the type of pulse width modulation used, which was described in Section 7.4. For the bridge configuration suspension terminals, this corresponds to the

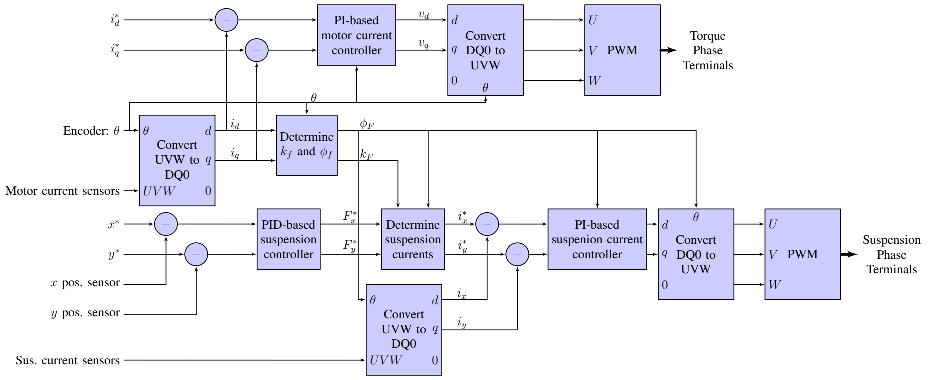

(a) Control schematic for a conventional bearingless drive and the bridge DPNV drive

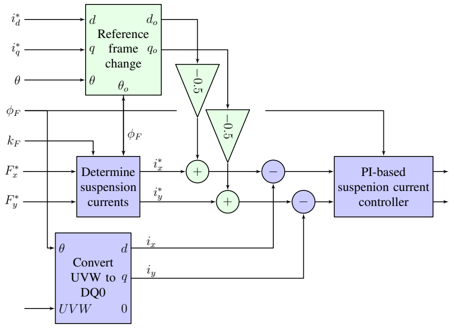

(b) Additional components for parallel DPNV drive

Figure 7.8: Schematic of the control diagram for a bearingless motor; the green components in (b) indicate the additional logic required for a parallel DPNV drive.

H-Bridges of Fig. 7.7; otherwise this corresponds to a three-phase, two-level inverter.

As described in Section 7.3, the DPNV suspension terminals can be modeled as a constant series resistance and inductance. As is standard for vector control, the suspension current controllers are designed in the DQ domain. The suspension DQ transformation is based on the angle ϕ_F, which results in the voltage equations below (7.9). Referring to Fig. 7.4, the bridge configuration has $R_{\text{sus}} = R$ and $L_{\text{sus}} = L_{lkg}$; the parallel configuration has $R_{\text{sus}} = 4R$ and $L_{\text{sus}} = 4L_{lkg}$.

$$\begin{aligned} v_x &= R_{\text{sus}} i_x + L_{\text{sus}} \dot{i}_x - \dot{\phi}_F L_{\text{sus}} i_y \\ v_y &= R_{\text{sus}} i_y + L_{\text{sus}} \dot{i}_y + \dot{\phi}_F L_{\text{sus}} i_x \end{aligned} \tag{7.9}$$

As discussed in Section 7.4, the implementation of the bridge configuration and the non-isolated implantation of the parallel configuration can experience zero-sequence, or circulating, currents which enter at the suspension terminals. A PI controller with a zero reference can be used to suppress these currents, as shown in Fig. 7.9. The zero sequence voltage equation can be extracted from the suspension DQ transformation, shown in (7.10).

$$v_0 = R_{\text{sus}} i_0 + L_{\text{sus}} \dot{i}_0 \tag{7.10}$$

In the parallel DPNV drive configuration for the $p = 1$ bearingless motors, additional control issues can arise due to the suspension DQ reference frame being stationary and the torque DQ reference frame rotating at the synchronous frequency. This problem can become apparent when constant radial forces are present, which require DC suspension currents. To the torque DQ current controller, these DC suspension currents appear to be rotating backwards at the synchronous frequency. Since PI controllers have difficulty tracking sinusoidal signals, these currents can cause oscillating errors to appear in the DQ motor currents. This issue also arises in other applications, such as active filters and motor drives [114–117]. One solution to this problem is to add additional integrators to the error signals in a reference frame where the problem signal is DC [115, 117]. For the present problem with parallel DPNV drives for homopolar motors, this means having an additional stationary DQ reference frame for the motor DQ currents, integrating the error as seen in this reference frame, and adding the resulting voltage references to the voltage references generated by the primary motor current controller. The details of implementing such a scheme are reserved for a future work.

7.6 Simulation results

MATLAB Simulink was used to validate the proposed implementations of the parallel and bridge configured drives for both the $p \pm 1$ and $p = 1$ bearingless motors. Each configuration was simulated with closed loop control, using idealized MOSFET models, and a switching frequency of 20kHz. The parallel configuration was implemented with a common dc bus, corresponding to Fig. 7.6a. In all simulations, the reference torque and x-direction suspension force waveforms shown in Fig. 7.10 are used and k_f is assumed to be a constant (i.e. is not impacted by q-axis current). The simulated bearingless motors have eight poles and a constant rotational speed of 1000RPM. Fig. 7.11 shows resulting simulated current waveforms. The power electronics work as expected under these idealized conditions.

Next, to illustrate the necessity of zero sequence current control, a phase imbalance was introduced in series with the suspension current terminals. Models with and without the zero sequence current controllers described in Section 7.5 were then simulated, with the results shown in Fig. 7.12. The plotted zero sequence currents were calculated from (7.11) by measuring the current into the suspension phase terminals. In the parallel configuration, the phase imbalance also appears in a portion of the torque current path, which causes unbalanced torque currents in addition to unbalanced suspension currents. In both the bridge and the parallel configuration, the simple zero sequence controller described in Section 7.5 is able to suppress the circulating current.

$$i_0 = \frac{1}{3}\left(I'_{ut} + I'_{vt} + I'_{wt}\right) \tag{7.11}$$

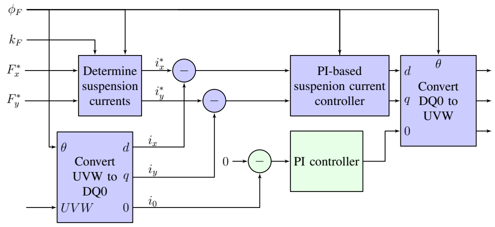

Figure 7.9: Additional components for zero sequence current control

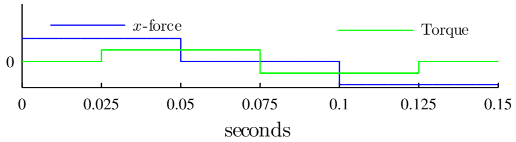

Figure 7.10: Simulation reference waveforms

7.7 Conclusion

This chapter investigated the power electronics used to implement drives for machines with DPNV windings. A comparison between the hardware requirements of the parallel and bridge DPNV drives and the conventional bearingless drive was presented as well as simulation results. Hardware results are presented later, in Chapter 8.

It was shown in the chapter that there are advantages and disadvantages to each of the DPNV drive configurations. The parallel configuration requires the least hardware components, but has less fault tolerance and more complex control requirements due to potential interactions between the torque and suspension inverters. Neither configuration can be realized in as few components as a standard bearingless motor drive, meaning that the DPNV drives will have a higher cost. This must be weighed against the potential increase in bearingless machine performance when deciding whether to design a bearingless motor with a DPNV winding.

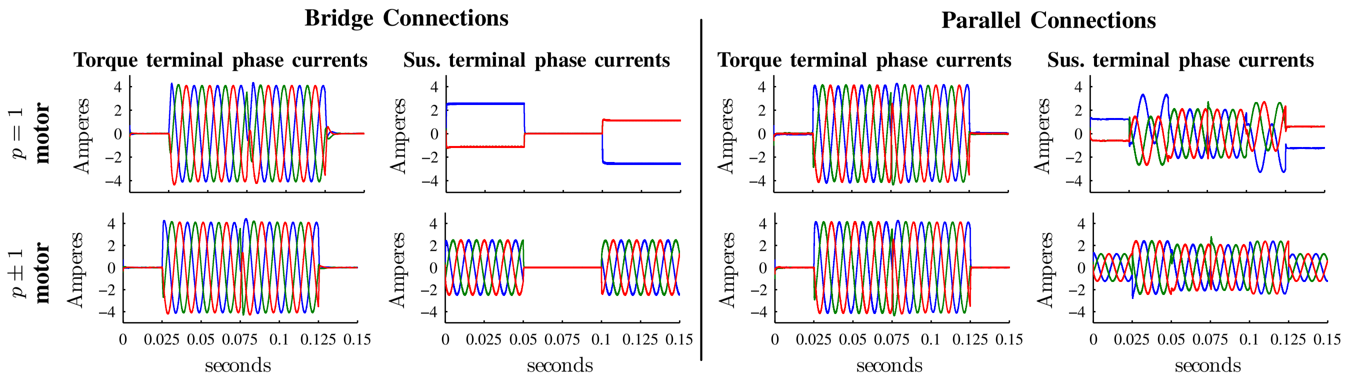

Figure 7.11: Simulation results for the proposed implementations of the bridge and parallel DPNV drives; both a $p = 1$ motor and a $p \pm 1$ motor are considered.

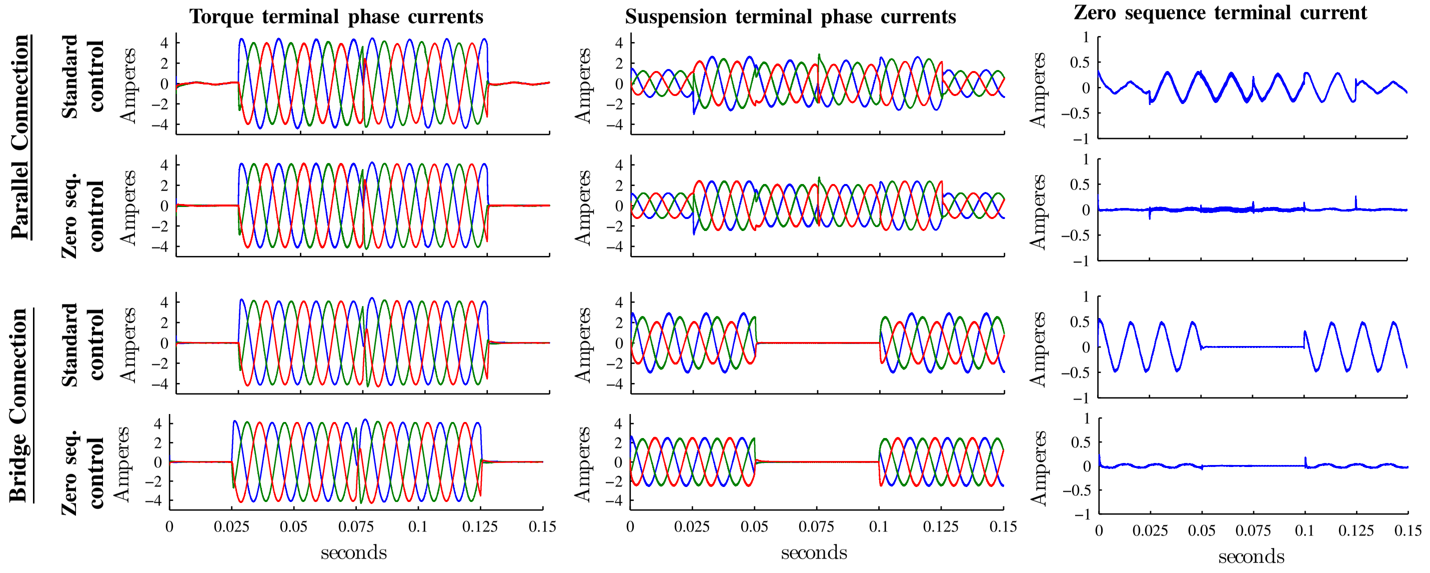

Figure 7.12: Simulation of zero sequence current controllers in the parallel and bridge configured drives for a $p \pm 1$ bearingless motor; a phase imbalance has been introduced by the addition of a series R-L branch at the suspension terminals of phases v and w; phase v has 1.5× the suspension impedance of phase u and phase w has 2× the suspension impedance of phase u.

Chapter 8

Bearingless Prototype Design and Experimental Results

8.1 Introduction

The design of various components of the prototype bearingless ac homopolar machine and the drive system used to operate it are now described. Experimental results are presented in this chapter to characterize the machine and validate the concepts developed in previous chapters.

The final prototype machine is shown in Fig. 8.1, the power electronics are shown in Fig. 8.2, and the control hardware is shown in Fig. 8.3. The power electronic inverters use silicon carbide (SiC) MOSFETs so that they can operate at a high switching frequency. This enables faster control operation and bandwidth and ultimately better machine performance than would be possible with the switching frequencies achievable with IGBTs. The design and characterization of the individual half-bridge circuits that are connected to make up these inverters has been published in [118].

Despite the dissertation's interest in developing an outer-rotor bearingless ac homopolar motor for flywheel energy storage, an inner-rotor topology has been used. This was done for ease of testing, as inner-rotor machines are standard and existing products were more easily purchased to construct the test stand. The concepts developed in this dissertation apply to both the inner- and outer-rotor topologies and the purpose of this prototype is to simply validate these concepts. The ac homopolar machine geometry is

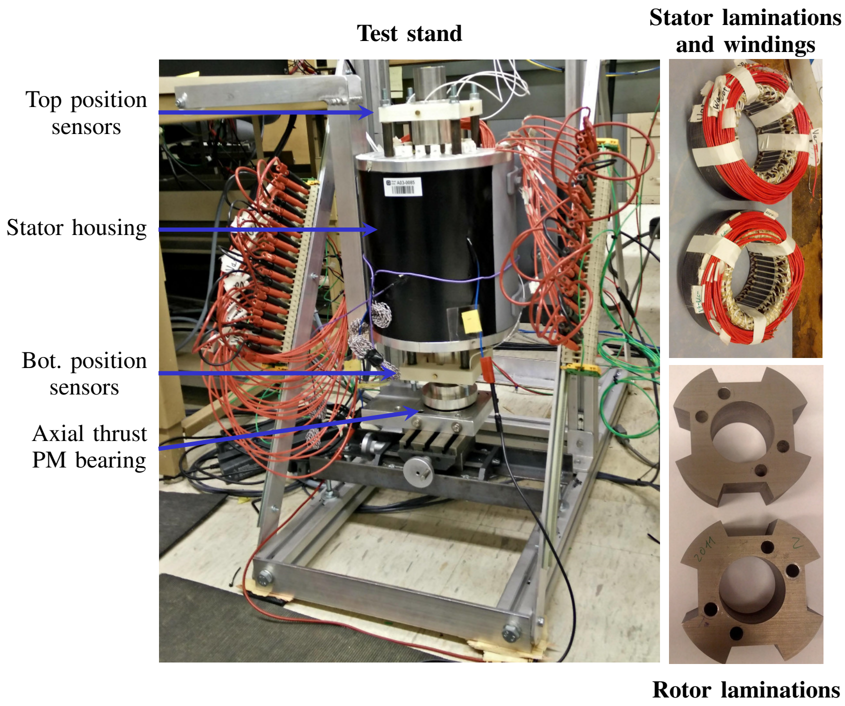

Figure 8.1: The prototype bearingless ac homopolar machine

the same as was illustrated in Fig. 2.1a. An axial PM thrust bearing is used to support the rotor weight, the design and characterization of which is described in Section 8.2. A DPNV winding has been installed in the two stator stacks, so that the same coils can be used for both torque and suspension forces. The design of this and a general FEA study of the machine is presented in Section 8.3. The controller design and control hardware implementation is described in Section 8.4. Finally, the hardware results of the prototype machine performance are presented in Section 8.5.

8.2 Axial PM bearing design

The design of the axial PM bearing used in the prototype machine is now described. The PM bearing was characterized via an experimental setup to understand the radial and axial stiffness as a function of rotor eccentricity. A point of emphasis is made on designing a bearing that maintains acceptable radial and axial stiffness values, and then measuring these values, when the bearingless machine is powered down and its rotor is

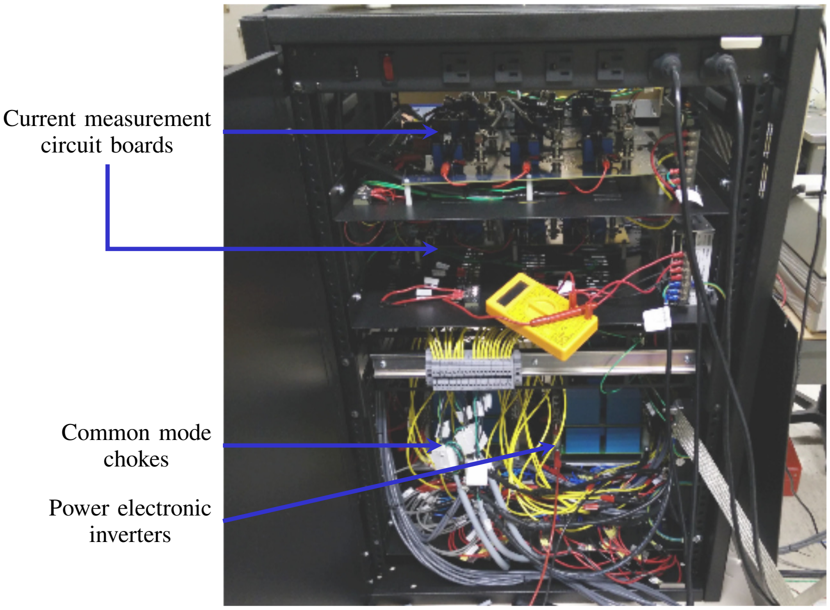

(a) Power electronics cabinet

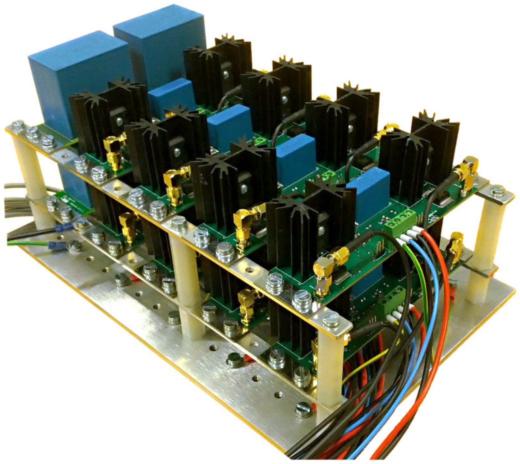

(b) SiC-based Inverter

Figure 8.2: The power electronic drive

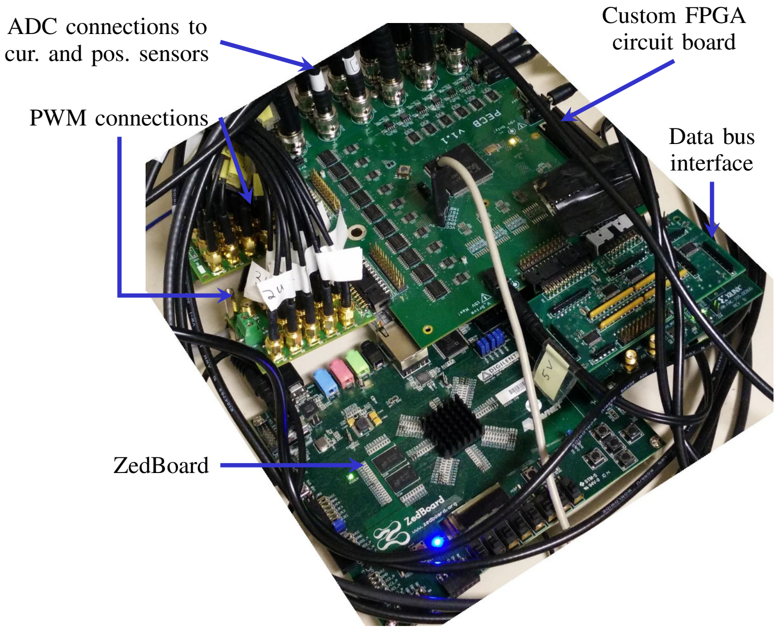

Figure 8.3: The drive control hardware

highly eccentric. A literature review of bearing characterization techniques is presented along with a description of the characterization procedure used and the characterization results.[1]

8.2.1 Design

The axial bearing design is based around a simple repulsive ring bearing, as depicted in Fig. 8.4. The design was conducted using FEA, with the design goals of minimizing the radial unstabilizing forces and changes in the axial forces when the rotor is fully eccentric (resting upon its touchdown bearings) and minimizing the design cost by reducing the magnet volume. The bearing stator consists of an axially magnetized ring magnet glued to an aluminum yoke; the rotor consists of an axially magnetized ring magnet glued to an aluminum sleeve which is secured to the bottom of the bearingless motor's rotor shaft.

The bearing design space is explored through 2D and 3D FE simulations in Fig. 8.5. The rotor weight, desired airgap, and magnet material properties are design constants

---

[1] Portions of this material have also been published in [53].

Table 8.1: Magnetic bearing design

Magnet thickness	3.4 mm
Inner diameter	55 mm
Outer diameter	82 mm
Magnet material	NdFeB Grade N42
Remanent flux density	1.28 T
Coercivity	915 kA/m

and the magnet thickness and inner diameter are design variables. To design the bearing, 2D FEA was performed for different values of the design variables to find the required magnet outer diameter needed to support the rotor weight with the desired airgap. The magnet volume was then calculated from the dimensions and 3D FEA was used to determine the radial unstabilizing force and changes in the axial supporting force when the bearing is fully eccentric (that is, when the bearingless motor's rotor is resting on the touchdown bearings). The final design is specified in Table 8.1 and additional FE results are presented later, in Fig. 8.9.

8.2.2 Review of bearing characterization techniques

Many different approaches to measuring the radial and axial forces can be found in the literature, for example: [119–130]. However, little emphasis is placed on either making accurate measurements during simultaneous axial and radial displacement or when the bearing is highly eccentric (corresponding to the case where the bearingless motor is powered down). On a fundamental level, these measurement approaches can be summarized as variations of the following:

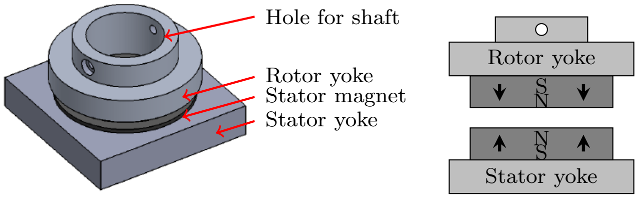

Figure 8.4: Axial PM repulsion bearing

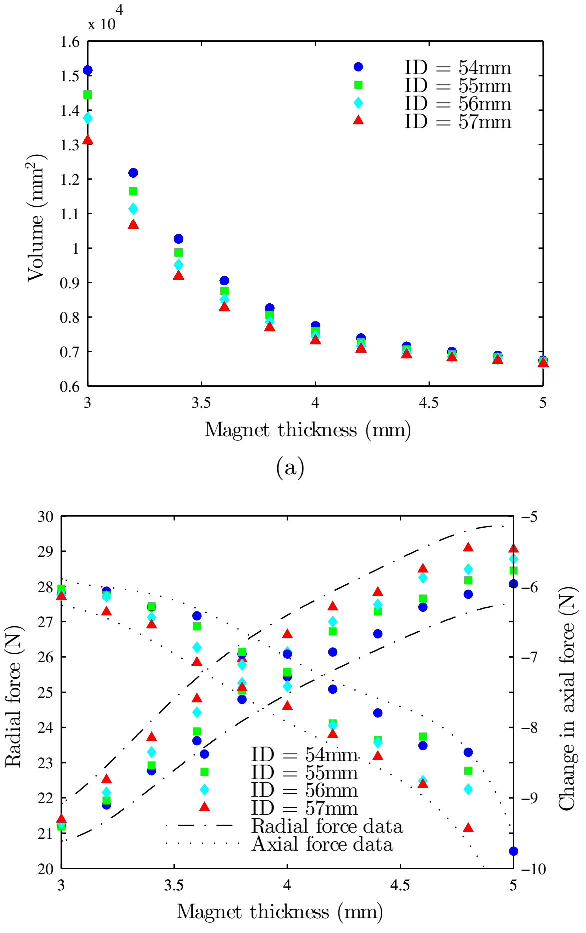

(a)

(b)

Figure 8.5: 2D and 3D FEM results showing the effect of magnetic thickness and inner diameter on: (a) required magnet volume; (b) magnetic bearing radial and axial forces when the rotor is resting on its touch down bearings ($\delta = 1.5$ mm).

- the rotor and stator are somehow mechanically displaced from each other and a device (such as a load cell) is used to measure the force along that direction for various displacements [119–121, 125, 128–130];
- a known force (i.e. a weight) is applied to the rotor along an axis and the displacement is measured for various forces; this will only work in cases where the magnetic bearing is stable in the displacement direction [119, 123, 125, 130].

There are also several different approaches to measuring the radial/axial stiffness, most of which can be summarized as variations of the following:

- extract the stiffness from the force data by fitting a linear regression line to the data as a function of displacement for small displacements [119, 120, 122, 125, 128, 130];
- excite the rotor with an impact hammer and observe the rotor's frequency response [122, 129].

A common variation on the above techniques is used in [122] for measuring radial stiffness (axial stiffness is measured via the impact hammer test). Here, a consequent-pole bearingless motor is considered with a PM axial bearing. To measure the radial stiffness, the bearingless motor suspension force characteristic is first measured: k_f of the linearized magnetic bearing force model (8.1) is calculated by using the magnetic bearing controller to keep the rotor centered (fixing $\delta = 0$ mm), applying a radial force to the rotor, and measuring the required suspension current, i_s.

$$F(\delta, i_s) = -k_s \delta + k_f i_s \tag{8.1}$$

Next, the controller is used to displace the rotor radially to a small value of δ. When the rotor is in equilibrium, $F(\delta, i_s) = 0$ and the radial stiffness is measured: $k_s = k_f i_s / \delta$ with and without the PM bearing connected. While this is a very low-cost approach, there are two potential problems that must be carefully addressed on a per-device basis to ensure accurate results:

- the force model of (8.1) is typically only a linear approximation of the radial force's dependence on displacement; it is therefore only accurate for sufficiently small values of δ and it doesn't account for axial displacement;

- as is noted in [58], the radial suspension force of the bearingless motor can vary to a limited extent as a function of the rotor's angular position, so if the rotor were to rotate between the time that the suspension force was characterized and the stiffness was measured, inaccurate results would be obtained.

Another variation is used in [130]. Here, the machine's rotor is displaced to several small values of δ by the controller. For each value, radial forces are applied to the rotor and the suspension current is measured while the controller keeps the displacement fixed. The bearing stiffness is approximated by dividing the difference in applied force for a given suspension current at two different displacements by the difference in displacement. Again, this suffers from the same potential inaccuracies as mentioned before. However, it is found that the method is sufficiently accurate for the device being considered in [130] under very small displacements.

Neither of the aforementioned variations are likely to provide acceptable radial stiffness measurements for large displacements in either the radial or axial direction and therefore are unlikely to accurately characterize the PM bearing when the bearingless machine is powered down and the rotor is fully displaced. In [120], a force measurement procedure is described which should be capable of accurately measuring radial/axial forces as a function of both radial and axial displacement. Here, the stator is connected to a load cell capable of measuring forces in three dimensions. An automated 3D x-y-z cross-table is used to move the stator and rotor with respect to each other. While radial and axial force results are only reported for displacements along their respective axes, it appears that this setup could be used to accurately measure forces along both axes. However, such equipment was not available and is considerably more expensive than the equipment required for the measurement which was used.

8.2.3 Measurement technique used

To characterize the PM bearing, the test stand depicted in Fig. 8.6 and Fig. 8.7 was built. The rotor is fixed radially but is free to move axially. This is accomplished by mounting two brass sliding bearings on the housing of the bearingless motor. The PM bearing stator is restricted axially and movements in the radial direction are controlled by a manual x-y cross-table. The connection to the cross-table is through single-axis

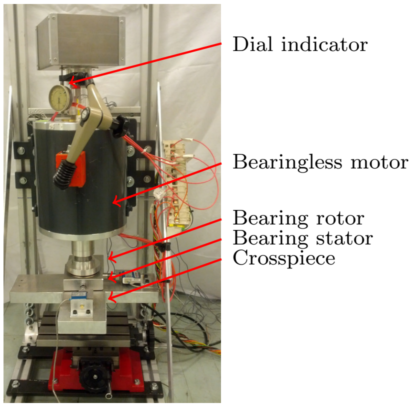

(a) Full test stand

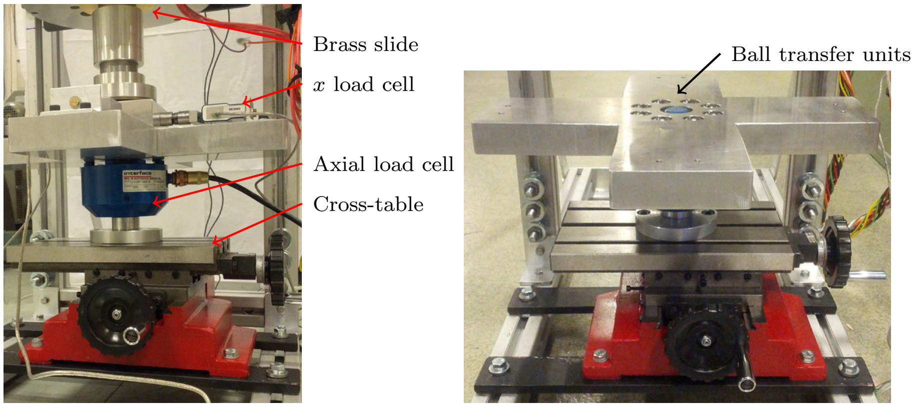

(b) Measurement apparatus

(c) Test stand bottom

Figure 8.6: Photographs of (a) the full test stand; (b) the measurement apparatus; and (c) the bottom of the test stand with the PM bearing and radial load cells removed.

load cells. An "x" and a "y" load cell are each connected to a side of the bearing stator through universal joint linkages. The universal joint linkages are used instead of bolts to decrease any cross-talk between the sensors, as they only support forces along their axes. The PM bearing stator rests axially against eight ball transfer units which have been installed in the crosspiece and are shown in Fig. 8.6c. The ball transfer units prevent friction between the bearing stator and the crosspiece that could interfere with radial force measurement. The radial force sensors are also mounted to this crosspiece and the entire apparatus is centered on top of another single-axis load cell for axial force measurements.

The rotor can be displaced axially by placing weights upon it (see the basket on

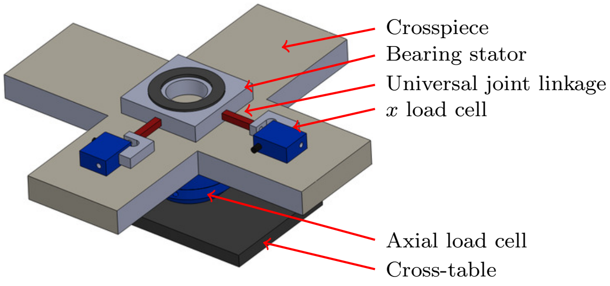

Figure 8.7: Drawing of measurement apparatus

the top of Fig. 8.6a) while the stator can be displaced radially by adjusting the x-y cross-table. Since the brass sliding bearings have some axial friction, the value of the weights added to the top of the rotor are ignored and instead the axial load cell is used to measure the axial force that the bearing provides. The rotor's axial displacement is measured via a dial indicator while the x-y cross-table is able to accurately position the stator to within 0.025 mm.

All measurements are taken with the bearingless homopolar machine completely powered down.

8.2.4 Results

Radial and axial force measurements are shown in Fig. 8.8 and 8.9. The airgap between the PM bearing and stator was measured at being 2.55 mm nominally, which, as can be seen in Fig. 8.8a, matches the FE simulations. The radial and axial stiffness values about the nominal positions were calculated from linear regression lines fit to the data and shown in Fig. 8.8a and 8.8b. These stiffness values are given in Table 8.2. Note that the measured radial stiffness value is approximately 4% greater than the FEA calculation and the measured axial stiffness is approximately 3% greater than the FEA calculation. Earnshaw's theorem predicts that for an axially symmetric magnetic bearing without iron, the axial stiffness should be twice the radial stiffness [131, 132]. The FE results satisfy this exactly and the small discrepancy in the measured results can be explained by measurement uncertainty, as discussed later.

The radial and axial force measurements as a function of both radial and axial displacement are shown in Fig. 8.9a and 8.9b. The range of radial displacement is

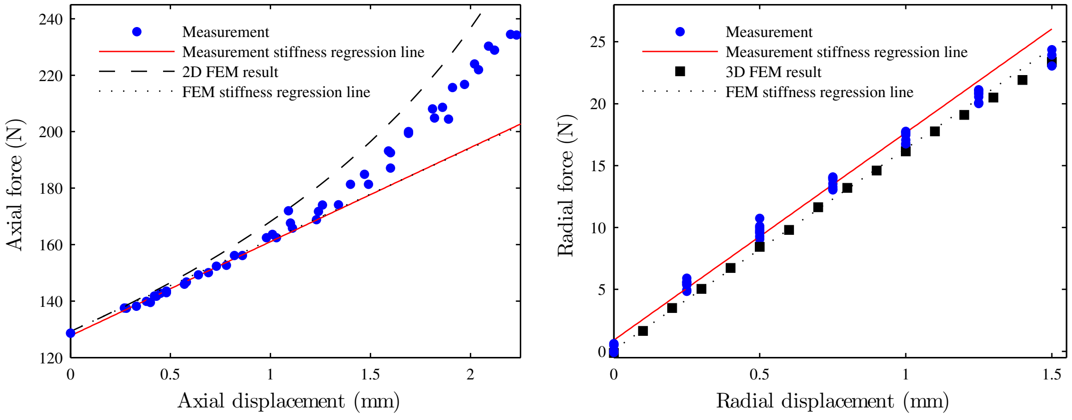

(a) Axial stiffness (b) Radial stiffness

Figure 8.8: Axial and radial force measurements under 1D displacement: (a) Axial force measurements when the rotor is centered; (b) radial force measurements when the airgap is at its nominal value.

Table 8.2: Stiffness results

Parameter[a]	**Measured**	**FEM Result**
Radial Stiffness (N/mm)	16.8	16.2
Axial Stiffness (N/mm)	33.3	32.4

---

[a] All stiffness values are reported about the nominal position and are taken as the slope of the regression lines shown in Fig. 8.9

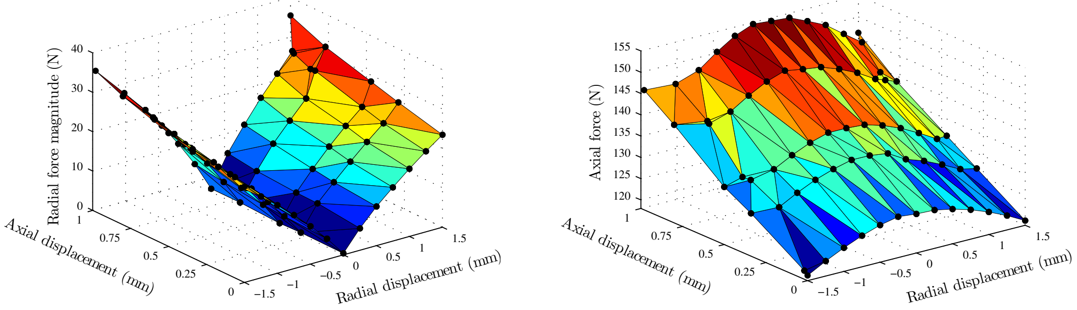

(a) Radial force measurements (b) Axial force measurements

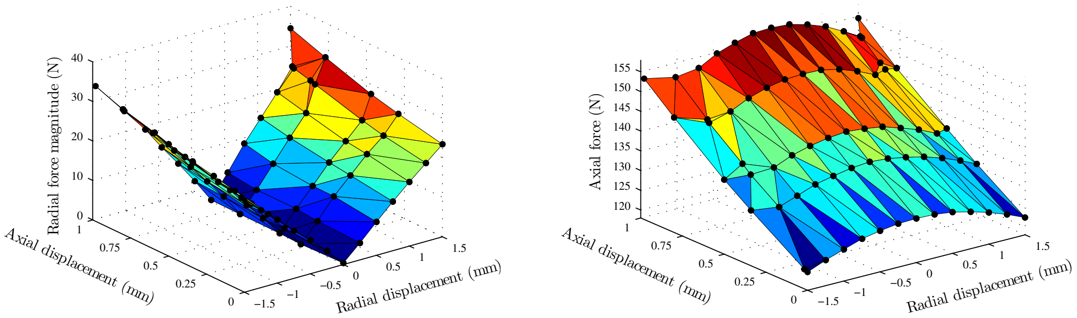

(c) Radial force FEM results (d) Axial force FEM results

Figure 8.9: Comparison of hardware and FEA results: (a) radial force measurements under both axial and radial displacement; (b) axial force measurements under both axial and radial displacement; (c) 3D FEM results for radial forces and (d) 3D FEM results for axial forces under the same displacements as in a) and b); note that positive values of axial displacement indicate a smaller airgap.

selected to be -1.5 mm to 1.5 mm to include the displacement when the bearingless ac homopolar machine is powered down and the shaft is resting upon the touchdown bearings. Fig. 8.9c and 8.9d show FEA results for the same displacements.

Repeatability

To assess the repeatability of the radial force measurements, the radial force data shown in Fig. 8.8b was collected eight times for each radial offset. The standard deviation in measurement data at each radial displacement is calculated. The average of these values is 0.4 N and all standard deviations are within 0.1 N of this. For radial displacements greater than 0.5 mm, the average standard deviation was 2.1% of the average force measured.

Assessing the repeatability of the axial force measurements is more challenging. Since the brass slides exert a frictional force on the rotor shaft, both the axial displacement and axial force differed between measurements for the same weight being placed upon the shaft. Therefore, it is not possible to compare force variation for the same axial displacement. Instead, it was observed from FEA that a quadratic polynomial accurately fit the axial force dependence upon axial displacement. The measured data shown in Fig. 8.8a were fit to a quadratic polynomial using the least squares method and the force difference between each measured data point and the value predicted by the polynomial was calculated and normalized by the value predicted by the polynomial. The average of the normalized error magnitudes is 0.9%.

The repeatability for both radial and axial forces are considered to be very good and any significant measurement error should be due to a systemic bias.

Systemic errors

There were two primary sources for systemic bias error observed in the measurements. The first is that the airgap between the PM bearing and stator was not completely parallel. It was measured at being 2.55 mm nominally and, despite efforts to mount the two surfaces perfectly parallel, there was a deviation of approximately 0.05 mm measured. Finite element simulations results showed that this could lead to a maximum difference in force measurements of 0.9 N over all values of axial and radial displacements tested, which was deemed acceptable. The finite element simulations predicted that for each value of axial displacement, the maximum force difference between the parallel and non-parallel cases would occur for small radial displacements, which possibly accounts for the non-zero radial forces at zero radial displacement shown in Fig. 8.9.

The second source for measurement error was noticeable cross-coupling between the x and y load cells, despite the universal joint linkages. All data was collected by keeping the y-axis in its nominal position and displacing the x-axis. Ideally, the y-axis load cell would always read 0 N. Instead, as can be seen in Fig. 8.10, the y-axis had a substantial offset and varied as a function of x-axis displacement. In addition to this, Fig. 8.10 shows that the x-axis load cell also had a substantial offset. To correct for the offset, a regression line was fit over all the x-axis data points. Ideally, the x-axis data should be perfectly symmetric about the center point ($x = 0$ mm). For this reason, the offset of the linear regression line was treated as the offset of the data. This procedure was applied to all of the radial data measurements. It is interesting to note that the average value of the y-axis force data (21.1 N in Fig. 8.10) is approximately equal to the determined offset in the x-axis data (21.3 N in Fig. 8.10). This suggests that the effect of the airgap not being perfectly parallel is minimal.

Initially, the test apparatus was designed to utilize five single-axis load cells to enable differential x- and y-axis measurements. The expectation was that such measurements would lead to more accurate results. However, the opposite was true: misalignment with the additional sensors caused tension along both the x- and y-axis which caused cross-axis coupling in the force measurement. For this reason, the final test stand consisted of only a single load cell on each axis. Furthermore, the data from the y-axis load cell was not used for any results other than to investigate cross-coupling. All of the presented force measurements in Fig. 8.8 and 8.9 were taken from only two single-axis load cells: one axial load cell and one radial load cell.

8.3 Bearingless winding design

The design of the DPNV winding used in the prototype machine is now considered. This section presents the winding design and an FEA study of study of the performance of this design compared to alternative designs, including a classical bearingless motor

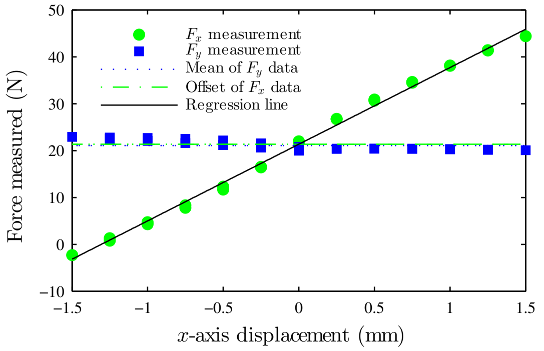

Figure 8.10: Example set of measured data with 2.55mm airgap

design with separate suspension and torque windings.[2]

8.3.1 DPNV winding design

The DPNV winding design procedure described in Section 6.5.3 was used to design the DPNV winding. It was decided that the torque winding should have identical parameters to the prototype ac homopolar motor considered in Chapter 4: $Q = 36$, $p = 4$, $m = 3$. The star of phasors used for the torque winding layout is shown in Fig. 8.11a and a phase of this is redrawn for the suspension frequency in Fig. 8.11c. With reference to Fig. 8.11c, there are two obvious options for which coils to flip for connection to the suspension terminals, forming 180° bands:

(i) starting at the phasor for slot 8 and wrapping around counter-clockwise to the slot 25 phasor,

(ii) starting at the phasor for slot 7 and wrapping around counter-clockwise to the slot 3 phasor.

The resulting suspension winding factors are shown in Table 8.3 in the columns corresponding to a coil pitch of 4 slots. The harmonic $h = 4$ corresponds to the fundamental harmonic $v = 1$ of the torque frequency ($p = 4$). Notice that while option (ii) has a higher fundamental suspension winding factor than option (i), it also has higher harmonic winding factors, which will introduce force ripple in the suspension operation.

---

[2] Portions of the material in this chapter have also been published in [47].

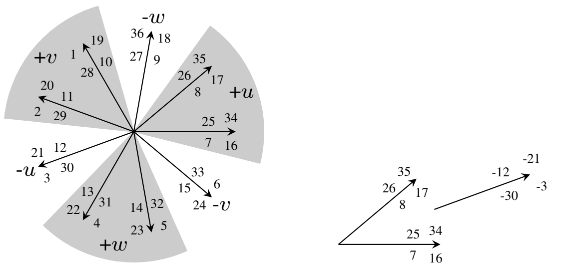

(a) Torque phasor star

(b) Torque phase u conn. star

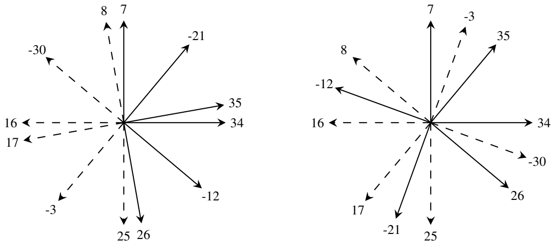

(c) Torque phase u conn. star drawn for $h = p_s$

(d) Torque phase u conn. star drawn for $h = 5$

Figure 8.11: Phasor diagrams for the example $Q = 36$, $p = 4$, $m = 3$ design; (a) torque winding layout using 60° phase belts; (b) phase u at the torque frequency; (c) phase u at the suspension frequency; (d) phase u at the 5th harmonic of the suspension frequency; dashed phasors correspond to coils whose direction is reversed when connected to the suspension terminals

To understand the importance of suspension winding factors on force ripple, refer back to the radial force calculations in Chapter 2. In summary, the Maxwell Stress Tensor is used to calculate radial forces which result from the interaction of the suspension field and the magnetizing field:

$$g_u\left(\alpha,\theta\right) = \tfrac{1}{h_1+h_2 f(p[\alpha-\theta]))} \tag{8.2}$$

$$g_l\left(\alpha,\theta\right) = \tfrac{1}{h_1+h_2 f(p[\alpha-\theta]+\pi))} \tag{8.3}$$

$$B_\psi\left(\alpha,\theta\right) = \mu_0 \frac{\mathcal{F}_\psi}{g_\psi\left(\alpha,\theta\right)} \tag{8.4}$$

where the subscript ψ is set to u or l to indicate the top or bottom airgap and $\mathcal{F}$ represents an MMF. The airgap flux density will contain the harmonics of each MMF as well as plus or minus the harmonics contained in the effective airgap length function $f\left(\phi\right)$ of (8.2). The interaction between the first 11 suspension MMF harmonics and the magnetizing and torque flux density harmonics is summarized in Table 8.4 for the simple case where the effective airgap length function is given by $f\left(\phi\right) = \cos\phi$. The interacting harmonic index of the magnetizing or torque flux density is written as "$(v = ..)$" where v indicates the harmonic of the torque frequency. Harmonics are crossed out which do not exist in this configuration (for example, triplen harmonics, since the phase currents sum to zero, and even suspension harmonics). The first row of the table is the only row that corresponds to a radial force which does not vary with rotor position: the existence of any other row is undesirable. It can be concluded that the most important winding factor to minimize for force ripple is $h = 5$ since it is the only harmonic to interact with main components of both the magnetizing and the torque armature reaction flux density. This harmonic is particularly difficult to deal with because it is near the $p = 4$ torque frequency, meaning that the pitching factor at $h = 5$ is relatively large. For a fixed coil pitch, the only way to minimize this suspension winding factor is by the winding distribution factor; that is, by selecting the coil direction in design step 2 in a way that minimizes this harmonic. The results can be visualized in a phasor star diagram drawn at this frequency, see Fig. 8.11d.

Table 8.3 shows that the suspension winding factors have low values, meaning that current is used inefficiently. This is largely the result of the coil pitch, which was selected for the torque winding design and is therefore extremely short at the suspension frequency. Increasing the coil pitch will result in better suspension winding factor.

Table 8.3: Example design suspension winding factors

	4 slot coil pitch		5 slot coil pitch	
h	winding i	winding ii	winding i	winding ii
1	0.204	0.225	0.252	0.278
3	0.000	0.289	0.000	0.322
5	0.204	0.305	0.170	0.253
7	0.204	0.371	0.027	0.050
9	0.000	0.000	0.500	0.373
11	0.204	0.126	0.316	0.196

Table 8.4: Harmonics leading to force ripple

Sus. MMF Harmonic	Interacting Torque Flux Density Harmonic		
h	h	$h-4$	$h+4$
1	$v=0$	$v=1$	$v=1$
~~2~~	-	-	-
~~3~~	-	-	-
~~4~~	-	-	-
5	$v=1$	$v=0$	$v=2$
~~6~~	-	-	-
7	$v=2$	$v=1$	$v=3$
~~8~~	-	-	-
~~9~~	-	-	-
~~10~~	-	-	-
11	$v=3$	$v=2$	$v=4$

However, this must be done with caution, as it may lead to an inferior torque winding in terms of winding factor, conduction losses, and end-effects. In this particular example with $q = 3/2$, a full pitch coil would be $y = mq = 4.5$ slots. This is typically rounded down to 4 slots to obtain shorter coils. However, if this were rounded up to 5 slots, the suspension winding factors would be improved considerably while the torque winding factors would remain the same, as shown in Table 8.3.

The winding design option (i) with a 4-slot pitch was built for the prototype machine. The layout schematic and MMF diagrams are depicted in Fig. 8.12 alongside an example of an alternate, conventional bearingless winding design which is considered in Section 8.3.3. The prototype machine uses separate, identical windings on top and bottom stator stacks that sandwich the field winding to provide 4-axis control of the rotor's position. The remaining machine parameters of the constructed prototype are specified in Table 8.5.

8.3.2 FEA study of the DPNV winding design

FEA has been conducted on the prototype design for two different DPNV windings, the 4 and 5 slot coil pitch variants of winding i in Table 8.3 (the layout for the former case, which was used in the prototype machine, is depicted in Fig. 8.12b). Two different rotor structures representing lower and upper bounds on the harmonic content of the effective airgap length have been considered: one with an inverted sinusoidal airgap length and one with a square airgap length, where $f(\phi)$ of (8.2) is $\cos\phi$ and $\mathrm{SQ}(\phi)$ respectively. This winding design can be interfaced to either the bridge or parallel style of drive. All simulations have been solved on static, non-linear 3D models using Infolytica's MagNet software, shown in Fig. 8.13a. The machine parameters and ratings are summarized in Table 8.5. The B-H curves used for the laminations and the solid steel are the same as what was previously depicted in Fig. 4.6.

First, the rated coil current is used to create an x-directed suspension force in the top rotor/stator section while no torque current is used. The resulting force and terminal current waveforms are shown in Fig. 8.14a. In the parallel configuration the suspension terminal has a series connection to all coil groups, whereas in the bridge configuration there are two parallel branches; therefore, to obtain the rated coil current, the bridge configuration's suspension terminals carry twice the current of the parallel configuration.

Slot	1	2	3	4	5	6	7	8	9	10	11	12	13	14	15	16	17	18	19	20	21	22	23	24	25	26	27	28	29	30	31	32	33	34	35	36
Top	v	v	$-u$	w	w	$-v$	u	u	$-w$	v	v	$-u$	w	w	$-v$	u	u	$-w$	v	v	$-u$	w	w	$-v$	u	u	$-w$	v	v	$-u$	w	w	$-v$	u	u	$-w$
Mid	v	$-u$	$-u$	w	$-v$	$-v$	u	$-w$	$-w$	v	$-u$	$-u$	w	$-v$	$-v$	u	$-w$	$-w$	v	$-u$	$-u$	w	$-v$	$-v$	u	$-w$	$-w$	v	$-u$	$-u$	w	$-v$	$-v$	u	$-w$	$-w$
Bot	v_s	v_s	v_s	v_s	v_s	v_s	$-u_s$	$-u_s$	$-u_s$	$-u_s$	$-u_s$	$-u_s$	w_s	w_s	w_s	w_s	w_s	w_s	$-v_s$	$-v_s$	$-v_s$	$-v_s$	$-v_s$	$-v_s$	u_s	u_s	u_s	u_s	u_s	u_s	$-w_s$	$-w_s$	$-w_s$	$-w_s$	$-w_s$	$-w_s$

(a) Conventional winding layout (with separate torque and suspension windings) for the example design

Slot	1	2	3	4	5	6	7	8	9	10	11	12	13	14	15	16	17	18	19	20	21	22	23	24	25	26	27	28	29	30	31	32	33	34	35	36
Top	v	v	$-u$	w	w	$-v$	u	u	$-w$	v	v	$-u$	w	w	$-v$	u	u	$-w$	v	v	$-u$	w	w	$-v$	u	u	$-w$	v	v	$-u$	w	w	$-v$	u	u	$-w$
Bot	v	$-u$	$-u$	w	$-v$	$-v$	u	$-w$	$-w$	v	$-u$	$-u$	w	$-v$	$-v$	u	$-w$	$-w$	v	$-u$	$-u$	w	$-v$	$-v$	u	$-w$	$-w$	v	$-u$	$-u$	w	$-v$	$-v$	u	$-w$	$-w$

(b) DPNV winding layout used in the prototype machine

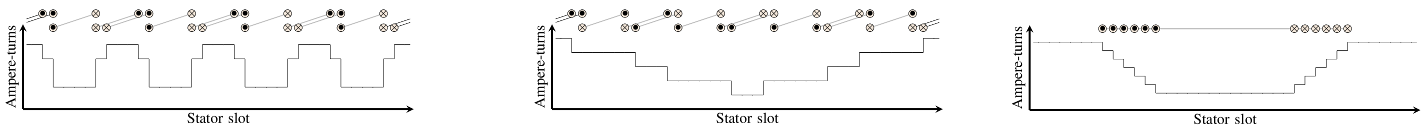

(c) DPNV phase u excited from torque terminal (d) DPNV phase u excited from sus. terminal (e) Phase u separate sus. winding

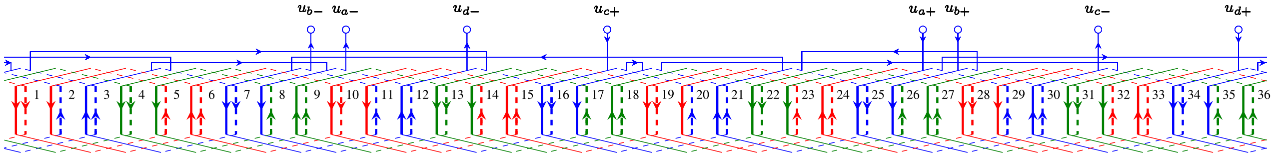

(f) Winding schematic of DPNV winding used in the prototype machine

Figure 8.12: Winding designs for the prototype stator which utilizes a (a) conventional bearingless winding design and (b) DPNV winding design that was constructed in the prototype machine. Torque production requires an 8-pole magnetic field and suspension force production requires a 2-pole magnetic field. Both windings have the same layout with regards to producing the torque MMF; the conventional design has a separate winding for producing the suspension MMF.

Table 8.5: Bearingless prototype machine parameters

Rated Coil Current	2.6 A (RMS)
Rated Torque (Sine Rotor)	2.0 Nm
Rated Torque (Square Rotor)	2.5 Nm
Mean Airgap Radius	53 mm
Min. / Max. Airgap Length	2 mm / 17.5 mm
Stator Segment Active Length	40 mm
Rotor / Stator Lamination Material	M19
Rotor Shaft / Stator Sleeve Material	Solid Rotor Steel
Field Winding Turns	1000
Field Winding Conductor Diameter	0.8 mm
Turns in Each Armature Coil	27
Armature Conductor Diameter	0.8mm

The quality of a bearingless motor's magnetic suspension is often analyzed by looking at the force ripple along each radial axis (x and y) when a force is desired along only one of the axes. The ripple value is typically normalized by the average force produced along the desired axis. This information is extracted from Fig. 8.14a and summarized in the first two rows of Table 8.6. Here, $\Delta F_{x/y}$ is defined as the maximum difference between the force waveform and the average force produced for that axis. As expected from the winding factors, the winding design with a coil pitch of $y = 5$ slots outperforms the shorter pitched design in terms of both the amount of average radial force produced and the amount of normalized force ripple.

Next, the flux linkage of the phase u torque and suspension terminals is explored to identify coupling between the torque and suspension terminals as well as to validate the "no voltage" characteristic of the suspension terminals. Three operation scenarios are considered with different terminal currents, as follows: 1) no suspension or torque current; 2) rated torque current, no suspension current; 3) no torque current, rated suspension current. The results are plotted in Fig. 8.14b for the square rotor with the winding coil pitch of $y = 4$ slots, as this design should exhibit the greatest harmonic content. The flux linkage is measured by summing each coil group's flux linkage (a-d), taking into account the group's direction with respect to the suspension and torque

Table 8.6: FEA results for winding suspension force characteristics

	Sine rotor			Square rotor		
y	$\langle F_x \rangle$	$\frac{\Delta F_x}{\langle F_x \rangle}$	$\frac{\Delta F_y}{\langle F_x \rangle}$	$\langle F_x \rangle$	$\frac{\Delta F_x}{\langle F_x \rangle}$	$\frac{\Delta F_y}{\langle F_x \rangle}$
4 slots[a]	125.9 N	11.1%	11.0%	136.3 N	13.8%	12.3%
5 slots[a]	155.0 N	7.6%	7.3%	167.9 N	9.1%	8.0%
4 slots[b]	42.2 N	13.1%	13.3%	45.7 N	15.1%	16.5%
5 slots[b]	52.1 N	8.2%	9.7%	56.4 N	11.0%	11.2%
18 slots[c]	147.8 N	1.7%	2.3 %	159.7 N	2.6%	2.9%

---

[a] Rated suspension current, no torque current

[b] 1/3 rated suspension current, 2/3 rated torque current

[c] Single layer winding depicted in Fig. 8.12a; rated suspension current; 25% slot space allocation

terminals. It is seen here that the flux linkage of the torque terminal is influenced by the movement of the rotor and the amount of torque terminal current; however, the torque terminal flux linkage is not influenced by the suspension terminal current. The flux linkage at the suspension terminal is also clearly not influenced by the torque current; when the suspension terminal current is at its rated value, the suspension flux linkage exhibits some dependence on the rotor's angular position. This variation in the suspension flux linkage is small compared to variation in the torque flux linkage and will therefore generate a very small relative motional-EMF. The flux density is shown for a 2D cross-section of the top rotor/stator section for each of the three scenarios in Fig. 8.13. It is seen that in scenario 3, the stator teeth carry the most flux, which most likely accounts for the suspension flux linkage's slight rotor position dependence.

Finally, simultaneous torque and suspension current is flown to validate the machine's capability to simultaneously produce both suspension force and torque. The coil current is set to its maximum rated value, but is divided into torque and suspension force producing components which are at 2/3 and 1/3 of the rated current respectively. FEA results for the torque and force waveforms are shown in Fig. 8.15 and a cross-sectional view of the flux density in the top rotor/stator section is shown in Fig. 8.13e. The average suspension force and normalized force ripple has been extracted from Fig. 8.15 and added to Table 8.6. The presence of torque current results in an increase in normalized force ripple. To ensure that this was not due to the use of a lower suspension current,

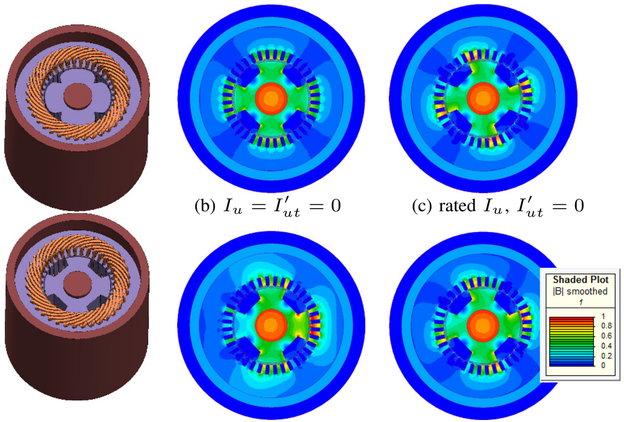

(b) $I_u = I'_{ut} = 0$ (c) rated I_u, $I'_{ut} = 0$

(a) 3D FEA Models (d) $I_u = 0$, rated I'_{ut} (e) $\frac{2}{3}$ rated I_u, $\frac{1}{3}$ rated I'_{ut}

Figure 8.13: FEA models and field results for prototype design winding: (a) Models with sine / square rotors for $y = 4$ slots; (b)-(e) flux density in top rotor/stator cross-section.

the same test was re-run with no torque current, and the suspension current maintained at 1/3 of its rated value; the resulting values of normalized force ripple agreed with the first two rows of Table 8.6. To test for degradation of the torque waveform, this same test was re-run with the same torque currents, but the suspension current set to zero. No significant difference was found in the average torque and torque ripple of both rotor structures and DPNV windings, leading to the conclusion that the suspension current does not interfere with the torque production apart from setting a limit on the amount of torque current that can be used; however, the presence of torque current does result in a slight increase in normalized suspension force ripple.

8.3.3 Comparison to conventional bearingless winding

The example conventional bearingless winding design, depicted in Fig. 8.12a, is now analyzed for comparison purposes. The winding was designed as a full pitch ($y = 18$ slots), single layer winding with 60° phase belts. The winding factors are shown in Table 8.7. Comparing these winding factors to the example DPNV winding factors shown previously in Table 8.3 reveals that the example DPNV suspension winding factors are inferior both in terms of the fundamental winding factor ($h = 1$) and in terms of the harmonic content (k_{wh}/k_{w1}). It is therefore expected that if the example conventional suspension winding could occupy the entire slot space, it would produce

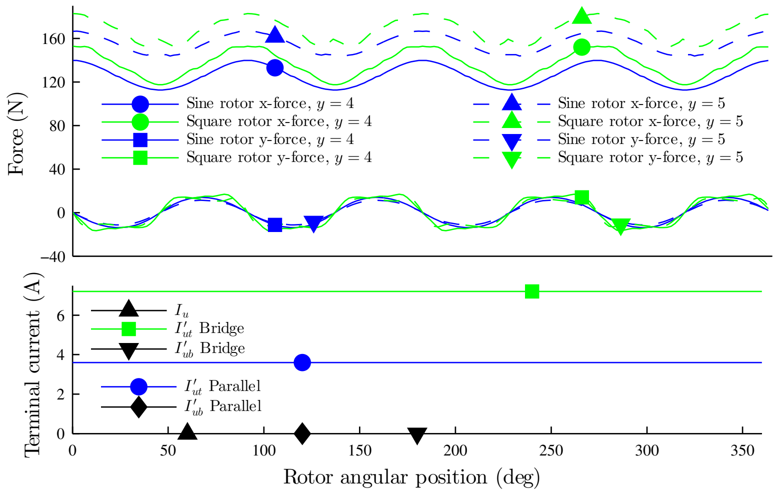

(a) Rated suspension force waveforms when no torque is produced

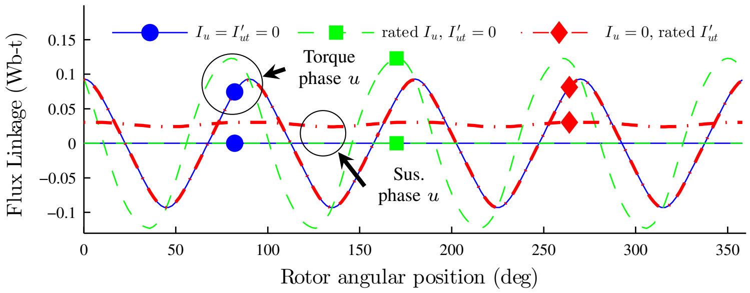

(b) Torque and suspension phase terminal flux linkage ($y = 4$ slots)

Figure 8.14: FEA results for the design variants with $y = 4$ and $y = 5$ DPNV windings for the two different rotor shapes shown in Fig. 8.13a. The terminal currents are indicated for both the bridge and parallel drive implementations. Note: in (b) results are shown for the $y = 4$ DPNV winding with a square rotor and waveforms which pass through the “Torque phase u” circle correspond to the the torque terminal.

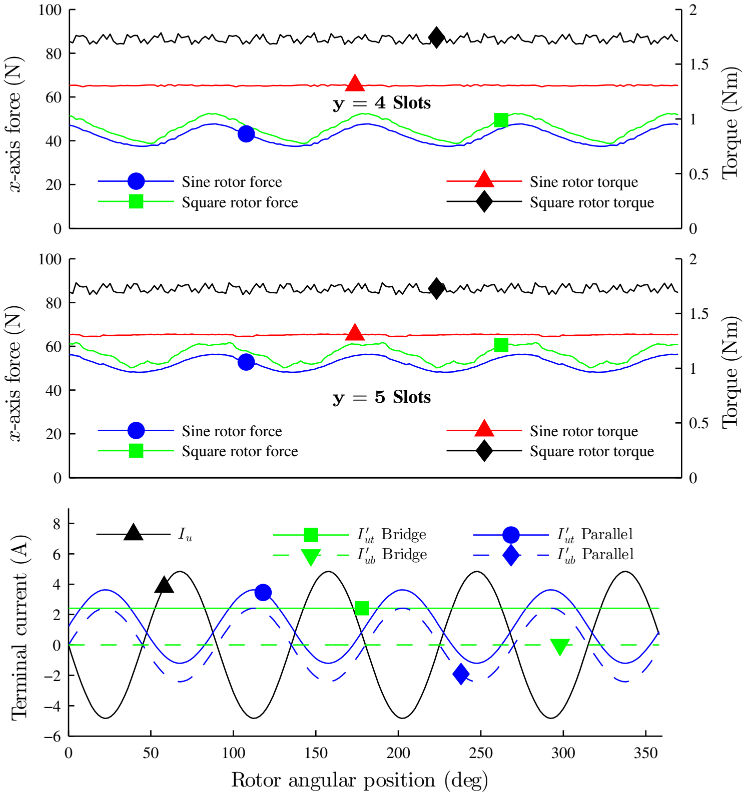

Figure 8.15: FEA results for the design variants with $y = 4$ and $y = 5$ DPNV windings for simultaneous torque and suspension force production when the torque terminal current is 2/3 of its rated value and the top suspension terminal current is 1/3 of its rated value

Table 8.7: Winding factors for example separate suspension winding

h	1	3	5	7	9	11
k_{wh}	0.937	0.515	0.027	0.185	0.101	0.042

a much larger suspension force at the rated suspension current with lower normalized force ripple. However, the conventional suspension winding cannot occupy the entire slot space because a portion of the slot space must be allocated to the torque winding.

FEA was conducted on the example machine when 25% of the slot space is allocated to the suspension winding and 75% to the torque winding. This results in a 25% reduction in the machine's rated torque as compared to the DPNV winding (when the DPNV winding is carrying no suspension current). The suspension force characteristics are summarized in the last row of Table 8.6, where it can be seen that the rated suspension force is comparable to the DPNV designs but the normalized force ripple is much improved.

In a flywheel system, where the rotor has considerable momentum and is rotating at a high speed, the force ripple of the suspension characteristic is hardly a concern. Furthermore, because of the high rotational speed, the flywheel rotor has substantial gyroscopic stability and therefore when the rotor is not passing through a critical speed, the suspension current is expected to be nearly zero, enabling a greater torque capability which is extremely advantageous as it increases the flywheel module's power density. Therefore, even with the low suspension winding factor, the DPNV winding is seen to be at a considerable advantage to the conventional bearingless winding approach for use in flywheel energy storage.

8.4 Control design and implementation

The control implementation of drives for bearingless DPNV machines was previously described Chapter 7 and depicted in Fig. 7.8 for machines with two degrees of freedom in the suspension operation. The constructed bearingless prototype machine has four degrees of freedom: radial x-y position in two planes, giving it x-y control of its shaft as well as tilting in the x and y directions. The rigid body model of this machine was derived in Section 5.2 and the results of this derivation were used to design the control logic for the prototype drive, which is now described. An overview of the control logic is presented; the PI and PID controller designs are investigated; and finally, details of the hardware implementation are summarized.

8.4.1 Control overview

To provide four-axis control, the previously presented control diagram of Fig. 7.8 is replaced by Fig. 8.16. This control is based on the rigid body model depicted in Fig. 5.2, where the rotor position in the x and y axes are decoupled. Detailed diagrams of the position and current controllers are depicted in Fig. 8.17 and the PI and PID in Fig. 8.18.

The rigid body model has state variables of δ_0 and θ, as labeled in Fig. 5.2 and expressed in state-space form in (5.2). An independent set of these states exist for each axis (x and y). Using the transformed inputs defined in (8.5), decoupled transfer functions can be written for each of these states (8.6) which have the same unstable poles that were identified in Section 5.2.

$$\begin{aligned} F_{c1} &= k_f i_{s1} \\ F_{c2} &= k_f i_{s2} \\ F_{\text{sum}} &= F_{c1} + F_{c2} \\ F_{\text{diff}} &= F_{c1} - F_{c2} \end{aligned} \tag{8.5}$$

$$\begin{aligned} \frac{\delta_0(s)}{F_{\text{sum}}(s)} &= \frac{1/m}{s^2 - |k_s|/m} \\ \frac{\theta(s)}{F_{\text{diff}}(s)} &= \frac{r_\delta/I}{s^2 - r_\delta^2 |k_s|/I} \end{aligned} \tag{8.6}$$

The position PID controllers of Fig. 8.17a are designed to operate on these decoupled transfer functions. Note that k_f, i_{s1}, and i_{s2} have the same meaning as defined in Section 5.2. The currents i_{s1} and i_{s2} are the equivalent suspension current in a winding spanning the top or bottom airgap for the given axis (x or y). As was done in Fig. 7.8, these equivalent currents are calculated by a d-q transformation of the three phase suspension currents, using the angle ϕ_f. However, here armature reaction flux is neglected so ϕ_f is a constant value fixed to the x-axis, which in this prototype is set to the phase u winding axis and assigned to 0° (notice the 0 values being fed into the suspension current controllers of Fig. 8.16).

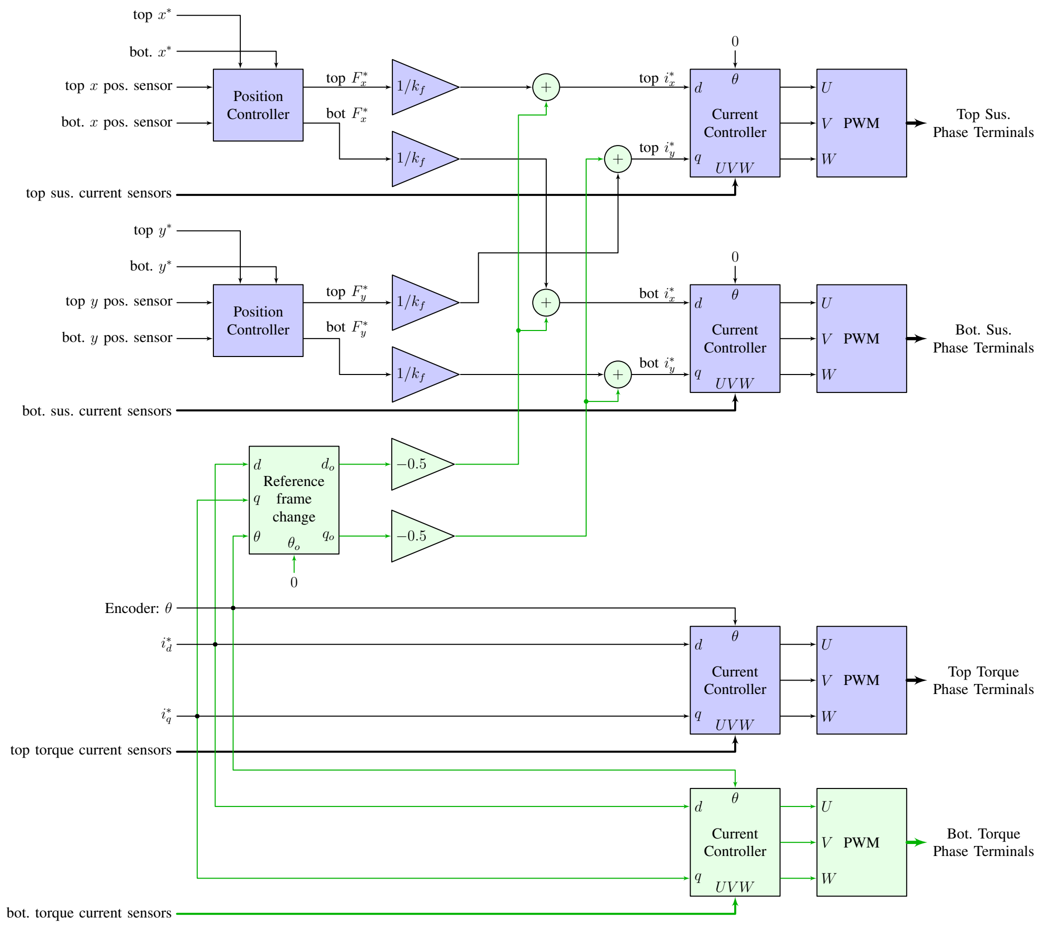

Figure 8.16: Bearingless drive top-level control schematic. The blocks labeled as "Position Controller" and "Current Controller" are depicted in detail in Fig. 8.17. The current controllers for torque current control do not implement zero sequence control. The green elements are only required for the parallel DPNV drive configuration.

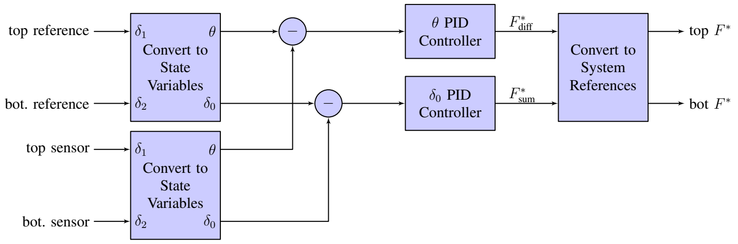

(a) Position controller

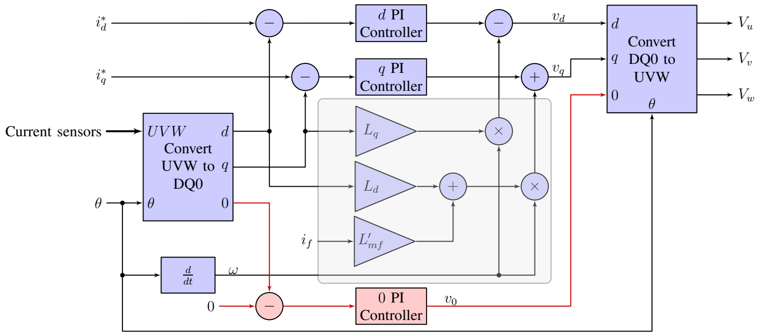

(b) Current controller

Figure 8.17: Position and current control schematics. The red elements are only used when the controller provides zero sequence current control. The elements in the shaded gray box are used for feedforward compensation and are used when $\frac{d\theta}{dt} = \omega \neq 0$, which is only the case for the torque current controllers. The PID and PI controllers are depicted in detail in Fig. 8.18.

In Fig. 8.17a, the θ and δ_0 state variables are calculated from top and bottom rotor position values by the block labeled "Convert to State Variables" by (8.7), using the notation indicated in Fig. 5.2. To speed up the control loop, these equations have been linearized using the small angle approximation that $\sin\theta \approx \theta$. If the position sensors are located at a distance other than r_δ from the axial center of the shaft, this distance is substituted in place of r_δ in (8.7) when calculating the measured rotor position.

$$\begin{aligned}\theta &= \frac{1}{2r_\delta}\left(\delta_1 - \delta_2\right)\\ \delta_0 &= \frac{1}{2}\left(\delta_1 + \delta_2\right)\end{aligned} \tag{8.7}$$

Similarly, the reference values of F_{sum} and F_{diff} that the position controllers generate must be converted back to reference top and bottom forces. This is done by the block labeled as "Convert to System References" in Fig. 8.17a using (8.8).

$$\begin{aligned}F_{c1} &= \frac{F_{\text{sum}} + F_{\text{diff}}}{2}\\ F_{c2} &= \frac{F_{\text{sum}} - F_{\text{diff}}}{2}\end{aligned} \tag{8.8}$$

In Fig. 8.16, the reference force values are divided by k_f to calculate the corresponding suspension current references and then fed into the appropriate top or bottom suspension current controller.

Similar to Fig. 7.8, the extra current control logic required for the parallel DPNV drive configuration is indicated by green shaded blocks. The logic required for zero sequence current control is drawn in red in Fig. 8.17b. As was the case in Chapter 7, these controllers are only present in the suspension current controllers. The computation done in the "Reference frame change" block is given by (8.9). In Fig. 8.17b, the computation done in the "Convert UVW to DQ0" block is given by (8.10) and the "Convert DQ0 to UVW" block performs the inverse of this. When the current controller is being used for suspension currents, d and q quantities are replaced by x and y quantities.

$$\begin{aligned}d_0 &= d\cos\left(\theta - \theta_0\right) - q\sin\left(\theta - \theta_0\right)\\ q_0 &= d\sin\left(\theta - \theta_0\right) + q\cos\left(\theta - \theta_0\right)\end{aligned} \tag{8.9}$$

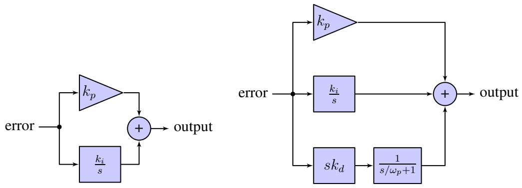

(a) PI controller (b) PID controller

Figure 8.18: PI and PID controller blocks.

$$\begin{Bmatrix} d \\ q \\ 0 \end{Bmatrix} = \sqrt{2/3} \begin{bmatrix} \cos\theta & \cos(\theta - 2\pi/3) & \cos(\theta + 2\pi/3) \\ -\sin\theta & -\sin(\theta - 2\pi/3) & -\sin(\theta + 2\pi/3) \\ 1 & 1 & 1 \end{bmatrix} \begin{Bmatrix} U \\ V \\ W \end{Bmatrix} \tag{8.10}$$

8.4.2 PI current controller design

For both the torque and suspension current controllers, the winding model looks like an R-L load. The resistance is simply the phase resistance and the inductances are the transformed d-q (or x-y) quantities. The machine was designed so that $L_d \approx L_q$ and $L_x \approx L_y$, which means that the d and q PI controllers are identical within a single current controller block. Because of the orientation of the winding coils within a coil group leading to the no-voltage suspension condition, the values of L_x and L_y are simply equal to the phase leakage inductance. The zero sequence R-L plant, and therefore PI controller, is identical to the suspension plant (and PI controller).

The closed loop transfer function used for the current controller design is depicted in Fig. 8.19 where $C(s)$ is the controller, $G(s)$ is the plant, and L corresponds to the d-q or x-y quantity. The loop gain is given by (8.11).

$$\begin{aligned} I_L(s) &= C(s) \times G(s) \\ &= \frac{k_p\left(s + \frac{k_i}{k_p}\right)}{Ls\left(s + \frac{R}{L}\right)} \end{aligned} \tag{8.11}$$

The controller gains (8.12) were chosen to achieve a desired controller bandwidth ω_c and to cancel the plant's open-loop pole. This was done to achieve a first-order closed

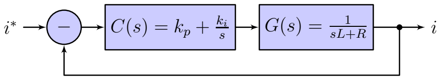

Figure 8.19: Diagram of model for current controller design

loop system (8.13).

$$\begin{aligned} k_p &= L\omega_c \\ k_i &= R\omega_c \end{aligned} \tag{8.12}$$

$$\begin{aligned} I_{CL}(s) &= \frac{I(s)}{I^*(s)} \\ &= \frac{I_L(s)}{1 + I_L(s)} \\ &= \frac{1}{s/\omega_c + 1} \end{aligned} \tag{8.13}$$

8.4.3 PID position controller design

The transfer functions for the θ and δ_0 state variables (8.6) differ in terms of the unstable pole location and gain. This means that different PID controller gains will be used for each PID controller block in Fig. 8.17a. The PID controller implementation is shown in Fig. 8.18b. This is a standard PID controller with the exception that a low pass filter composed of a single high-frequency pole has been placed in series with the derivative term. This is to attenuate the controller's response to high frequency noise that may otherwise result in unstable operation. It should be noted that the simplest controller required to stabilize the system is actually a PD controller. However, such controllers allow for a dc force to result in a constant control error. For this reason, integral action is used.

The PID controller transfer function can be expressed in terms of its poles and zeros (8.14). The controller gains can be calculated from the desired poles, zeros, and dc gain

k_{dc} (8.15).

$$\begin{aligned} C(s) &= k_p + k_i \frac{1}{s} + k_d \frac{s}{s/\omega_p + 1} \\ &= \frac{(k_p/\omega_p + k_d)s^2 + (k_p + k_i/\omega_p)s + k_i}{s\,(s/\omega_p + 1)} \\ &= k_{dc} \frac{(s/\omega_{z1} + 1)\,(s/\omega_{z2} + 1)}{s\,(s/\omega_p + 1)} \end{aligned} \tag{8.14}$$

$$\begin{aligned} k_p &= k_{dc} \left(\frac{\omega_{z1} + \omega_{z2}}{\omega_{z1}\omega_{z2}} - \frac{1}{\omega_p} \right) \\ k_i &= k_{dc} \\ k_d &= k_{dc} \left(\frac{1}{\omega_{z1}\omega_{z2}} - \frac{\omega_{z1} + \omega_{z2}}{\omega_{z1}\omega_{z2}\omega_p} + \frac{1}{\omega_p^2} \right) \end{aligned} \tag{8.15}$$

To generalize the design procedure, a generic plant transfer function is defined here (8.16), where k_G and ω_x are replaced with the actual values of either transfer function defined in (8.6).

$$\begin{aligned} G(s) &= \frac{\omega_x^2 k_G}{s^2 - \omega_x^2} \\ &= \frac{k_G}{(s/\omega_x + 1)\,(s/\omega_x - 1)} \end{aligned} \tag{8.16}$$

The closed loop model used for the PID controller design is depicted in Fig. 8.20, where $I_{CL}(s)$ corresponds to the inner current control loop. The frequency design method is used, with the primary objective of stabilizing the system. Approximated, idealized bode plots of the various model transfer functions are shown in Fig. 8.21 where it is seen that $G(s)$ has a constant phase angle of $-180°$. To stabilize the system, the open-loop phase angle must be greater than $-180°$ at the cross-over frequency (the frequency at which the loop gain is at unity magnitude). To do this, the first zero of (8.14) must be located far below the cross-over frequency to boost the phase angle and prevent premature attenuation of the loop gain due to the poles of $G(s)$. The location of the second zero is chosen to further boost the phase angle to obtain a desired phase margin at the cross-over frequency. The dc gain k_{dc} of $C(s)$ is used to set the cross-over frequency. Finally, the pole in series with the PID controller's derivative term is set to a value far greater than the cross-over frequency.

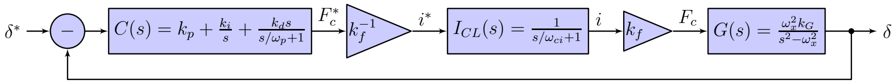

Figure 8.20: Diagram of model for position controller design

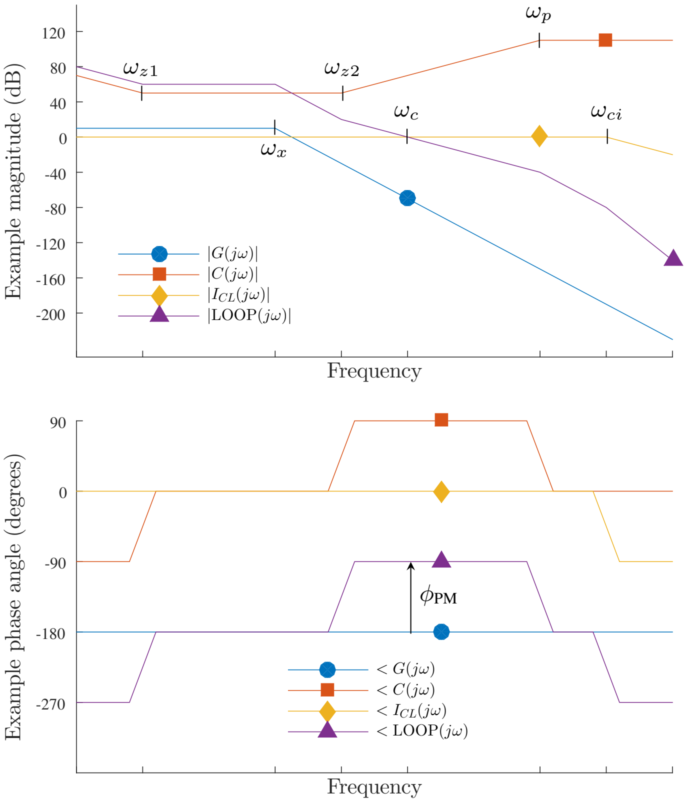

Figure 8.21: Idealized bode diagram used for designing the PID controller

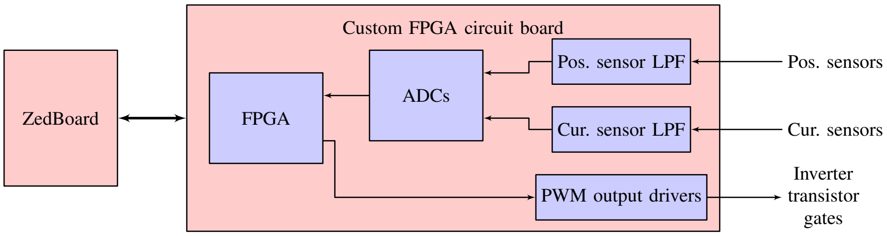

Figure 8.22: Schematic of the control hardware. The actual hardware is shown in Fig. 8.3.

The primary design input parameters are the desire phase margin ϕ_{PM} and the cross-over frequency ω_c, which have a strong effect on the suspension performance. The controller gains were calculated from these parameters by (8.17). The expressions for ω_{z1} and ω_p were chosen based on what worked well in practice. As will be discussed later, it is suspected that a detailed controller tuning effort may yield significant improvement in suspension performance.

$$\begin{aligned}
\omega_{z1} &= \omega_c/100 \\
\omega_p &= 4\omega_c \\
\omega_{z2} &= \frac{\omega_c}{\tan\left(\phi_{\mathrm{PM}} + 90 + \arctan\frac{\omega_c}{\omega_{ci}} - \arctan\frac{\omega_c}{\omega_{z1}} + \arctan\frac{\omega_c}{\omega_p}\right)} \\
k_{dc} &= \frac{1}{\left|C(j\omega_c)\big|_{k_{dc}=1}\right| \, |I_{CL}(j\omega_c)| \, |G(j\omega_c)|}
\end{aligned} \tag{8.17}$$

8.4.4 Hardware implementation

A diagram of the control hardware is shown in Fig. 8.22. The main control logic has been written in C code and runs bare-metal on the DSP portion of a Xilinx Zynq SoC. The DSP board is interfaced to a custom FPGA circuit board developed in the UMN Power Electronic's Research Laboratory via a high speed data bus. This custom FPGA circuit board contains analog to digital converters (ADCs) to interface to the eddy current position sensors used for rotor position feedback and the hall-effect current sensors used to measure the phase current. Low pass, first order filters are placed in front of the ADCs to prevent aliasing. These filters are implemented with simple R-C circuits.

The FPGA circuit board also contains the PWM output drivers which are used to send transistor gate pulses to the power electronic inverters. The power electronic inverter circuit topologies used were described in Chapter 7. The DSP writes duty ratio values for each 2-level half-bridge inverter circuit to the FPGA. The FPGA then generates PWM signals from these duty ratio values via a triangle comparator. The FPGA synchronizes its sampling of the ADCs to the positive and negative peaks of triangle comparator to minimize switching noise. This means that the ADCs are sampled at twice the inverter's switching frequency. The FPGA then uses first-order, low pass digital filters to remove frequency components that would be aliased by the DSP's digital control loops' sample rate. The filtered ADC values are stored in FPGA registers from which the DSP reads new values at every iteration of its digital control loops.

The machine parameters used for the controller design are given in Table 8.8 and the controller parameters and hardware information are provided in Table 8.9.

There was no encoder used in the final prototype testing. Instead, a stationary value of θ from Fig. 8.16 was selected and a torque current was flown to align the rotor. Then, increasing values of ω were used until the desired ω value was obtained. If ω was increased too rapidly or reached too great of a value, the machine would lose synchronism and the rotor would spin down. While the lack of an encoder made it impossible to flow true q or d axis current and limited the maximum rotational speed, it was advantageous to the suspension performance results because it meant that the rotor had no contact with, and therefore experienced no forces from, the stator. Future work is planned to mount an encoder onto the rotor in a way that provides minimal interference from the stator and will allow test results to be taken at higher rotational speeds.

When the rotor is centered in the airgap, the suspension system is at an unstable equilibrium and therefore a well-tuned suspension control system should require very little current. However, despite efforts to precisely align the axial PM bearing and the eddy current position sensors, zero position references for the top and bottom x/y rotor position (top x^*, bot. x^*, top y^*, bot. y^*) required significant suspension current to maintain the rotor's position. To remedy this, the magnetic center of the system was found by "tuning" the values of the position references. This was done with an iterative process, as follows:

1) rotate the rotor in 10° increments (corresponding to the cogging locations for a

Table 8.8: Machine parameters used for controller design

	Bridge	Parallel
Suspension R^a	1.1Ω	3.0Ω
L_x, L_y, ${L_0}^b$	0.41 mH	4.50 mH
Torque R^c	0.8Ω	
L_d, ${L_q}^d$	3.80 mH	
L'_{mf}	5.60 mH	
$k_f(i_f)^e$	$11.4i_f + 0.8i_f^2 - 0.52i_f^3$	$22.8i_f + 1.6i_f^2 + -1.05i_f^3$
$k_s(i_f)$	$\left(35.9i_f - 246.2i_f^2 + 41i_f^3\right) \times 10^3$	
m	12 kg	
I	$0.105\,\text{kg-m}^2$	
r_δ	48.5 mm	
${r_{\text{sense}}}^f$	191 mm	

---

[a] All sus. resistance values were measured using an LCR meter at the inverter terminals.

[b] All sus. inductance values were measured using an LCR meter at a frequency near the current controller's bandwidth at the inverter terminals.

[c] DC measurement using a multimeter

[d] All torque inductance values were calculated using 3D FEA.

[e] k_f and k_s are specified as polynomials of the field current as was done in Chapter 5. The polynomial parameters were calculated using 3D FEA models of the constructed prototype in the same manner as in Chapter 5.

[f] The axial distance from the position sensor to the center of the shaft. This replaces r_δ when calculating the state variables from position sensor readings in (8.7)

Table 8.9: Control design and hardware parameters[a]

ϕ_{PM}	50° for δ_0, 60° for θ
Position controller ω_c	$2\pi \times 75$Hz
Current controller ω_c	$2\pi\times$ 1.25kHz for sus., 1kHz for torque
R-C filter bandwidth[b]	$2\pi\times$ 3.6kHz for pos., 16kHz for cur. sensors
Digital filter bandwidth[c]	$2\pi\times$ 400Hz for pos., 9kHz for cur. sensors
Digital control frequency[d]	20kHz
Inverter switching frequency	100kHz
DSP	Xilinx Zynq-7000 AP SoC XC7Z020-CLG484
	on the Avnet ZedBoard 7020
FPGA	Xilinx Spartan 3E XC3S500E
	on a custom PCB
Position sensors	Kaman DIT5200-20N

---

[a] Several different values of phase margin, filter bandwidth, and controller bandwidth were used. The data presented in this table are the final values which were found to yield the most satisfactory performance.

[b] This is the bandwidth of the first-order, low pass filter used on the FPGA circuit board to prevent ADC sampling aliasing.

[c] This is the bandwidth of the first-order, low pass digital filter that the FPGA uses on sampled ADC values to prevent digital control aliasing.

[d] The frequency, or inverse of the sampling rate, at which the digital control loops were run.

Table 8.10: Final reference values for the rotor's magnetic center

top x^*	0.251 mm
top y^*	-0.053 mm
bot. x^*	0.089 mm
bot. y^*	-0.140 mm

36 slot stator) and average the required x and y top and bottom currents over an entire revolution;

2) change each position reference in a manner to decrease the magnitude of the averaged x and y top and bottom currents;

3) repeat steps 1) and 2) until satisfactory stationary suspension currents are obtained.

This process had to be repeated every time any modification was made to the test stand which disrupted the magnetic center. Final reference values used are shown in Table 8.10.

8.5 Results

Results from the hardware prototype of the bearingless machine are now presented. The DPNV winding was tested in both a parallel and a bridge configuration with and without zero sequence current controllers for various speeds and armature torque current values.[3]

8.5.1 No load

First, the machine was operated with mechanical bearings to measure the no-load terminal voltage characteristic. A dc power supply was used to provide rated current to the field winding. An electric drill was coupled to the rotor and used to rotate the rotor at 1000RPM. The results of this are shown in Fig. 8.23 for the armature coil groups

---

[3] Portions of the material in this chapter have also been published or submitted for publication in [46, 47, 49].

connected in both parallel and bridge configurations. From these results, it is clear the suspension winding experiences no significant motional-EMF.

8.5.2 Full bearingless operation

Experimental results are now presented for the parallel and bridge under full bearingless motor operation at a rotational speed of 1000RPM while 1.5A RMS of current is flowing in the motor phases. In an effort to illustrate the torque inverter's impact on the suspension terminal currents, only the torque inverter for the top DPNV winding is connected in both configurations.

In the bridge configuration, 20V buses were used for the suspension inverters and a 40V bus was used for the torque inverter. The terminal currents are shown in Fig. 8.24b along with the orbital x-y positions in Fig. 8.24a. An ac suspension current with a frequency equal to the rotational speed is clearly visible. This is because the rotor does not remain perfectly centered over a single revolution, causing the suspension controller to generate restorative forces with a period of one revolution. Terminal current waveforms for the parallel DPNV drive are shown in Fig. 8.24c. This drive is implemented with a single voltage bus of 40V, matching Fig. 7.6a.

The suspension controller's measured shaft displacement input and force references were logged and are displayed in Fig. 8.25. This data shows that the machine is utilizing approximately 18% of its rated suspension force, meaning that approximately 82% of the slot space can be devoted to torque production. As the rotor speed increases, gyroscopic stabilization increases which decreases the amount of required suspension force, giving the machine a higher torque capability. This dynamic torque capability compares favorably to the example of a conventional bearingless winding design considered in Section 8.3.3 where the torque slot space was permanently fixed at 75%.

The bridge and parallel configured drives were both operated with and without the zero sequence current controller described in Fig. 7.9 of Section 7.5. The zero sequence currents are calculated from (7.11) and the results are shown in Fig. 8.26. For the bridge configuration, it can be seen in Fig. 8.26a that there was very little zero sequence current present without the controller, and therefore little improvement was obtained with the zero sequence controller. However, the results for the parallel configuration without the zero sequence controller had significant circulating currents and highly distorted

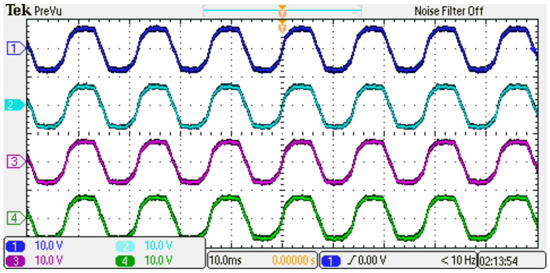

(a) Individual coil groups

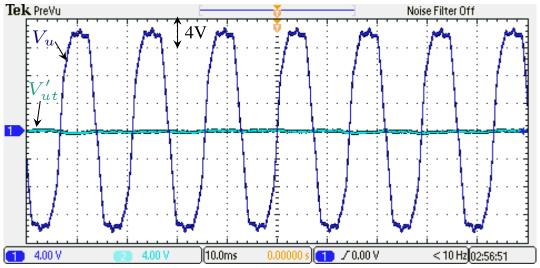

(b) Parallel configuration

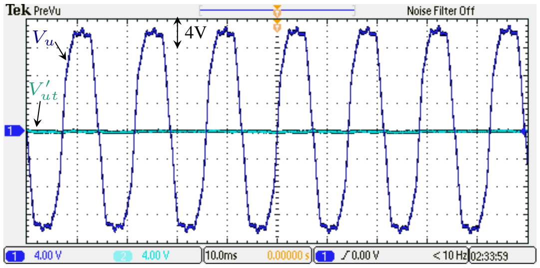

(c) Bridge configuration

Figure 8.23: No-load torque (V_u) and suspension (V'_{ut}) terminal voltages when the shaft is centered with mechanical bearings and rotated at 1000 RPM.

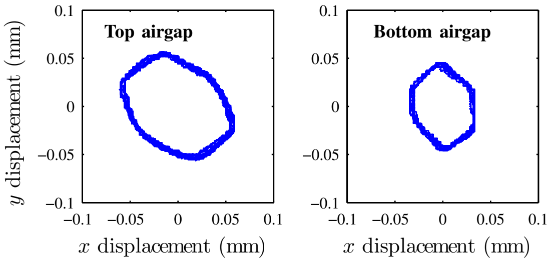

(a) Orbital x-y position (Bridge config.)

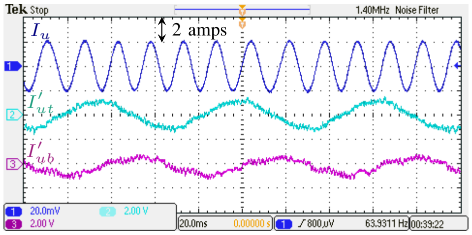

(b) Bridge phase u terminal currents

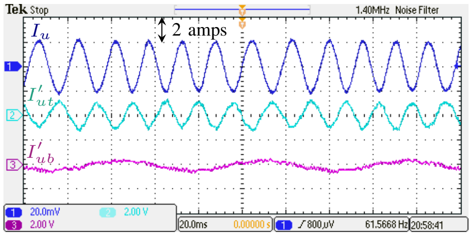

(c) Parallel phase u terminal currents

Figure 8.24: Experimental results from both the bridge and parallel DPNV drives with zero sequence current controllers

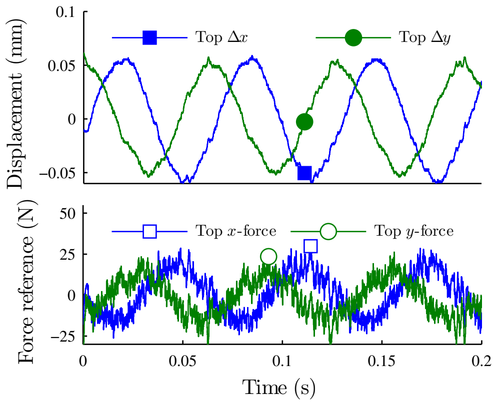

(a) Top displacement and force reference

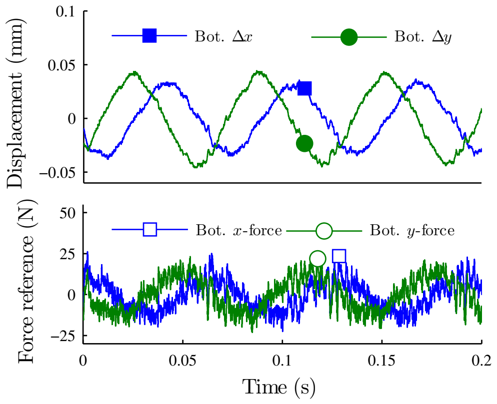

(b) Bottom displacement and force reference

Figure 8.25: Position controller measurements and reference waveforms for the bridge configuration. The data were collected from the DSP-based controller: the controller's measured x and y displacements and generated x and y corrective forces were logged for 200ms.

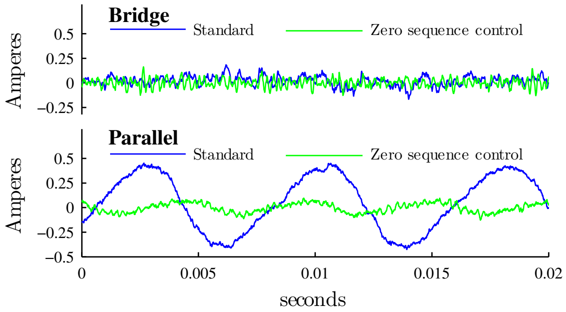

(a) Zero sequence currents

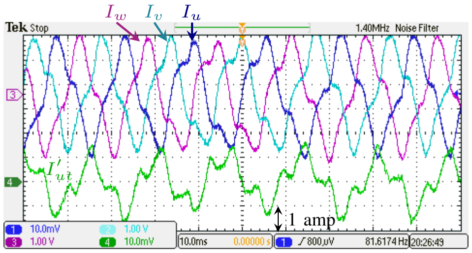

(b) Without zero sequence control

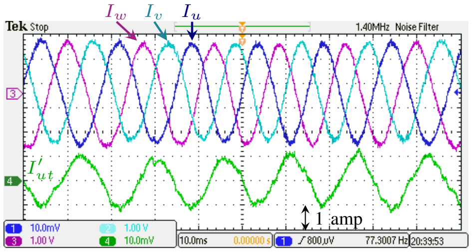

(c) With zero sequence control

Figure 8.26: Experimental results indicating the need for zero sequence current control; (b) and (c) are for the parallel drive configuration.

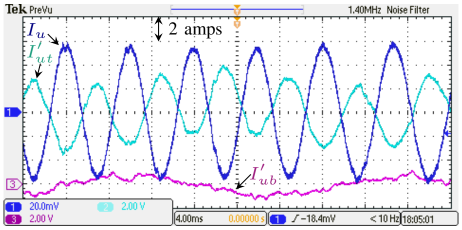

(a) Phase u terminal currents

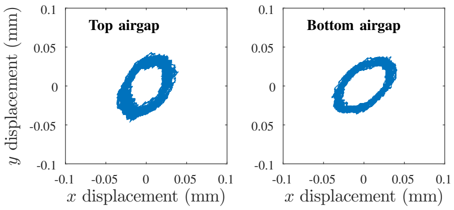

(b) Rotor's orbital position in each airgap

Figure 8.27: Results for parallel configuration at 2500 RPM with 85% of rated torque terminal current; I'_{ut} and I'_{ub} are the currents into the top and bottom suspension terminals; the data in (b) was collected over a period of one second.

terminal current waveforms, shown in Fig. 8.26b. In this case, adding zero sequence current control made a substantial improvement to the terminal current waveforms, shown in Fig. 8.26c.

Finally, to investigate the effect of loading on the bearingless performance for different rotational speeds, the machine was operated at various levels of the rated torque current in the top airgap winding and for varying speeds up to 2500 RPM. Again, the bottom torque inverter was disconnected to clearly demonstrate the impact of torque current. Isolated voltage buses were used for the suspension and torque inverters to enable the torque inverters to have a higher voltage bus to support the greater back-EMF present at high rotational speeds while allowing the suspension inverters to have a lower voltage bus to minimize EMI in the position sensors. The rotor displacement was recorded for each airgap over a period of one second under varying conditions. The maximum displacement observed is shown in Fig. 8.28. The amount of torque terminal current is found to have no effect on the machine's bearingless performance. Furthermore, the machine's control is clearly about to maintain the rotor's position at all tested speeds.

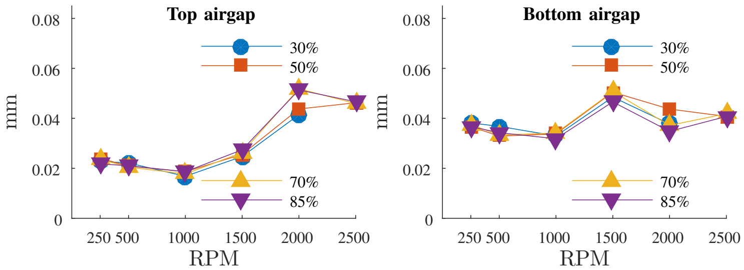

Figure 8.28: The maximum displacement of the rotor in either the x or y direction for each airgap over a range of rotational speed and torque terminal current. The torque terminal current is indicated as a percentage of the rated current.

Chapter 9

Conclusion and Future Work

9.1 Conclusion

The primary conclusion of this dissertation is that energy storage devices based on flywheel technology have the potential to simultaneously provide both frequency regulation and load following services to the power grid in a modular form factor that can be installed locally on a per-need basis. However, to develop such a device, key obstacles in flywheel technology must be resolved. The most important of which is the high rate of self-discharge that flywheel systems experience when idling due to magnetic losses in the permanent magnet motor/generator. This dissertation has re-envisioned the design of flywheel energy storage devices to be based around the bearingless ac homopolar machine. It has shown that the field excitation of this machine can be easily removed when idling to eliminate the magnetic losses that cause self-discharge. Furthermore, the dissertation has shown that designs based around the ac homopolar machine allow for several secondary benefits to flywheel systems, including reduced overall system complexity and cost due to the elimination of separate radial magnetic bearings.

At the onset of this disseration, the bearingless ac homopolar machine was an immature technology with very few examples of prototype machines available in the literature. This dissertation has advanced the state-of-the-art of this technology as both a bearingless machine and as a motor through contributions in magnetic modeling, winding design, control, and presenting experimental validation of these aforementioned contributions. All of this has laid the ground work and justification for future design optimization of this machine.

Finally, this dissertation has also made significant contributions to the broader field of bearingless machine design through its derivation of dual purpose no voltage winding design rules, a design procedure, and drive implementations. By using the same coils for both torque and radial force production, these windings will increase the torque density of future bearingless machine designs and reduce the cost of bearingless machines to values closer to what is required of non-bearingless machines. In effect, this technology will lower the threshold of need that is required to consider a bearingless design, resulting in more optimal electromechanical devices.

9.2 Future work

Several future projects are suggested to continue the development of flywheel energy storage based around the bearingless ac homopolar machine as well as to continue the development of dual purpose no voltage bearingless windings.

- The experimental validation of the prototype has placed no emphasis on optimal control. It is suggested that future work experimentally measure the machine's suspension transfer functions and thoroughly explore the performance improvements that can be achieved by control tuning or alternative control implementations. Furthermore, the experimental prototype did not make use of an encoder and because of this the maximum achievable rotational speed was limited to 2500 RPM. Next steps should involve either mounting an encoder on the prototype or exploring sensorless techniques (see the next item) to increase the rotational speed. Note that higher speeds may require more advanced control design to handle the changing suspension pole locations due to gyroscopic effects.

- An exploration of sensorless and self-sensing control techniques for both the rotor's angular position and the rotor's linear position is suggested. The eddy current linear position sensors used for feedback were expensive and, if they are required in final flywheel system designs, would constitute a significant portion of the module's cost. While angular position detection can be implemented with low-cost equipment, it adds manufacturing complexity/cost and overall system reliability concerns. For these reasons, a fully position-sensorless flywheel system would have considerable advantages.

- Now that computationally efficient magnetic models have been developed and once sensorless techniques are developed and validated in the bearingless ac homopolar prototype, the logical next step is to consider the design optimization of an outer-rotor prototype. Of particular interest is the achievable cost/kWh, cost/kW, and suspension power needed to maintain levitation while the machine is idling. The suspension power will act as a source of self-discharge, which must be carefully considered in the design optimization. Also of interest in the design optimization is the mechanical design integrating the flywheel and the machine's rotor. The loading from the rotor teeth at high speeds and the PM axial bearing on the flywheel will need to be taken into account. When carbon composite flywheels are used, careful consideration must be given to the machine's operating temperature to prevent weakening and catastrophic flywheel failure.
- Apart from flywheel energy storage, future work can be conducted to continue the development of bearingless machines with dual purpose no voltage windings. One aspect of these windings which has not been explored in this dissertation is their ability to passively provide corrective forces when the rotor is eccentric. Designs that generate these forces can use standard motor windings (that have modified end-connections) and must only have their suspension terminal connections short-circuited. The generated forces could potentially be used to dampen rotor vibrations in conventional machine designs and, because this comes at nearly no additional cost, could have a huge impact on large-scale machines where reliability is especially important. Future work focusing in this area should explore requirements on winding factors and rotational speeds to develop significant forces in the presence of eccentricity.

References

[1] Brendan J Kirby. *Frequency regulation basics and trends.* United States. Department of Energy, 2005.

[2] J.P. Barton and D.G. Infield. Energy storage and its use with intermittent renewable energy. *Energy Conversion, IEEE Transactions on*, 19(2):441–448, 2004.

[3] A. Oudalov, T. Buehler, and D. Chartouni. Utility scale applications of energy storage. In *Energy 2030 Conference, 2008. ENERGY 2008. IEEE*, pages 1–7, 2008.

[4] H. Ibrahim, A. Ilinca, and J. Perron. Energy storage systems characteristics and comparisons. *Renewable and Sustainable Energy Reviews*, 12(5):1221 –1250, 2008.

[5] Ioannis Hadjipaschalis, Andreas Poullikkas, and Venizelos Efthimiou. Overview of current and future energy storage technologies for electric power applications. *Renewable and Sustainable Energy Reviews*, 13(6):1513–1522, 2009.

[6] Paul Denholm, Erik Ela, Brendan Kirby, and Michael Milligan. The role of energy storage with renewable electricity generation. 2010.

[7] C.S. Hearn, M.C. Lewis, S.B. Pratap, R.E. Hebner, F.M. Uriarte, Dongmei Chen, and R.G. Longoria. Utilization of optimal control law to size grid-level flywheel energy storage. *Sustainable Energy, IEEE Transactions on*, 4(3):611–618, 2013.

[8] M.L. Lazarewicz and T.M. Ryan. Integration of flywheel-based energy storage for frequency regulation in deregulated markets. In *Power and Energy Society General Meeting, 2010 IEEE*, pages 1–6, 2010.

[9] V.A. Boicea. Energy storage technologies: The past and the present. *Proceedings of the IEEE*, 102(11):1777–1794, Nov 2014.

[10] Gauthier Delille and Bruno François. A review of some technical and economic features of energy storage technologies for distribution system integration. *Ecological engineering and environment protection*, 1:40–49, 2008.

[11] P. Fairley. Flywheels get their spin back [news]. *Spectrum, IEEE*, 52(1):18–18, January 2015.

[12] Beacon Power. [online]. `http://www.beaconpower.com/`. Accessed: 2015-05-13.

[13] PowerThru. Clean flywheel energy storage systems [online]. `http://www.power-thru.com/`. Accessed: 2015-05-13.

[14] M.M. Flynn, P. McMullen, and O. Solis. Saving energy using flywheels. *Industry Applications Magazine, IEEE*, 14(6):69–76, November 2008.

[15] M. Lafoz Pastor, L. Garcia-Tabares Rodriguez, and C. Vazquez Velez. Flywheels store to save: Improving railway efficiency with energy storage. *Electrification Magazine, IEEE*, 1(2):13–20, Dec 2013.

[16] Rotonix. [online]. `http://rotonix.com/`. Accessed: 2015-05-13.

[17] Amber Kinetics. [online]. `http://www.amberkinetics.com/`. Accessed: 2015-05-13.

[18] M.A. Pichot and M.D. Driga. Loss reduction strategies in design of magnetic bearing actuators for vehicle applications. *Magnetics, IEEE Transactions on*, 41(1):492–496, Jan 2005.

[19] M. Strasik, P.E. Johnson, A.C. Day, J. Mittleider, M.D. Higgins, J. Edwards, J.R. Schindler, K.E. McCrary, C.R. McIver, D. Carlson, J.F. Gonder, and J.R. Hull. Design, fabrication, and test of a 5-kwh/100-kw flywheel energy storage utilizing a high-temperature superconducting bearing. *Applied Superconductivity, IEEE Transactions on*, 17(2):2133–2137, June 2007.

[20] M. Flynn. *A Methodology for Evaluating and Reducing Rotor Losses, Heating, and Operational Limitations of High-Speed Flywheel Batteries.* PhD thesis, The University of Texas at Austin, Austin, TX, 2003.

[21] H.J. Bornemann, A. Tonoli, T. Ritter, C. Urban, O. Zaitsev, K. Weber, and H. Rietschel. Engineering prototype of a superconducting flywheel for long term energy storage. *Applied Superconductivity, IEEE Transactions on*, 5(2):618–621, June 1995.

[22] P.P. Acarnley, B.C. Mecrow, J.S. Burdess, J. N. Fawcett, P.G. Dickinson, and J. G. Kelly. An integrated flywheel/machine energy store for road vehicles. In *New Topologies for Permanent Magnet Machines (Digest No: 1997/090), IEE Colloquium on*, pages 9/1–9/6, 1997.

[23] M. A. Pichot, J.P. Kajs, B. R. Murphy, A. Ouroua, B. Rech, R.J. Hayes, J.H. Beno, G.D. Buckner, and A.B. Palazzolo. Active magnetic bearings for energy storage systems for combat vehicles. *Magnetics, IEEE Transactions on*, 37(1):318–323, 2001.

[24] RJ Hayes, JP Kajs, RC Thompson, and JH Beno. Design and testing of a flywheel battery for a transit bus. *SAE transactions*, 108(6; PART 2):2199–2207, 2000.

[25] Clay Stephen Hearn. *Design methodologies for advanced flywheel energy storage.* PhD thesis, The University of Texas at Austin, Austin, TX, 2013.

[26] H. Hofmann. *High-speed synchronous reluctance machine for flywheel applications.* PhD thesis, The University of California at Berkley, Berkley, CA, 1998.

[27] Perry Tsao, M. Senesky, and S.R. Sanders. An integrated flywheel energy storage system with homopolar inductor motor/generator and high-frequency drive. *Industry Applications, IEEE Transactions on*, 39(6):1710 – 1725, nov.-dec. 2003.

[28] T. Ichihara, K. Matsunaga, M. Kita, Izumi Hirabayashi, M. Isono, M. Hirose, K. Yoshii, K. Kurihara, O. Saito, S. Saito, M. Murakami, H. Takabayashi, M. Natsumeda, and N. Koshizuka. Application of superconducting magnetic bearings to a 10 kwh-class flywheel energy storage system. *Applied Superconductivity, IEEE Transactions on*, 15(2):2245–2248, June 2005.

[29] F.N. Werfel, U. Floegel-Delor, T. Riedel, R. Rothfeld, D. Wippich, B. Goebel, G. Reiner, and N. Wehlau. A compact hts 5 kwh/250 kw flywheel energy storage system. *Applied Superconductivity, IEEE Transactions on*, 17(2):2138–2141, June 2007.

[30] Peter Kascak. *Fully Levitated Rotor Magnetically Suspended By Two Pole-Pair Seperated Conical Motors.* PhD thesis, Case Western University, Cleveland, OH, 2010.

[31] Qian Wang, Chengjun Liu, Jibin Zou, Xinghe Fu, and Juan Zhang. Numerical analysis and design optimization of a homopolar inductor machine used for flywheel energy storage. *Plasma Science, IEEE Transactions on*, 41(5):1290–1294, May 2013.

[32] Trong Duy Nguyen, G. Foo, King-Jet Tseng, and D.M. Vilathgamuwa. Modeling and sensorless direct torque and flux control of a dual-airgap axial flux permanent-magnet machine with field-weakening operation. *Mechatronics, IEEE/ASME Transactions on*, 19(2):412–422, April 2014.

[33] Todd Andrew Begalke. *Synchronous Reluctance Drive for Flywheel Batteries.* PhD thesis, University of Minnesota, 2006. Major: Electrical engineering., 2006.

[34] Maria Inês Lopes Marques. *Design and Control of an Electrical Machine for Flywheel Energy-Storage System.* PhD thesis, MA thesis, IST, Lisbon, Portugal, 2008.

[35] J. Santiago, J.G. Oliveira, J. Lundin, A. Larsson, and H. Bernhoff. Losses in axial-flux permanent-magnet coreless flywheel energy storage systems. In *Electrical Machines, 2008. ICEM 2008. 18th International Conference on*, pages 1–5, Sept 2008.

[36] Jae-Do Park, C. Kalev, and H.F. Hofmann. Control of high-speed solid-rotor synchronous reluctance motor/generator for flywheel-based uninterruptible power supplies. *Industrial Electronics, IEEE Transactions on*, 55(8):3038–3046, Aug 2008.

[37] Seok-Myeong Jang, Ji-Hoon Park, Dae-Joon You, and Sang-Ho Choi. Analysis on operational power and eddy current losses for applying coreless double-sided permanent magnet synchronous motor/generator to high-power flywheel energy storage system. *Journal of Applied Physics*, 105(7):07F116–07F116–3, Apr 2009.

[38] L. Bakay, M. Dubois, P. Viarouge, and J. Ruel. Losses in an optimized 8-pole radial amb for long term flywheel energy storage. In *Electrical Machines and Systems, 2009. ICEMS 2009. International Conference on*, pages 1 –6, nov. 2009.

[39] L. Bakay, M. Dubois, P. Viarouge, and J. Ruel. Losses in hybrid and active magnetic bearings applied to long term flywheel energy storage. In *Power Electronics, Machines and Drives (PEMD 2010), 5th IET International Conference on*, pages 1–6, April 2010.

[40] G. Cimuca, S. Breban, M.M. Radulescu, C. Saudemont, and B. Robyns. Design and control strategies of an induction-machine-based flywheel energy storage system associated to a variable-speed wind generator. *Energy Conversion, IEEE Transactions on*, 25(2):526–534, June 2010.

[41] Johan Abrahamsson. *Kinetic Energy Storage and Magnetic Bearings: for Vehicular Applications*. PhD thesis, Uppsala University, Uppsala, SE, 2014.

[42] M. Garcia-Gracia, M.A. Cova, M.T. Villen, and A. Uson. Novel modular and retractable permanent magnet motor/generator for flywheel applications with reduced iron losses in stand-by mode. *Renewable Power Generation, IET*, 8(5):551–557, July 2014.

[43] K. Asami, A. Chiba, M. Azizur Rahman, T. Hoshino, and A. Nakajima. Stiffness analysis of a magnetically suspended bearingless motor with permanent magnet passive positioning. *Magnetics, IEEE Transactions on*, 41(10):3820–3822, Oct 2005.

[44] M. Ooshima, S. Kitazawa, A. Chiba, T. Fukao, and D.G. Dorrell. Design and analyses of a coreless-stator-type bearingless motor/generator for clean energy generation and storage systems. *Magnetics, IEEE Transactions on*, 42(10):3461–3463, Oct 2006.

[45] M.N. Recheis, B. Schweighofer, P. Fulmek, and H. Wegleiter. Selection of magnetic materials for bearingless high-speed mobile flywheel energy storage systems. *Magnetics, IEEE Transactions on*, 50(4):1–4, April 2014.

[46] E. Severson, R. Nilssen, T. Undeland, and N. Mohan. Dual purpose no voltage winding design for bearingless motors. *Industrial Electronics, IEEE Transactions on*, PP(99):1–1, Under Review.

[47] E. Severson, R. Nilssen, T. Undeland, and N. Mohan. Dual purpose no voltage winding design for the bearingless ac homopolar and consequent pole motors. *Industry Applications, IEEE Transactions on*, PP(99):1–1, 2015.

[48] E. Severson, R. Nilssen, T. Undeland, and N. Mohan. Magnetic equivalent circuit modeling of the ac homopolar machine for flywheel energy storage. *Energy Conversion, IEEE Transactions on*, PP(99):1–1, 2015.

[49] Eric Severson, Srikant Gandikota, and Ned Mohan. Practical implementation of dual purpose no voltage drives for bearingless motors. In *Applied Power Electronics Conference and Exposition (APEC), 2015 IEEE*, pages 819–826, March 2015.

[50] E. Severson, R. Nilssen, T. Undeland, and N. Mohan. Suspension force model for bearingless ac homopolar machines designed for flywheel energy storage. In *GCC Conference and Exhibition (GCC), 2013 7th IEEE*, pages 274–279, Nov 2013.

[51] E Severson, R Nilssen, T Undeland, and N Mohan. Outer-rotor ac homopolar motors for flywheel energy storage. In *Power Electronics, Machines and Drives (PEMD 2014), 7th IET International Conference on*, pages 1–6, April 2014.

[52] E. Severson, R. Nilssen, T. Undeland, and N. Mohan. Analysis of the bearingless ac homopolar motor. In *International Conference on Electrical Machines (ICEM), 2012.*, pages 568 – 574, Sep. 2012.

[53] E. Severson, A. Rokke, R. Nilssen, T. Undeland, and N. Mohan. Design and measurement of a passive thrust magnetic bearing for a bearingless motor. In *Industrial Electronics Society, IECON 2013 - 39th Annual Conference of the IEEE*, pages 2720–2725, Nov 2013.

[54] E. Severson, R. Nilssen, T. Undeland, and N. Mohan. Experimental results and 3d finite element analysis of the ac homopolar motor. Presented at *MMM/IEEE Intermag*, 2013.

[55] E. Severson, R. Nilssen, T. Undeland, and N. Mohan. Dual purpose no voltage winding design for the bearingless ac homopolar and consequent pole motors. In *Power Electronics Conference (IPEC-Hiroshima 2014 - ECCE-ASIA), 2014 International*, pages 1412–1419, May 2014.

[56] A. Chiba, T. Fukao, O. Ichikawa, M. Oshima, M. Takemoto, and D.G. Dorrell. *Magnetic Bearings and Bearingless Drives.* Newnes, 2005.

[57] Wenshao Bu, Shenghua Huang, Shanming Wan, and Wensheng Liu. General analytical models of inductance matrices of four-pole bearingless motors with two-pole controlling windings. *Magnetics, IEEE Transactions on*, 45(9):3316 –3321, sept. 2009.

[58] J. Amemiya, A. Chiba, D.G. Dorrell, and T. Fukao. Basic characteristics of a consequent-pole-type bearingless motor. *Magnetics, IEEE Transactions on*, 41(1):82 – 89, jan. 2005.

[59] Swarn S. Kalsi. *Applications of High Temperature Superconductors to Electric Power Equipment.* Wiley-IEEE Press, 2011.

[60] O. Ichikawa, A. Chiba, and T. Fukao. Inherently decoupled magnetic suspension in homopolar-type bearingless motors. *Industry Applications, IEEE Transactions on*, 37(6):1668 –1674, nov/dec 2001.

[61] H. Hara, M. Takemoto, Y. Tanaka, A. Chiba, and T. Fukao. Reduction effect of suspension input power using rotor eccentricity in a bearingless motor. In *Electrical Machines and Systems, 2008. ICEMS 2008. International Conference on*, pages 2968 –2973, oct. 2008.

[62] J. Asama, R. Natsume, H. Fukuhara, T. Oiwa, and A. Chiba. Optimal suspension winding configuration in a homo-polar bearingless motor. *Magnetics, IEEE Transactions on*, 48(11):2973 –2976, Nov. 2012.

[63] H. Devred, M. Martinez, and J. Huonic. 150 kva, 56000 rpm, turbo engine integrated homopolar electrical generator. In *Electric Machines and Drives, 1999. International Conference IEMD '99*, pages 749–751, May 1999.

[64] K. Sivasubramaniam, E.T. Laskaris, M.R. Shah, J.W. Bray, and N.R. Garrigan. High-temperature superconducting homopolar inductor alternator for marine applications. *Applied Superconductivity, IEEE Transactions on*, 18(1):1–6, March 2008.

[65] K. Sivasubramaniam, T. Zhang, M. Lokhandwalla, E.T. Laskaris, J.W. Bray, B. Gerstler, M.R. Shah, and J.P. Alexander. Development of a high speed hts generator for airborne applications. *Applied Superconductivity, IEEE Transactions on*, 19(3):1656 –1661, June 2009.

[66] H.M. Cheshmehbeigi and E. Afjei. Design optimization of a homopolar salient-pole brushless dc machine: Analysis, simulation, and experimental tests. *Energy Conversion, IEEE Transactions on*, 28(2):289–297, June 2013.

[67] Zhang'ao Ren, Kexun Yu, Qingming Xin, and Yuan Pan. Performance of homopolar inductor alternator with diode-bridge rectifier and capacitive load. *Industrial Electronics, IEEE Transactions on*, 60(11):4891–4902, Nov 2013.

[68] Xin Qingming, Yu Kexun, You Qilin, and Yuan Man. Repetition pulse charging characteristics for homopolar inductor alternator with rectified capacitive load. *IEEJ Transactions on Electrical and Electronic Engineering*, 10(1):44–49, 2015.

[69] Christopher W Gabrys. Inductor alternator flywheel system, September 21 2004. US Patent 6,794,776.

[70] Paul C. Krause, Oleg Wasynczuk, and Scott D. Sudhoff. *Analysis of Electric Machinery and Drive Systems (2nd Edition)*. Wiley-IEEE Press, 2002.

[71] P. Tsao. *An Integrated Flywheel Energy Storage System with a Homopolar Inductor Motor/Generator and High-Frequency Drive*. PhD thesis, University of California, Berkley, Berkley, CA, 2003.

[72] Ned Mohan. *Advanced Electric Drives: Analysis, Control and Modeling Using Simulink*. Mnpere, 2001.

[73] X. Fu, M. Lin, H. Yu, L. Hao, D. Xu, P. Jin, and J. Zou. Calculation and analysis of iron loss in homopolar inductor alternator. *Magnetics, IEEE Transactions on*, 48(11):3466 –3469, nov. 2012.

[74] Zhang ao Ren, Kexun Yu, Zhenxiu Lou, and Caiyong Ye. Investigation of a novel pulse ccps utilizing inertial energy storage of homopolar inductor alternator. *Plasma Science, IEEE Transactions on*, 39(1):310 –315, jan. 2011.

[75] N. Levin, S. Orlova, V. Pugachov, and L. Ribickis. Optimization of the magnetic circuit of the homopolar inductor machine with non-overlapping concentrated windings. In *Power Electronics and Motion Control Conference (EPE/PEMC), 2010 14th International*, pages T4–77 –T4–81, sept. 2010.

[76] Juha Pyrhonen, Tapani Jokinen, and Valeria Hrabovcova. *Design of Rotating Electrical Machines*. Wiley, 2009.

[77] Hiperco 27 alloy data sheet.

[78] Arnon 5 data sheet.

[79] Zhenxiu Lou, Yigang He, Yuan Cheng, Caiyong Ye, and Kexun Yu. Analytical calculation of d- and q-axis synchronous reactances of homopolar inductor alternator. In *Electromagnetic Launch Technology (EML), 2014 17th International Symposium on*, pages 1–8, July 2014.

[80] S.I. Deaconu, M. Topor, L. Tutelea, G.N. Popa, and C. Abrudean. Mathematical model of a reactive homopolar synchronous machine with stator excitation. In *Power Electronics and Applications, 2009. EPE '09. 13th European Conference on*, pages 1–9, Sept 2009.

[81] C. Belalahy, I. Rasoanarivo, and F. M Sargos. Using 3d reluctance network for design a three phase synchronous homopolar machine. In *Industrial Electronics, 2008. IECON 2008. 34th Annual Conference of IEEE*, pages 2067–2072, Nov 2008.

[82] B. Nedjar, S. Hlioui, L. Vido, Y. Amara, and M. Gabsi. Hybrid excitation synchronous machine modeling using magnetic equivalent circuits. In *Electrical Machines and Systems (ICEMS), 2011 International Conference on*, pages 1–6, Aug 2011.

[83] H.W. Derbas, J.M. Williams, A.C. Koenig, and S.D. Pekarek. A comparison of nodal- and mesh-based magnetic equivalent circuit models. *Energy Conversion, IEEE Transactions on*, 24(2):388–396, June 2009.

[84] M.L. Bash, J.M. Williams, and S.D. Pekarek. Incorporating motion in mesh-based magnetic equivalent circuits. *Energy Conversion, IEEE Transactions on*, 25(2):329–338, June 2010.

[85] M.L. Bash and S.D. Pekarek. Modeling of salient-pole wound-rotor synchronous machines for population-based design. *Energy Conversion, IEEE Transactions on*, 26(2):381–392, June 2011.

[86] H. Gorginpour, H. Oraee, and R.A. McMahon. A novel modeling approach for design studies of brushless doubly fed induction generator based on magnetic equivalent circuit. *Energy Conversion, IEEE Transactions on*, 28(4):902–912, Dec 2013.

[87] Min-Fu Hsieh and You-Chiuan Hsu. A generalized magnetic circuit modeling approach for design of surface permanent-magnet machines. *Industrial Electronics, IEEE Transactions on*, 59(2):779–792, Feb 2012.

[88] A.R. Tariq, C.E. Nino-Baron, and E.G. Strangas. Iron and magnet losses and torque calculation of interior permanent magnet synchronous machines using magnetic equivalent circuit. *Magnetics, IEEE Transactions on*, 46(12):4073–4080, Dec 2010.

[89] T. Hosoi, K. Shima, and T. Fukami. Magnetic circuit analysis of permanent-magnet-assisted salient-pole synchronous machines under steady states. *Industry Applications, IEEE Transactions on*, 48(3):895–902, May 2012.

[90] M.L. Bash and S. Pekarek. Analysis and validation of a population-based design of a wound-rotor synchronous machine. *Energy Conversion, IEEE Transactions on*, 27(3):603–614, Sept 2012.

[91] G.M. Shane and S.D. Sudhoff. Refinements in anhysteretic characterization and permeability modeling. *Magnetics, IEEE Transactions on*, 46(11):3834–3843, Nov 2010.

[92] Vlado Ostovic. *Dynamics of Saturated Electric Machines.* Springer, 1989.

[93] Gerhard Schweitzer and Eric H Maslen. *Magnetic bearings: theory, design, and application to rotating machinery.* Springer, 2009.

[94] A. Chiba, T. Deido, T. Fukao, and M.A. Rahman. An analysis of bearingless ac motors. *Energy Conversion, IEEE Transactions on*, 9(1):61–68, Mar 1994.

[95] Xiaodong Sun, Long Chen, and Zebin Yang. Overview of bearingless permanent-magnet synchronous motors. *Industrial Electronics, IEEE Transactions on*, 60(12):5528–5538, Dec 2013.

[96] X Sun, C Chen, and Z Yang. Overview of bearingless induction motors. *Mathematical Problems in Engineering*, 2014, 2014.

[97] H. Wang, J. Bao, B. Xue, and J. Liu. Control of suspending force in novel permanent magnet biased bearingless switched reluctance motor. *Industrial Electronics, IEEE Transactions on*, PP(99):1–1, 2015.

[98] Tomohiro Takenaga, Yutaka Kubota, Akira Chiba, and Tadashi Fukao. A principle and winding design of consequent-pole bearingless motors. *JSME International Journal Series C*, 46(2):363–369, 2003.

[99] W. K S Khoo. Bridge configured winding for polyphase self-bearing machines. *Magnetics, IEEE Transactions on*, 41(4):1289–1295, 2005.

[100] Klaus Raggl, Thomas Nussbaumer, and Johann W Kolar. Comparison of separated and combined winding concepts for bearingless centrifugal pumps. *J. Power Electron*, 9(2):243–258, 2009.

[101] T. Reichert, T. Nussbaumer, and J.W. Kolar. Bearingless 300-w pmsm for bioreactor mixing. *Industrial Electronics, IEEE Transactions on*, 59(3):1376–1388, March 2012.

[102] W. Gruber, T. Nussbaumer, H. Grabner, and W. Amrhein. Wide air gap and large-scale bearingless segment motor with six stator elements. *Magnetics, IEEE Transactions on*, 46(6):2438–2441, June 2010.

[103] D. Steinert, T. Nussbaumer, and J.W. Kolar. Slotless bearingless disk drive for high-speed and high-purity applications. *Industrial Electronics, IEEE Transactions on*, 61(11):5974–5986, Nov 2014.

[104] P. Kascak, R. Jansen, T. Dever, A. Nagorny, and K. Loparo. Levitation performance of two opposed permanent magnet pole-pair separated conical bearingless motors. In *Energy Conversion Congress and Exposition (ECCE), IEEE*, pages 1649–1656, 2011.

[105] W. K S Khoo, K. Kalita, and S.D. Garvey. Practical implementation of the bridge configured winding for producing controllable transverse forces in electrical machines. *Magnetics, IEEE Transactions on*, 47(6):1712–1718, 2011.

[106] Jin Huang, Bingnan Li, Haibo Jiang, and Min Kang. Analysis and control of multiphase permanent-magnet bearingless motor with a single set of half-coiled winding. *Industrial Electronics, IEEE Transactions on*, 61(7):3137–3145, July 2014.

[107] E.F. Rodriguez and J.A. Santisteban. An improved control system for a split winding bearingless induction motor. *Industrial Electronics, IEEE Transactions on*, 58(8):3401–3408, Aug 2011.

[108] R. L A Ribeiro, F. E F Castro, A.O. Salazar, and A.L. Maitelli. A suitable current control strategy for split-phase bearingless three-phase induction machine. In *Power Electronics Specialists Conference, 2005. PESC '05. IEEE 36th*, pages 701–706, June 2005.

[109] SWK Khoo, RL Fittro, and SD Garvey. An ac self-bearing rotating machine with a single set of windings. In *Power Electronics, Machines and Drives. International Conference on*, pages 292–297. IET, 2002.

[110] A. Chiba, K. Sotome, Y. Iiyama, and M. Azizur Rahman. A novel middle-point-current-injection-type bearingless pm synchronous motor for vibration suppression. *Industry Applications, IEEE Transactions on*, 47(4):1700–1706, 2011.

[111] R. Oishi, S. Horima, H. Sugimoto, and A. Chiba. A novel parallel motor winding structure for bearingless motors. *Magnetics, IEEE Transactions on*, 49(5):2287–2290, 2013.

[112] A Chiba, S. Horima, and H. Sugimoto. A principle and test results of a novel bearingless motor with motor parallel winding structure. In *Energy Conversion Congress and Exposition (ECCE), 2013 IEEE*, pages 2474–2479, Sept 2013.

[113] D. Grahame Holmes and Thomas A. Lipo. *Pulse Width Modulation for Power Converters: Principles and Practice*. Wiley-IEEE Press, 2003.

[114] Yashan Hu, Zi-Qiang Zhu, and Kan Liu. Current control for dual three-phase permanent magnet synchronous motors accounting for current unbalance and harmonics. *Emerging and Selected Topics in Power Electronics, IEEE Journal of*, 2(2):272–284, June 2014.

[115] Xiaoming Yuan, W. Merk, H. Stemmler, and J. Allmeling. Stationary-frame generalized integrators for current control of active power filters with zero steady-state error for current harmonics of concern under unbalanced and distorted operating conditions. *Industry Applications, IEEE Transactions on*, 38(2):523–532, Mar 2002.

[116] Jing Wang, D.D. Konikkara, and A. Monti. A generalized approach for harmonics and unbalanced current compensation through inverter interfaced distributed generator. In *Power Electronics for Distributed Generation Systems (PEDG), 2014 IEEE 5th International Symposium on*, pages 1–8, June 2014.

[117] Ping Hsu and M. Behnke. A three-phase synchronous frame controller for unbalanced load [invertor operation]. In *Power Electronics Specialists Conference,*

1998. PESC 98 Record. 29th Annual IEEE, volume 2, pages 1369–1374 vol.2, May 1998.

[118] L. Ravi, E.L. Severson, S. Tewari, and N. Mohan. Circuit-level characterization and loss modeling of sic-based power electronic converters. In *Industrial Electronics Society, IECON 2014 - 40th Annual Conference of the IEEE*, pages 1291–1297, Oct 2014.

[119] P. Karutz, T. Nussbaumer, W. Gruber, and J.W. Kolar. Novel magnetically levitated two-level motor. *Mechatronics, IEEE/ASME Transactions on*, 13(6):658 –668, dec. 2008.

[120] W. Gruber, H. Grabner, S. Silber, and W. Amrhein. Design of a brushless permanent magnet synchronous drive with a merely passively suspended rotor. In *Power Electronics, Electrical Drives, Automation and Motion (SPEEDAM), International Symposium on*, pages 597–602, 2012.

[121] H. Grabner, W. Amrhein, S. Silber, and W. Gruber. Nonlinear feedback control of a bearingless brushless dc motor. *Mechatronics, IEEE/ASME Transactions on*, 15(1):40–47, Feb.

[122] J. Asama, T. Asami, T. Imakawa, A. Chiba, A. Nakajima, and M.A. Rahman. Effects of permanent-magnet passive magnetic bearing on a two-axis actively regulated low-speed bearingless motor. *Energy Conversion, IEEE Transactions on*, 26(1):46 –54, march 2011.

[123] Fengxiang Wang and Longya Xu. Calculation and measurement of radial and axial forces for a bearingless pmdc motor. In *Industry Applications Conference, 2000. Conference Record of the 2000 IEEE*, volume 1, pages 249–252 vol.1.

[124] B. Warberger, R. Kaelin, T. Nussbaumer, and J.W. Kolar. 50- /2500-w bearingless motor for high-purity pharmaceutical mixing. *Industrial Electronics, IEEE Transactions on*, 59(5):2236–2247, 2012.

[125] M. Siebert, B. Ebihara, R. Jansen, R.L. Fusaro, A. Kascak, and A. Kenny. A passive magnetic bearing flywheel. In *Proceedings of the Intersociety Energy Conversion Engineering Conference*, pages 125–132, Feb. 2002.

[126] T. Ohji, S.C. Mukhopadhyay, M. Iwahara, and S. Yamada. Permanent magnet bearings for horizontal- and vertical-shaft machines: A comparative study. *Journal of Applied Physics*, 85(8):4648–4650, Apr 1999.

[127] R. De Andrade Jr., G.G. Sotelo, A.C. Ferreira, L.G.B. Rolim, J.L. Da Silva Neto, R.M. Stephan, W.I. Suemitsu, and R. Nicolsky. Flywheel energy storage system description and tests. *IEEE Transactions on Applied Superconductivity*, 17(2):2154–2157, 2007.

[128] G.G. Sotelo, R. De Andrade Jr., and A.C. Ferreira. Magnetic bearing sets for a flywheel system. *IEEE Transactions on Applied Superconductivity*, 17(2):2150–2153, 2007.

[129] R.M. Stephan, R. De Andrade Jr., G.C. Dos Santos, M.A. Neves, and R. Nicolsky. Levitation force and stability of superconducting linear bearings using ndfeb and ferrite magnets. *Physica C: Superconductivity and its Applications*, 386:490–494, 2003.

[130] M. Autila, E. Lantto, and A. Arkkio. Determination of forces and linearized parameters of radial active magnetic bearings by finite element technique. *Magnetics, IEEE Transactions on*, 34(3):684–694, May 1998.

[131] Samuel Earnshaw. On the nature of the molecular forces which regulate the constitution of the luminiferous ether. *Trans. Camb. Phil. Soc*, 7:97–112, 1842.

[132] J. Delamare, E. Rulliere, and J.P. Yonnet. Classification and synthesis of permanent magnet bearing configurations. *IEEE Transactions on Magnetics*, 31(6 pt 2):4190–4192, 1995.